Performance Evaluation and Durability Studies of Adhesive Bonds

Shantanu Rajendra Ranade

Dissertation submitted to the faculty of the Virginia Polytechnic Institute and State University in partial fulfillment of the requirements for the degree of

Doctor of Philosophy
In
Macromolecular Science and Engineering

David A. Dillard, Chair
Romesh C. Batra
Robert B. Moore
John G. Dillard
Ann M. Norris

26 August, 2014
Blacksburg, VA

Keywords: Structural Adhesives, Double Cantilever Beam Test, Surface Defects, Pressure Sensitive Adhesives, Silicone Sealants

Performance Evaluation and Durability Studies of Adhesive Bonds

Shantanu Rajendra Ranade

ABSTRACT

In this thesis, four test approaches were developed to characterize the adhesion performance and durability of adhesive bonds for specific applications in areas spanning from structural adhesive joints to popular confectionaries such as chewing gum. In the first chapter, a double cantilever beam (DCB) specimen geometry is proposed for combinatorial fracture studies of structural adhesive bonds. This specimen geometry enabled the characterization of fracture energy vs. bondline thickness trends through fewer tests than those required during a conventional "one at a time" characterization approach, potentially offering a significant reduction in characterization times. The second chapter investigates the adhesive fracture resistance and crack path selection in adhesive joints containing patterns of discreet localized weak interfaces created using physical vapor deposition of copper. In a DCB specimen tested under mode-I conditions, fracture energy within the patterned regions scaled according to a simple rule of mixture, while reverse R-curve and R-curve type trends were observed in the regions surrounding weak interface patterns. Under mixed mode conditions such that bonding surface with patterns is subjected to axial tension, fracture energy did not show R-curve type trends while it was observed that a crack could be made to avoid exceptionally weak interfaces when loaded such that bonding surface with defects is subjected to axial compression. In the third chapter, an adaptation of the probe tack test is proposed to characterize the adhesion behavior of gum cuds. This test method allowed the introduction of substrates with well-defined surface energies and topologies to study their effects on gum cud adhesion. This approach and reported insights could potentially be useful in developing chewing gum formulations that facilitate easy removal of improperly discarded gum cuds from adhering surfaces. In the fourth chapter we highlight a procedure to obtain insights into the long-term performance of silicone sealants designed for load-bearing applications such as solar panel support sealants. Using small strain constitutive tests and time-temperature-superposition principle, thermal shift factors were obtained and successfully used to characterize the creep rupture master curves for specific joint configurations, leading to insights into delayed failures corresponding to three years through experiments carried out in one month.

Acknowledgements

I wish to thank my advisor, Dr. David A. Dillard for giving me an opportunity to work in the area of adhesives and adhesive science. He has given me invaluable opportunities to be involved in different research projects, attend several technical conferences and interact with many expert scientists in the adhesion science area. These experiences and his efforts to develop my scientific competence have been deeply appreciated.

I also wish to acknowledge my Ph.D. committee members Dr. Romesh Batra, Dr. Ann Norris, Dr. Robert Moore and Dr. John Dillard for valuable suggestions and guidance during my research. I am also thankful to Dr. Alan Esker, Dr. Bruce Orler, Dr. Donatus Ohanehi for helpful interactions during my research projects.

I would like to thank the National Science Foundation (NSF/CMMI Award No. 0826143) for funding part of this research as well as the LORD^{TM} Corporation (Cary, NC) for supplying adhesives needed during this work

I am also thankful to my department, Macromolecules and Interfaces Institute for providing opportunities to attend numerous conferences and inviting many reputed scientists for seminars talks. I want to thank Engineering Science & Mechanics Department and the Institute of Critical Technology and Applied Science for providing facilities and fostering a great environment for studying and doing research.

Special thanks go to Tammy-Jo Hiner and Melissa Nipper for all their help during administrative and graduate school procedures.

I want to thank Mac McCord, Danny Reed, for their inputs and help during setting new experiments and Darrell L. Link whose machining tools from shop were always handy.

I would like to express my gratitude and admiration to my parents, Rajendra Ranade, Aparna Ranade and my sister Sukhada Ranade, who have always encouraged me to do the best possible work and their support and love throughout this journey has been inspiring.

I would like to express my gratitude to Chainika Jangu, a special person whose

unconditional love, patience and deep support gave me strength and motivation during my stay at Virginia Tech.

I would like to thank the people that made my time at the Adhesion Mechanics Lab enjoyable and fulfilling: Youliang Guan, Qian Li, Bikramjit Mukharjee, Geoffrey Tizard, Jessica May, Katherine Finlay and past graduates from our lab, Edoardo Nicoli and Kshitish Patankar, and other colleagues and undergrads. Their friendship and cooperation have been truly genuine.

Table of Contents

List of Figures

List of Tables

1 Introduction

Adhesive bonding is a widely used method for joining two or more similar and dissimilar materials during diverse range of applications. Some common application areas include industries such as automotive, aerospace, renewable energy, construction and civil infrastructure industry to name a few [1]. Joining of materials using adhesives can lead to more uniform stress distributions within joints than joints prepared using methods such as riveting or bolting, where the structure is weakened considerably due to the high stress concentration around holes [2]. Though joining of metals using metal welding can offer similar advantages, adhesive bonding can be advantageous due to their ability to bond thinner materials and their relatively low weight density. Adhesives can be used to bond dissimilar surfaces such as wood, plastic, metal, ceramics, composites etc. where in most cases the welding techniques are not applicable [3]. This results in an increase in the number of materials that can be used leading to more efficient and novel designs. Similar to joining methods such as welding and riveting, bonding operations using adhesives can be automated, as they can be readily adapted to robotic assembly techniques, which can result in high production throughput. However, there are some shortcomings for the adhesive bonding technology such as the need of surface pretreatments in some applications, limited temperature ranges over which they can be employed, and the relatively low strength in tension compared to metals [2, 4].

For enabling the use of adhesives and for designing adhesive joints in structural or semi-structural applications, it is critical to understand the performance of adhesives in the relevant joint geometries. Numerous standards are available for characterizing bulk adhesive properties and adhesive joint performance in standardized test configurations [2, 5]. In spite of results from these methods being valuable in terms of characterizing adhesive performance and discriminating among adhesive choices, the performance of adhesive joints in real structures remains difficult to predict [2, 6, 7]. These difficulties arise as the failure of an adhesive joint in real structures can be a complex and nonlinear phenomenon that depends upon application specific parameters such as adherend preparation and bond formation, loading conditions, joint geometry, environmental exposure conditions, and other factors. [4, 6, 8] In many cases standardized test methods

may fail to adequately represent the complexities of actual joints in service. At the same time it is often difficult to mimic infield joint conditions during laboratory testing and full-scale tests using real structures may not be feasible. Thus in many cases, characterizing adhesive performance for specific applications requires careful consideration of possible relevant stress states, environmental aspects and loading conditions and other factors in the envisioned adhesive joint application. Based on these considerations, a test approach can be developed which may involve testing of one or more adhesive joint configurations that induce the relevant stress states which are likely to be encountered in envisioned adhesive joint configuration. Similar approach can be useful in designing test methods to understand the mechanisms of failures, locus of failure and to obtain basic insights regarding adhesive performance as a function of variables that are of interest [9-13].

In this thesis four test approaches were developed to characterize the adhesion performance and durability of a variety of adhesive bonds. These were developed for specific applications in areas spanning from structural adhesive joints to popular confectionaries such as chewing gums. The thesis is organized as follows:

Chapter 1:

In this chapter, double cantilever beam specimens with linearly increasing or decreasing bondline thickness were studied for their feasibility to determine the fracture energy of adhesively bonded joints as a function of bondline thickness. In a combinatorial characterization sense, this approach explores the possibility to characterize the effect of bondline thickness on fracture energy through fewer tests than those required for a "one at a time" characterization approach, thus potentially offering a significant reduction in characterization times. This study has been accepted and will be published in *International Journal of Adhesion and Adhesives*.

Chapter 2:

In this chapter a test approach was developed to characterize and investigate the adhesive fracture resistance and crack path selection in adhesive joints containing localized

defects. The defects in adhesive joints can be in the form of voids, improperly mixed or cured adhesive in some locations, adherend surface contaminations, etc. The presence of such defects can lead to weakened interfaces with reduced stiffness or load carrying capabilities or disbonds that are incapable of resisting certain tractions at the interface of an adhesive joint. Apart from the insights about robustness of the adhesive joints, a better understanding of fracture resistance and crack path selection in the presence of localized interfacial defects might lead to adhesive joints with tunable failure locus and resistance to fracture. Such joints might be useful in applications that require controlled disassembly of adhesive joints, such as the packaging industry, and perhaps other fields where recycling and reuse options offer enhanced sustainability. This study is to be submitted as a publication in *Journal of Adhesion*.

Chapter 3:

In this chapter a characterization procedure was developed to assess adhesion fundamentals for chewing gum cuds. The chewed gum cud is a soft viscoelastic material, which similar to a pressure sensitive adhesive sticks to many surfaces upon brief contact. Thus, although very popular, improperly disposed chewed gum cud can be a nuisance product, adhering tenaciously to surfaces on which they have been deposited. Cleanup can be expensive and require extensive efforts. In this study a probe test based approach was developed to obtain insights into the effect of surface energy and surface roughness on gum cud adhesion. It is envisioned that this approach could be helpful towards quantifying gum cud adhesion leading to chewing gum formulations, which when chewed and improperly discarded, facilitate easy removal during the cleanup process. This study is due to be submitted as a publication in *Journal of Adhesion*.

Chapter 4:

In this chapter we aim to highlight a procedure to obtain insights into and compare the long-term creep rupture performance of three different silicone sealants designed for load-bearing applications for solar panel support sealants, though the techniques and materials may also be relevant in other engineering and building structures. Unlike sealant formulations, which have been sold for many years, new sealant formulations for

emerging load bearing applications do not have a well-established performance history. Generating accurate and a reliable long-term performance history for a new sealant and application typically requires extensive outdoors and in service testing. In light of ever shortening product development cycles, accelerated laboratory testing can offer valuable insights into the long-term performance of the newly developed product [14]. In this chapter the long-term performance of silicone sealants was studied through creep rupture tests carried out at three different load levels and at three different humidity and temperature combinations. Accelerated testing, coupled with the application of time-temperature-superposition principle to failure data allowed estimation of delayed failures corresponding to three years through experiments carried out in one month, which might prove impractical to achieve using stress as the only accelerating factor. This study is due to be submitted in *Journal of Testing and Evaluation* by ASTM.

References

[1] E. M. Petrie, *Handbook of Adhesives and Sealants*: McGraw-Hill New York, 2000.

[2] A. J. Kinloch, *Adhesion and Adhesives: Science and Technology*. London; New York: Chapman and Hall, 1987.

[3] B. Müller and R. Walter, *Formulating Adhesives and Sealants: Chemistry, Physics and Applications*. Hannover: Vincentz Network, 2010.

[4] E. H. Andrews and A. J. Kinloch, "Mechanics of Adhesive Failure II," *Proceedings of the Royal Society of London. A. Mathematical and Physical Sciences,* **332**, 401-414, 1973.

[5] A. V. Pocius, D. A. Dillard, and M. K. Chaudhury, *Adhesion Science and Engineering* vol. 2. Amsterdam; Boston: Elsevier, 2002.

[6] A. V. Pocius, D. A. Dillard, and M. K. Chaudhury, *Adhesion Science and Engineering* vol. 1. Amsterdam; Boston: Elsevier, 2002.

[7] P. Martiny, F. Lani, A. J. Kinloch, and T. Pardoen, "A Multiscale Parametric Study of Mode I Fracture in Metal-to-Metal Low-Toughness Adhesive Joints," *International Journal of Fracture,* **173**, 105-133, 2012.

[8] V. Cooper, A. Ivankovic, A. Karac, D. McAuliffe, and N. Murphy, "Effects of Bond Gap Thickness on the Fracture of Nano-Toughened Epoxy Adhesive Joints," *Polymer,* **53**, 5540-5553, 2012.

[9] B. Chen and D. A. Dillard, "The Effect of the T-Stress on Crack Path Selection in Adhesively Bonded Joints," *International Journal of Adhesion and Adhesives,* **21**, 357-368, 2001.

[10] B. Chen, D. A. Dillard, J. G. Dillard, and R. L. Clark Jr, "Crack Path Selection in Adhesively Bonded Joints: The Roles of External Loads and Specimen Geometry," *International Journal of Fracture,* **114**, 167-190, 2002.

[11] B. Chen, D. A. Dillard, J. G. Dillard, and R. L. Clark, "Crack Path Selection in Adhesively-Bonded Joints: The Role of Material Properties," *The Journal of Adhesion,* **75**, 405-434, 2001.
[12] E. F. Karachalios, R. D. Adams, and L. F. M. da Silva, "Strength of Single Lap Joints with Artificial Defects," *International Journal of Adhesion and Adhesives,* **45**, 69-76, 2013.
[13] J. Y. Chung and M. K. Chaudhury, "Roles of Discontinuities in Bio-Inspired Adhesive Pads," *Journal of The Royal Society Interface,* **2**, 55-61, 2005.
[14] A. T. Wolf, *Durability of Building Sealants: State-of-the-art Report of RILEM Technical Committee 139-DBS, Durability of Building Sealants* vol. 21: RILEM publications, 1999.

2 A Tapered bondline thickness double cantilever beam (DCB) specimen geometry for combinatorial fracture studies of adhesive bonds

S. R. Ranade, Y. Guan, D. C. Ohanehi, J. G. Dillard, R. C. Batra, and D. A. Dillard, "A tapered bondline thickness double cantilever beam (DCB) specimen geometry for combinatorial fracture studies of adhesive bonds," *International Journal of Adhesion and Adhesives*, **55**, 155-160, 2014.

2.1 Introduction

The effect of bondline thickness (t), on adhesive joint performance has been the subject of considerable research, with many studies showing quite significant differences in resistance to failure as a function of the adhesive bondline thickness [1-13]. It has been observed, as shown schematically in Figure 2-1 for toughened epoxy adhesive systems, that the fracture energy of an adhesive joint shows complex dependence upon the bondline thickness, with fracture energy values passing through a maximum at a certain bondline thickness t_m [1-3, 10].

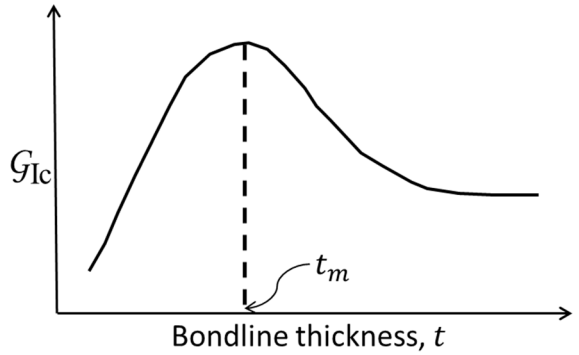

Figure 2-1: Schematic representation of the effect of bondline thickness on mode I fracture energy of a toughened epoxy adhesive DCB specimen

It has been suggested that such behavior for a toughened adhesive system, is due

to varying amounts of plastic deformations that develop ahead of the crack tip. In the fracture of monolithic materials, the size of the plastic zone (r_p) developing at the crack tip often affects the resulting fracture energy. For small adhesive bondline thickness, $t < t_m$, the development of the plastic zone at the crack tip is restricted due to the presence of stiff, high yield strength adherends. Thus the adhesive fracture energy decreases with a decrease in the bondline thickness for $t < t_m$. As shown in Figure 2-2 (a), at $t = t_m$, the plastic zone ahead of the crack tip is fully developed with the diameter of the plastic zone ($2r_p$) normal to the plane of the crack being nearly equal to the bondline thickness, which results in a maximum fracture energy value for a DCB specimen bonded with a given adhesive.

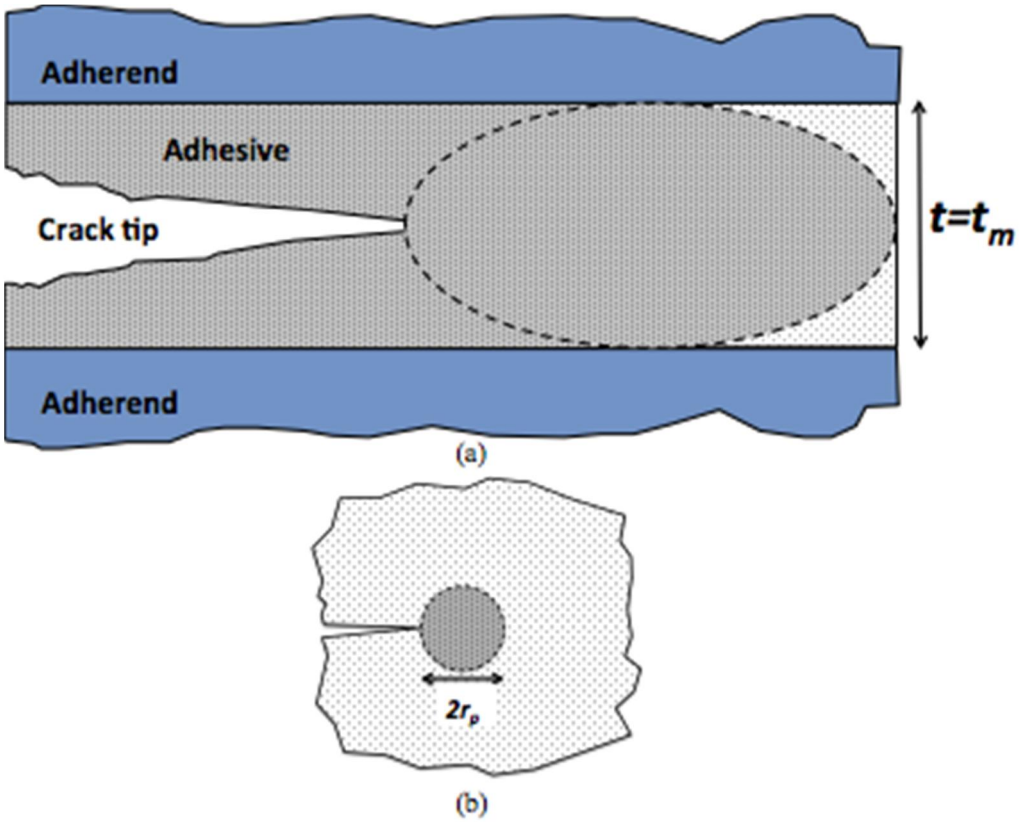

Figure 2-2: Schematic sketch of the plastic zone developed at a crack tip in (a) an adhesive joint at bondline thickness $t = t_m$ [14], and (b) in a monolithic elastic-plastic material

It has been reported that due to constraints imposed by stiff adherends, local tensile stresses ahead of the crack tip act over longer distances, thus leading to plastic zone size being longer in length in joints than those in bulk adhesive specimens [3, 15, 16]. In Figure 2-1 at bondline thicknesses $t > t_m$, the constraint due to the presence of

stiff adherends decreases, thus decreasing the length of the plastic zone and resulting in lower fracture energy values compared to the fracture energy at $t = t_m$. Similar observations have been reported based on studies using finite element methods [7, 8]. Cooper et al. conducted finite element analysis of TDCB joints with several bondline thicknesses, using a Dugdale-type cohesive zone model (CZM) to simulate mode I fracture in an adhesive joint [9]. Martiny et al. used a model based on a critical maximum principal stress at a critical distance ahead of a crack tip as a failure criterion, to study the variation of the fracture energy with the bondline thickness [10, 17]. It has been observed for toughened epoxy adhesive systems that the fracture energy vs bondline thickness trends and the maximum in the fracture energy value also depends upon test variables such as the loading rate and the test temperature. It was also observed that at a given loading rate, test temperature changes in joint width altered trends for the fracture energy as a function of the bondline thickness [1].

In light of such a complex dependence of the fracture energy on the bondline thickness and to maintain high quality of joints, the aircraft industry has long used techniques that tightly control the bondline thickness for critical structural joints. The use of supporting scrim cloth layers, for example, resists the flow of viscous adhesives and can result in good bondline thickness control[18]. However, in some applications, tolerances over bondline thickness are less strict, such as in the mass-produced automotive industry. The very large size and complex shapes involved in wind turbine blade assembly lead to an even wider range of bondline thicknesses, which may be many millimeters thick, much thicker than what has typically been used or recommended for structural joints. For these and other similar applications, an understanding of the adhesive joint performance as a function of the bondline thickness is critical. This typically requires characterizing the fracture energy using multiple DCB specimens with each specimen having a constant bondline thickness. This “one at a time” characterization approach requires many specimens and significant preparation, testing, and analysis effort.

In a combinatorial characterization sense, the approach outlined in this study aims to explore the possibility of characterizing the effect of the bondline thickness on the

fracture energy through fewer tests and in less time than those required for "one at a time" bondline thickness characterization approach. In this study the feasibility of using double cantilever beam (DCB) specimens with either increasing or decreasing bondline thickness (Figure 2.3) has been assessed to determine the fracture energy as a function of the bondline thickness. An estimate of the plastic zone size in mode I plane strain conditions for bulk adhesive specimens was obtained through single edge notch bend (SENB) tests and the plastic zone size was then compared to t_m measured (Figure 2-1) in DCB tests.

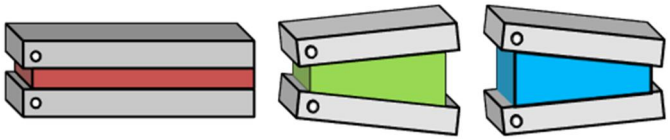

(a) (b) (c)

Figure 2-3: Exaggerated schematic diagrams of DCB specimens with adhesive bondline thickness (a) constant, (b) increasing, and (c) decreasing.

2.2 Experimental Work

2.2.1 DCB tests

DCB test specimens were prepared using 6061-T6511 aluminum adherends, having dimensions of 305 mm x 25.4 mm x 12.7 mm (length x width x thickness). Circular holes were drilled at one end of each aluminum bar to accommodate 6.4 mm diameter loading pins. The adherends were then abraded with #220 sandpaper and exposed to a base-acid surface treatment, which consisted of placing aluminum bars in 10% (wt./wt.) NaOH solution for 10 minutes, rinsing with deionized (DI) water and placing them in $HNO_3 : H_2O = 1:1$ (vol./vol.) for 2 to 3 minutes or until the surfaces regained a white metallic appearance. The adherends were then rinsed again with DI water, and placed in an oven heated to 110°C for about 2 hours to remove moisture absorbed on the surface. Two types of specimens were prepared. The first type of specimens had several constant adhesive bondline thicknesses (six specimens with bondline thicknesses of 0.02 mm, 0.77 mm, 1.7 mm, 1.87 mm, 2.26 mm, and 4.52 mm); the second type of specimens consisted of 12 either linearly increasing or linearly decreasing bondline thickness depending upon which end was drilled for the loading pins and the direction in which the subsequent debond propagated. Exaggerated schematic

sketches of the three types of specimens are shown in Figure 2.3. Commercially available LORD^{TM} 320/322 structural epoxy adhesive was used to bond the aluminum adherends. Before bonding the adherends, each pair of adherends was marked on the outer (non-bonding) surface at five locations spaced at approximately equal intervals using a permanent marker and the thickness of the adherends was measured at these locations. The adhesive was then applied on one of the adherends and the adherends were clamped together at both ends while maintaining the alignment of the adherends. The desired bondline thicknesses were achieved by placing spacers of appropriate thickness at each end of the specimen. Due to the highly viscous nature of the adhesive, no confinement was necessary to prevent the adhesive from flowing out of the bondline. Specimens were then cured for 14 hours at room temperature, followed by a post-cure at 60°C for 3 hours. All adhesive joint and bulk adhesive specimens used in this study were cured at same conditions. Based on dynamic mechanical analysis measurements (temperature sweep, 1 Hz), experiments, the glass transition temperature of the bulk adhesive was 85°C for the mentioned curing conditions. After bonding, the total thicknesses of the bonded specimens were measured at the marked locations on the adherends and the bondline thickness at marked locations was calculated by subtracting adherend thicknesses from the total thickness of the specimens. For linearly increasing or linearly decreasing bondline thickness specimens, the distances between marked locations and drilled holes were measured, and the bondline thickness values at the first and the last marked location from the drilled holes were plotted as a function of the distance from the loading holes. A straight line was fitted through the points, and an expression for the bondline thickness as a function of the distance from the drilled holes was obtained. This expression was used to determine the bondline thickness at each crack length. Prior to conducting the tests, typewriter correction fluid was applied on the bondline to facilitate observations of the crack tip. Paper rulers were affixed to the specimens to help measure crack growth. The DCB tests were carried out at room temperature (about 25°C) in an Instron model 5800R in mode I conditions at a total crosshead rate of 0.1 mm/min. The mode I fracture energies were calculated using the corrected beam theory (CBT) (Equation 1.1) [19, 20].

$$G_{Ic} = \frac{3P\delta}{2B(a+\hat{a})}F \tag{1.1}$$

where,

G_{Ic} is mode I fracture energy

a is crack length

P is load measured by load cell at crack length, a

δ is crosshead displacement at a crack length, a

F is large displacement correction

B is width of the specimen

$\hat{a}$ is the crack length correction for a beam that is not perfectly built in

2.2.2 Three point bend tests

The single edge notch beam (SENB) tests were used to calculate the plane strain fracture toughness (K_{Ic}) of the bulk adhesive specimens, following the ASTM D 5045-99 standard. Bulk adhesive specimens were cast using silicone molds. The SENB specimens had dimensions of about 57.1 mm x 12.7 mm x 6.3 mm (length x width x thickness). Specimens were pre-cracked by driving a fresh, sharp razor blade by gentle tapping such that the crack tip was a few millimeters ahead of the razor blade tip. Due to the lack of distinguishing features on the fractured surfaces of the SENB specimens, it was not possible to unambiguously measure the length of the pre-crack from fractured specimens. Crack lengths were measured using high-resolution images of the pre-cracked specimens and digital image analysis software. Pre-cracked specimens were then mounted crack down on a 3-point bend fixture in an Instron model 5500R and loaded at a constant crosshead rate of 0.1 mm/min. All three point bend tests were carried out at room temperature (about 25°C). The distance between the supporting rollers in the 3-point bend fixture was 4 times the width of the specimens. Plane strain fracture toughness values were calculated as per ASTM D 5045-99 standard, utilizing tensile yield strength ($\sigma_{y\ tensile}$) values estimated from compression tests, as described in the next section [1]. The plane stress plastic zone size, r_p, was estimated using the following expression (Equation 1.2) [21].

$$r_p = \frac{1}{2\pi}\left(\frac{K_{Ic}}{\sigma_{ytensile}}\right)^2 \quad (1.2)$$

2.2.3 Compression tests

Dogbone specimens were cast using silicone molds. When tested in tension to obtain tensile yield strength, specimens failed in a brittle manner, precluding the use of tensile tests for obtaining the tensile yield strength values. Similar behavior has been reported for a toughened epoxy adhesive system when tested in tension[1]. For a toughened epoxy system, it has been reported that the tensile yield strength equals nearly 0.75 times the compressive yield strength [1]. For compression tests, three cylindrical specimens were cast and cured at conditions same as those of the DCB and the SENB tests. Specimens were then machined to a height/diameter ratio between 2 to 1.5. The three specimens had a diameter in the range of 10.16 mm to 15.24 mm. The specimens were loaded between non-lubricated polished steel plates in an Instron 5800R test frame at 0.1mm/min. The load values were converted into the nominal axial stress by dividing the load by the original cross-sectional area of the specimen. The change in the specimen length was obtained through crosshead movement and converted to the average axial strain by dividing it by the original specimen length. Compressive yield strength ($\sigma_{y\ compresion}$) was calculated from the stress-strain curves by using 1% strain offset. Compressive modulus values were obtained from the slope of the linear part of the stress-strain curve. Compressive stress vs. compressive strain curves corrected for a toe region (artifact caused by take up of slack, alignment or seating of the specimen) are shown in Figure 2-4. Guidelines from ASTM D 695 – 02a standard were used to compensate for the toe region in the compressive stress vs. compressive strain curves.

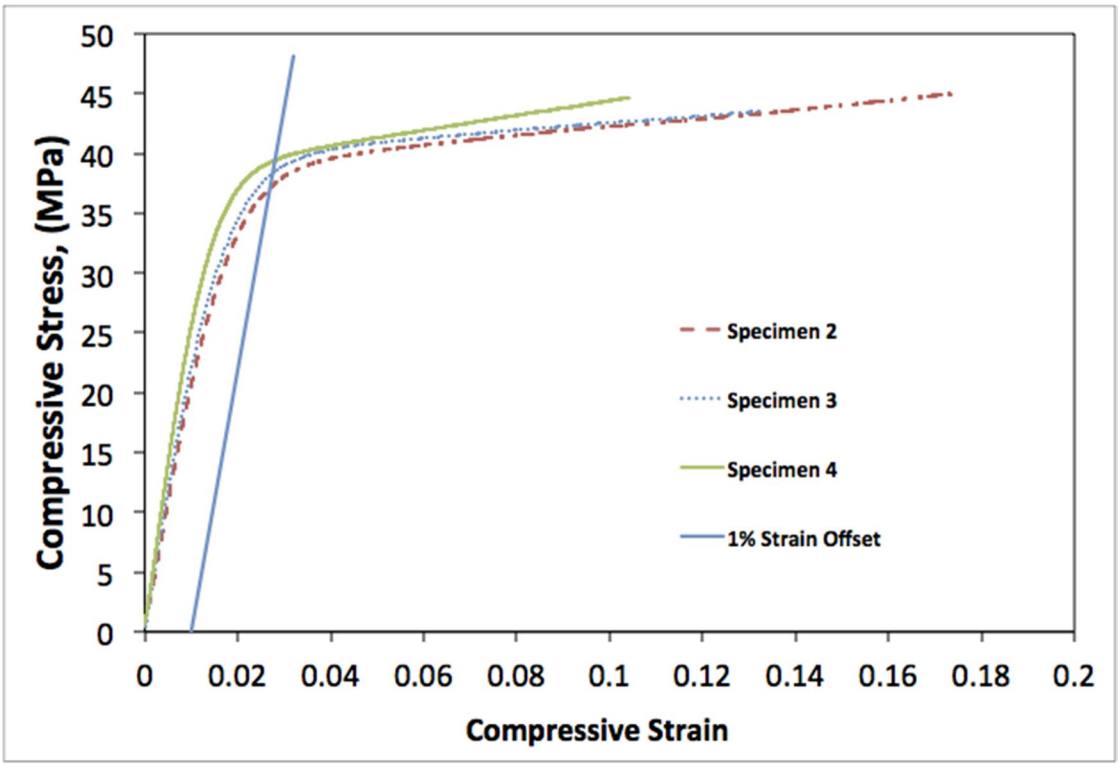

Figure 2-4: Engineering compressive axial stress vs. compressive axial strain curves from compression tests

2.3 Results and Discussion

The fracture energy vs. the crack length data for DCB specimens having a constant bondline thickness is shown in Figure 2-5. It was found that as the crack propagated along the length of a specimen, the fracture energy remained essentially constant (within ± 10 % of the average value). Similar trends were observed when fracture energies were calculated using the experimental compliance method. Fracture energy values (based on CBT) from a specimen were then averaged and plotted as a function of the bondline thickness. These plots are shown in Figure 2-6. A horizontal error bar for a given data point, where visible in Figure 2-6, indicates the maximum and the minimum adhesive bondline thickness values measured during thickness measurements at several locations for a given DCB specimen. A vertical error bar for a given data point shows the ± one standard deviation of the fracture energy values for a given specimen. From results depicted in Figure 2-6, it can be observed that for the adhesive system used in this study, fracture energies tend to increase with an increase in the bondline thickness up to about 2 mm and then essentially remain constant out to the

bondline thickness of about 4 mm.

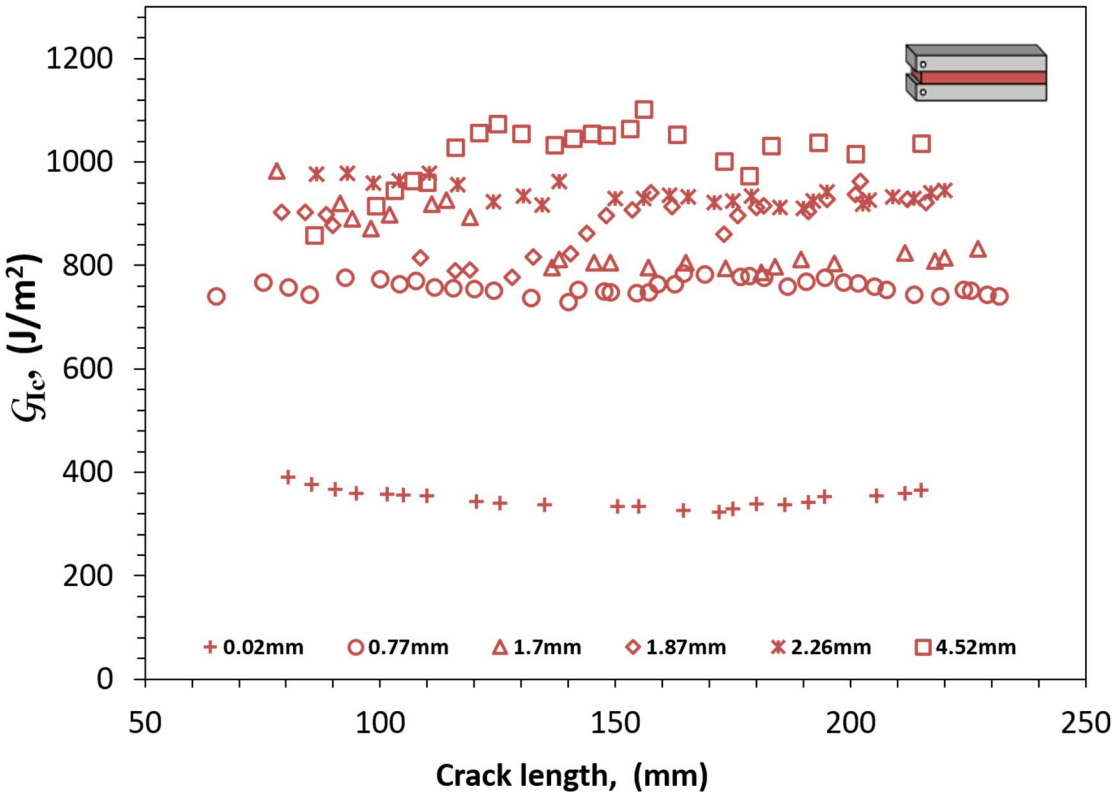

Figure 2-5: Variation of mode I fracture energy with crack length for DCB specimens with constant bondline thickness.

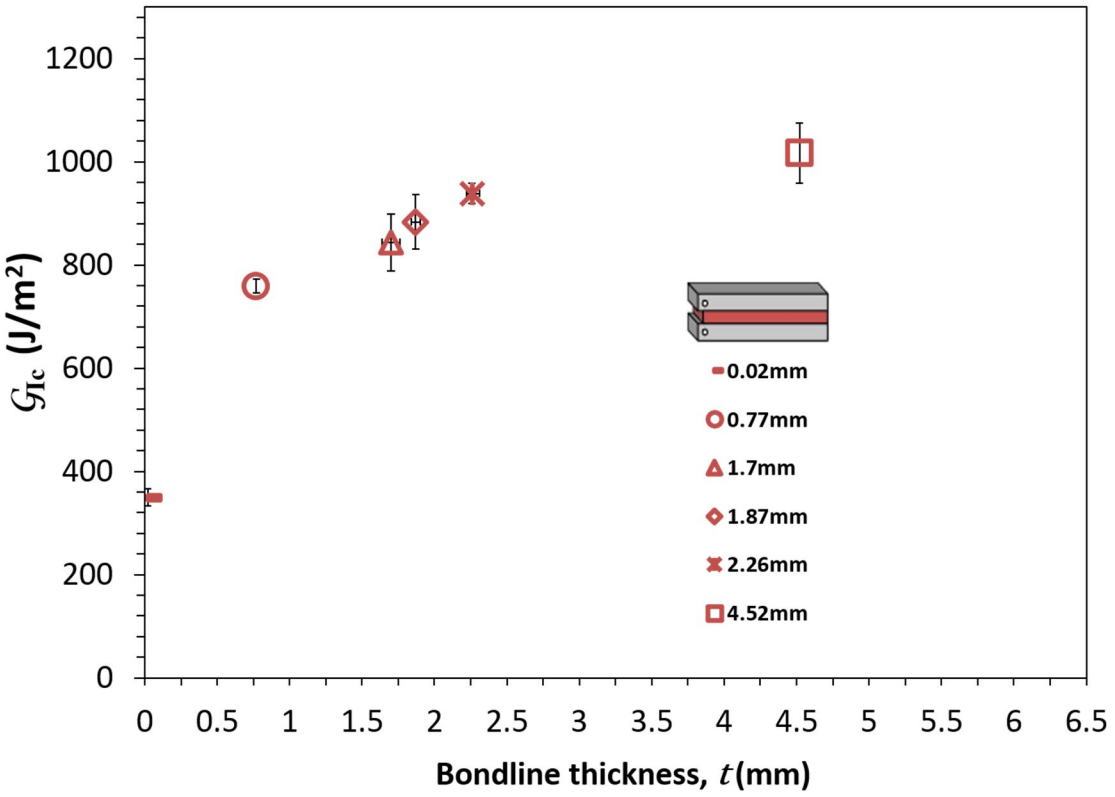

Figure 2-6: Variation of mode I fracture energy with bondline thickness for DCB specimens having a constant bondline thickness

The variation of the fracture energy with the bondline thickness for linearly increasing, linearly decreasing and constant bondline thickness DCB specimens is shown in Figure 2-7. Eight DCB specimens were prepared, four of which had linearly increasing bondline thickness covering a range of 0.25 to 6.12 mm in four intervals (0.25 to 0.69 mm, 0.9 to 1.96 mm, 1.85 to 4.02 mm, 3.16 to 6.12 mm). The remaining four specimens had linearly decreasing bondline thicknesses covering a range of 6.22 mm to 0.22 mm in four intervals (6.22 to 3.11 mm, 4.18 to 1.79 mm, 2.16 to 0.88 mm, 0.65 to 0.22 mm) (Figure 2-7). These bondline thickness ranges were covered in multiple intervals due to geometric restrictions where adherends begin to touch each other at narrow ends of the specimens for a large thickness interval. Some successive intervals had a small overlap in order to characterize the fracture energy at a given bondline thickness via multiple specimens. It was observed that data from eight linearly increasing and linearly decreasing bondline thickness specimens showed good agreement with the data from

constant bondline thickness specimens. A larger deviation was observed for the data obtained from a specimen with the constant bondline thickness of 0.77 mm, though the reason for this is unknown. It was also observed that data obtained from multiple specimens with overlapping thickness ranges showed good agreement with each other.

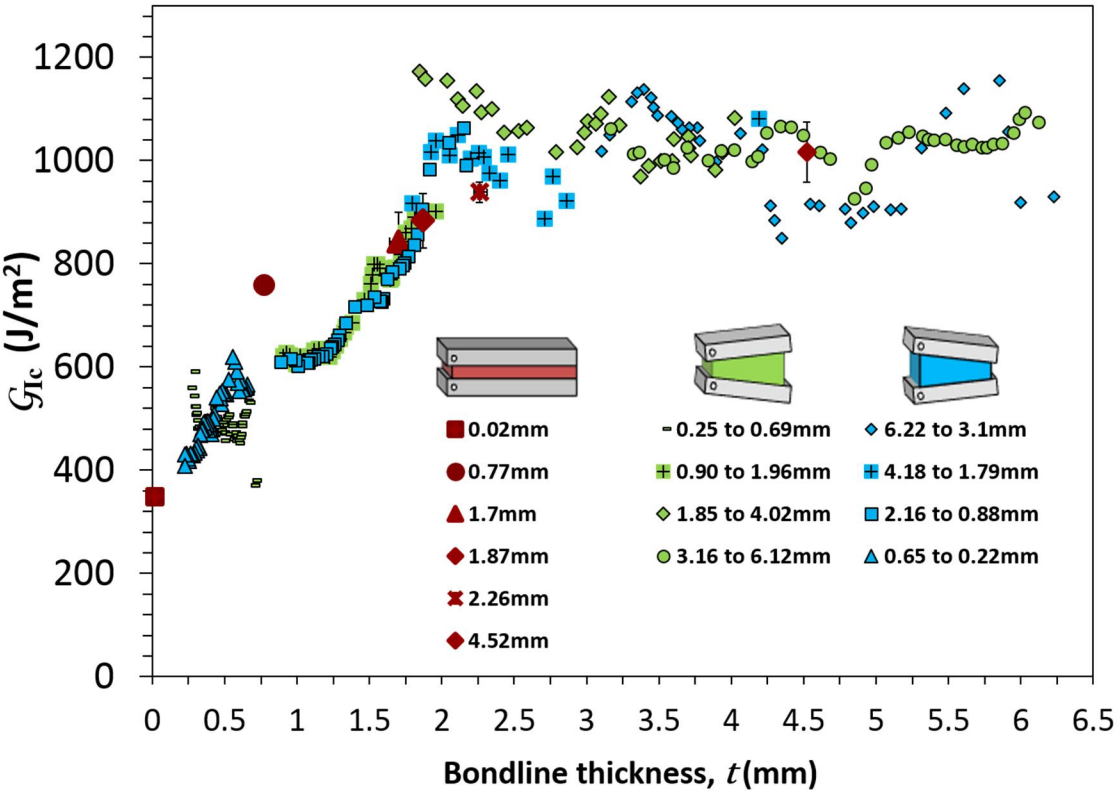

Figure 2-7: Comparison of variation in the mode I fracture energy with bondline thickness between specimens with constant bondline thickness and specimens with linearly increasing and linearly decreasing bondline thickness

In order to test larger bondline thickness intervals using a single specimen, two DCB specimens with a modified geometry were prepared. In these specimens part of the adherend faces were chamfered to accommodate a steeper taper angle (about 3°) (Figure 2-8). In the case of DCB tests with non-chamfered adherends the bondline thickness taper angle was in the range of 0.1° to 1.7°. One DCB specimen had an increasing bondline thickness, covering a bondline thickness range from 0.63 mm to 4.14 mm, and the other specimen had a decreasing bondline thickness, covering a bondline thickness range from 5 mm to 1.36 mm. It was observed that the data obtained from these specimens showed

good agreement with the data obtained from constant bondline thickness specimens. It is interesting to note that these specimens had a bondline thickness gradient much larger than that in the previously tested linearly varying bondline thickness specimens, which covered a similar bondline thickness range in multiple intervals. Thus, increasing the bondline thickness gradient did not appear to affect the results obtained from these modified DCB specimens. It is important to note, however, that the taper angle is still relatively small, about 3°. Significantly steeper gradients may indeed introduce some anomalies.

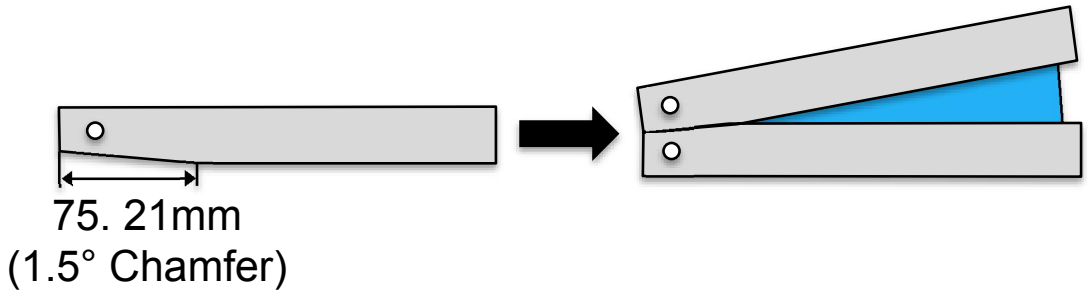

Figure 2-8: Exaggerated schematic representation of a DCB specimen with modified geometry to accommodate large intervals of bondline thickness

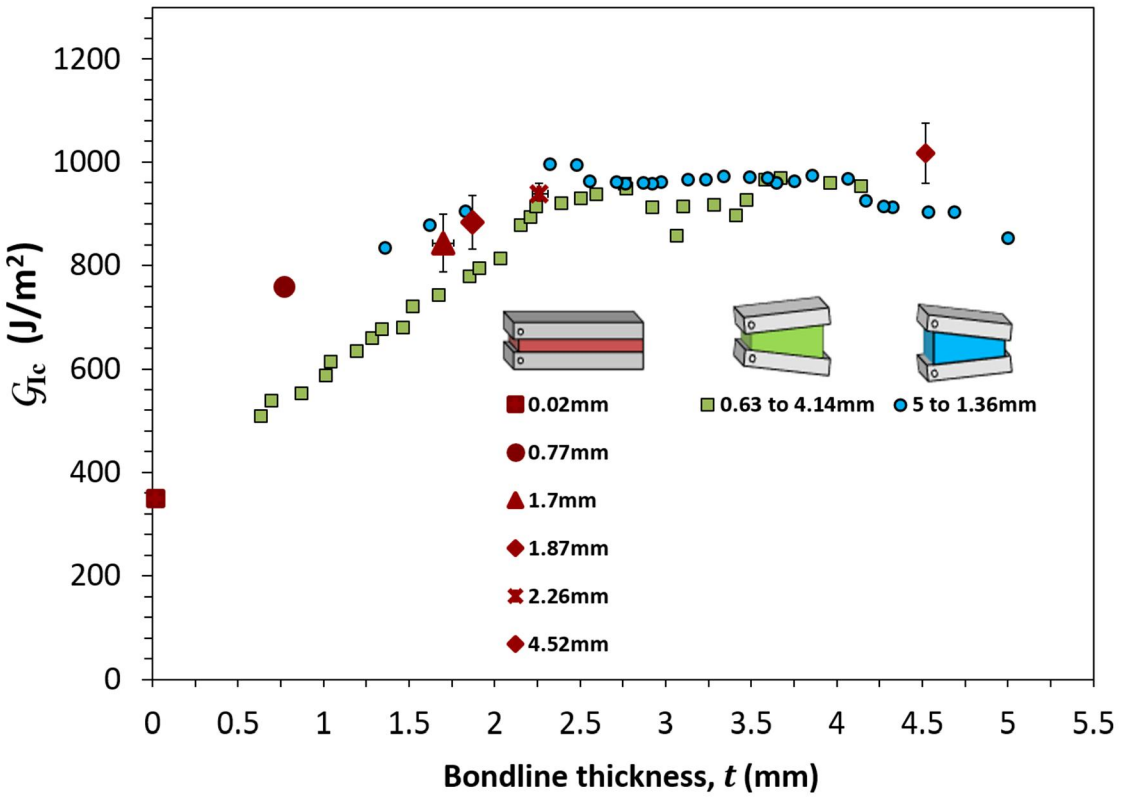

Figure 2-9: Comparison of variation in the mode I fracture energy with bondline thickness between specimens having constant bondline thickness and specimens having linearly increasing and linearly decreasing bondline thickness

For the adhesive system used in this study, no peak in the fracture energy was observed. From the test data on DCB specimens having linearly increasing, linearly decreasing and constant bondline thicknesses, it was observed that fracture energies increased until a bondline thickness of approximately 2.2 mm. Fracture energies plateaued at bondline thicknesses greater than 2.2 mm with no downward trend observed up to the maximum bondline thickness used (4.5 mm). Similar results were reported by Bascom et al. for 30% carboxy-terminated butadiene-acrylonitrile (CTBN) elastomer toughened epoxy system where fracture energy values for DCB specimens increased up to a bondline thickness of about 1 mm ($t = t_m$) and remained constant with a further increase in the bondline thickness up to 2 mm [2]. Several other studies have been reported where fracture energy increases with bondline thickness and reaches a plateau without exhibiting a peak within the investigated bondline thickness ranges [8, 9, 22]. Kinloch et al. have reported that the extent of decrease in the fracture energy value for a

rubber toughened epoxy adhesive for $t > t_m$ was affected by the loading rate, the temperature and the width of the joint. In a more recent study based on a model developed using a critical maximum principal stress at a critical distance ahead of the crack tip as a failure criterion, Matiny et al. suggested that not all adhesives would show a peak in the fracture energy as a function of the bondline thickness. It was suggested that the occurrence of peak in the fracture energy vs. the bondline thickness curve depended upon parameters such as the modulus of the adhesive, the power law hardening exponent for the adhesive and the critical maximum principal stress ahead of the crack tip at a critical distance [10].

As mentioned earlier, it has been reported that the fracture energy of toughened epoxy adhesive joints increases up to a particular bondline thickness, which often corresponds with the plastic zone diameter ($2r_p$) measured using bulk adhesive specimens. Though, it should be noted that in adhesive joints, plastic zone shape and size would be more complex due to constraints imposed by the adherends and change in stress state from plane stress to plane strain through the width of the specimen [15, 23, 24]. The plane stress plastic zone diameter in a bulk adhesive specimen can be predicted using equation 2. In Table 2.1 we have listed average plane strain fracture toughness obtained from the SENB tests, results from compression tests, and average plane stress plastic zone diameter calculated using equation 2. It was observed that for the adhesive system and geometry used in this study, the plane stress plastic zone diameter estimated from bulk adhesive specimens did not correlate well and was about one-fourth the bondline thickness value of about 2.2 mm (t_m) for either constant or tapered bondline thickness DCB specimens, where fracture energy appears to reach a plateau.

Table 2-1: Summary of compression, SENB test results and plane stress plastic zone size

	Compressive modulus (GPa)	Compressive yield strength [(a)] (MPa)	Tensile yield strength[(b)] (MPa)	K_{Ic} (MPa•m$^{0.5}$)	Plastic zone diameter[(c)], $2r_p$ (mm)
Average	2.45	37.77	28.33	1.16	0.51
Standard deviation	0.32	0.63	0.47	0.15	0.13

(a) Calculated using 1% offset

(b) Equal to 0.75·(yield strength in compression) [1]

(c) Calculated using equation (1.2)

2.4 Conclusions

This study proposes and demonstrates the use of a DCB specimen with a linearly varying bondline thickness as a potential combinatorial specimen for characterizing the effect of bondline thickness on fracture energy. For the adhesive system used in this study data from linearly increasing and linearly decreasing bondline thickness specimens generally showed good agreement with that from constant bondline thickness specimens. It was observed that a single DCB specimen with a linearly increasing or linearly decreasing bondline thickness could provide significant insight into the effect of the fracture energy on the bondline thickness. Use of such speciemens will result in a decrease in the testing time and effort needed to study the effect of the bondline thickness on the fracture energy of a toughened epoxy adhesive system. Concerns would be raised, however, if the bonds exhibit a clear R-curve behavior, which could obscure the results of this combinatorial specimen configuration.

2.5 References

[1] A. J. Kinloch and S. J. Shaw, "The Fracture Resistance of a Toughened Epoxy Adhesive," *The Journal of Adhesion,* **12**, 59-77, 1981.

[2] W. D. Bascom, R. L. Cottington, R. L. Jones, and P. Peyser, "The Fracture of Epoxy- and Elastomer-Modified Epoxy Polymers in Bulk and as Adhesives," *Journal of Applied Polymer Science,* **19**, 2545-2562, 1975.

[3] D. L. Hunston, A. J. Kinloch, and S. S. Wang, "Micromechanics of Fracture in Structural Adhesive Bonds," *The Journal of Adhesion,* **28**, 103-114, 1989.

[4] S. Mostovoy and E. J. Ripling, "Effect of Joint Geometry on the Toughness of Epoxy Adhesives," *Journal of Applied Polymer Science,* **15**, 661-673, 1971.

[5] S. Mostovoy, E. J. Ripling, and C. F. Bersch, "Fracture Toughness of Adhesive

Joints," *The Journal of Adhesion,* **3**, 125-144, 1971.
[6] H. Chai, "On the Correlation Between the Mode I Failure of Adhesive Joints and Laminated Composites," *Engineering Fracture Mechanics,* **24**, 413-431, 1986.
[7] S. Azari, M. Papini, and J. K. Spelt, "Effect of Adhesive Thickness on Fatigue and Fracture of Toughened Epoxy Joints – Part II: Analysis and Finite Element Modeling," *Engineering Fracture Mechanics,* **78**, 138-152, 2011.
[8] S. Azari, M. Papini, and J. K. Spelt, "Effect of Adhesive Thickness on Fatigue and Fracture of Toughened Epoxy Joints – Part I: Experiments," *Engineering Fracture Mechanics,* **78**, 153-162, 2011.
[9] V. Cooper, A. Ivankovic, A. Karac, D. McAuliffe, and N. Murphy, "Effects of Bond Gap Thickness on the Fracture of Nano-Toughened Epoxy Adhesive Joints," *Polymer,* **53**, 5540-5553, 2012.
[10] P. Martiny, F. Lani, A. J. Kinloch, and T. Pardoen, "A Maximum Stress at a Distance Criterion for the Prediction of Crack Propagation in Adhesively-Bonded Joints," *Engineering Fracture Mechanics,* **97**, 105-135, 2013.
[11] D. Lee, T. Ikeda, N. Miyazaki, and N. Choi, "Effect of Bond Thickness on the Fracture Toughness of Adhesive Joints," *Journal of Engineering Materials and Technology,* **126**, 14-18, 2004.
[12] S. Mall and G. Ramamurthy, "Effect of Bond Thickness on Fracture and Fatigue Strength of Adhesively Bonded Composite Joints," *International Journal of Adhesion and Adhesives,* **9**, 33-37, 1989.
[13] D. Lee, T. Ikeda, N. Miyazaki, and N. Choi, "Fracture Behavior Around a Crack Tip in Rubber-Modified Epoxy Adhesive Joint with Various Bond Thicknesses," *Journal of Materials Science Letters,* **22**, 229-233, 2003.
[14] A. J. Kinloch, *Adhesion and Adhesives: Science and Technology*. London; New York: Chapman and Hall, 1987.
[15] S. S. Wang, J. F. Mandell, and F. J. McGarry, "An Analysis of the Crack Tip Stress Field in DCB Adhesive Fracture Specimens," *International Journal of Fracture,* **14**, 39-58, 1978.
[16] T. Ikeda, A. Yamashita, D. Lee, and N. Miyazaki, "Failure of a Ductile Adhesive Layer Constrained by Hard Adherends," *Journal of Engineering Materials and Technology,* **122**, 80-85, 2000.
[17] P. Martiny, F. Lani, A. J. Kinloch, and T. Pardoen, "A Multiscale Parametric Study of Mode I Fracture in Metal-to-Metal Low-Toughness Adhesive Joints," *International Journal of Fracture,* **173**, 105-133, 2012.
[18] H. Aglan, Z. Abdo, and S. Shroff, "Fracture and Fatigue Behavior of Scrim Cloth Adhesively Bonded Joints With and Without Rivet Holes," *Journal of Adhesion Science and Technology,* **9**, 177-197, 1995.
[19] B. R. K. Blackman, A. J. Kinloch, M. Paraschi, and W. S. Teo, "Measuring the Mode I Adhesive Fracture Energy, Gic, of Structural Adhesive Joints: The Results of an International Round-Robin," *International Journal of Adhesion and Adhesives,* **23**, 293-305, 2003.
[20] ISO, "Adhesives — Determination of The Mode I Adhesive Fracture Energy of Structural Adhesive Joints Using Double Cantilever Beam and Tapered Double Cantilever Beam Specimens," vol. 25217, ed. Switzerland: ISO 2009.
[21] D. Broek, *Elementary Engineering Fracture Mechanics*. Alphen aan den Rijn:

Sijthoff & Noordhoff, 1978.

[22] L. F. Kawashita, A. J. Kinloch, D. R. Moore, and J. G. Williams, "The Influence of Bond Line Thickness and Peel Arm Thickness on Adhesive Fracture Toughness of Rubber Toughened Epoxy–Aluminium Alloy Laminates," *International Journal of Adhesion and Adhesives,* **28**, 199-210, 2008.

[23] S. R. Ranade, "Performance and Durability of Adhesive Joints," Ph. D., Macromolecular Sci. and Eng., Virginia Polytechnic Institute and State University, Blacksburg,VA, USA, To be published.

[24] S. R. Ranade, Y. Guan, D. Ohanehi, J. Dillard, R. C. Batra, and D. A. Dillard, "A Tapered Bondline Thickness Double Cantilever Beam (DCB) Specimen Geometry for Combinatorial Fracture Studies of Adhesive Bonds," presented at the Adhesion Society Meeting, Daytona, USA, 2013.

3 Fracture performance and the interaction of a propagating crack with locally weakened interfaces in an adhesive joint

3.1 Introduction

Identifying and understanding the locus of failure in an adhesive joint is important for interpreting bond performance. The resulting locus of failure or crack path selection in an adhesive joint is complex, arising from an interaction of the spatially varying stress state ahead of a growing crack tip with the material system's resistance to failure, which can depend on the location within the bond [1-5]. Though a number of studies have been carried out to understand the effects of joint geometry, fracture mode mixity, and material properties on crack path selection and the performance of adhesive joints, relatively few studies have probed crack path selection and adhesive joint performance in the presence of localized interfacial defects [6-11]. During the manufacture of adhesive joints, it is difficult to completely eliminate defects in adhesive joints [12]. These defects can be in the form of voids, improperly mixed or cured adhesive in some locations, adherend surface contaminations, etc. The presence of such defects can lead to weakened interfaces with reduced stiffness or load carrying capabilities or disbonds that are incapable of resisting certain tractions at the interface of an adhesive joint. Most of the previous studies that probe the effect of defects on the performance of an adhesive joint are based on strength-based tests such as lap shear tests. In these studies a defect is typically introduced by placing a thin Teflon shim of desired shape and size at the adhesive-adherend interface. Schonhorn et al. reported some of the early findings in this area by using a low-density polyethylene adhesive and a brittle epoxy adhesive [13, 14]. They observed that the strength of such lap shear joints was governed by the net bonded area rather than the edge effects for a soft adhesive while edge effects were significant when a brittle adhesive was used [13]. Berry et al. reported similar findings, where lap shear strength was found to be independent of the size of circular defect placed in the middle of the overlap, for a joint comprised of an epoxy adhesive [15]. Recently, Karachalios et al. reported that the effect of defect size on the strength of the lap shear joint is a complex function of relative properties of adhesive and adherends [12]. For cases where the edge effects influenced the failure, changes in the size of a centrally located defect did not

significantly affect the joint performance. While for cases where the entire bond area influenced the failure, the size rather than shape of artificial defects affected the overall strength of the adhesive joint. Several studies have been reported that characterize the stress distribution in an overlap of the lap shear joints containing disbonds using shear lag type models [16-20]. Chadegani et al. used a first-order shear deformation plate theory to characterize the stress state in a lap shear joint having a void [21].

In an adhesive joint, the disbonds which contain traction-free surfaces can be detected using non-destructive techniques, however, it is difficult to detect weakened interfaces, where there are no traction-free surfaces [22]. There are very few studies available on the effect of localized weak interfaces (interfacial defects with no traction-free surfaces) on the fracture properties of adhesive joints or on the interaction of a growing crack tip with localized weak interfaces [7, 10, 11, 22, 23]. This is partly due to difficulties in creating well-defined localized weak interfaces (rather than a disbond with traction-free surfaces) having a controlled shape, size and failure properties.

Using an interferometric technique Heslehurst et al. observed that weakened interfaces caused variations in adherend fringe patterns indicating smaller out of plane deformations for weakly bonded adherends when compared to a joint having disbands [22]. Chan et al. explored the influence of patterns containing the periodic variation of weak and strong interfaces on the adhesion of soft materials [6, 23]. Budzic et al. studied the crack front propagation and fracture properties along the heterogeneous interfaces using an elastic/fragile epoxy adhesive. They observed that overall fracture energy varied non-linearly with the change in weak/strong interfacial fractions [10, 11].

Apart from the insights about robustness of the adhesive joints, better understanding of fracture resistance and crack path selection in the presence of localized interfacial defects might lead to adhesive joints with tunable failure locus and resistance to fracture. Such joints might be useful in applications that require controlled disassembly of adhesive joints, such as the packaging industry, and perhaps other fields where recycling and reuse options offer enhanced sustainability. This paper investigates adhesive fracture performance and crack path selection in double cantilever beam (DCB)

specimens containing well-defined, quantifiable localized interfacial defects created using physical vapor deposition technique.

3.2 Experimental

3.2.1 DCB Tests

All the DCB specimens in this study were prepared using 6061-T6511 aluminum bars as adherends, having dimensions of 305 mm × 25.4 mm × 12.7 mm. Holes were drilled at one end of each aluminum bar to accommodate loading pins. The bonding surfaces of the adherends were then abraded with #220 sandpaper and subjected to a base-acid surface treatment previously described in the literature [3]. The joints consisted of two such adherends, but for most specimens, one of the adherends was subjected to a subsequent step to form locally weakened regions on the bonding surface. Several patterns of local weak interfaces were created on base-acid treated aluminum adherend surfaces utilizing physical vapor deposition (PVD) of copper (99.99% pure). Physical vapor depositions were carried out using a Kurt-Lesker PVD-250 instrument. Acrylic masks (1.27 mm thickness) with desired patterns were prepared using an Epilog laser cutter (64W) instrument. Prior to use acrylic masks were cleaned with compressed nitrogen gas and acetone. Physical vapor depositions were carried out at 25°C in a clean room environment at 6.6 x 10^{-4} Pa pressure and at a rate of about 0.25 nm/sec. The final thickness of the deposited copper films was about 250 nm. Figure 3-1 summarizes the procedure used to create libraries of patterns, containing localized weak interfaces for a given specimen. As discussed in the later section, each copper deposited region within a pattern forms a local weak interface due to poor adhesion between the deposited copper and the aluminum adherends.

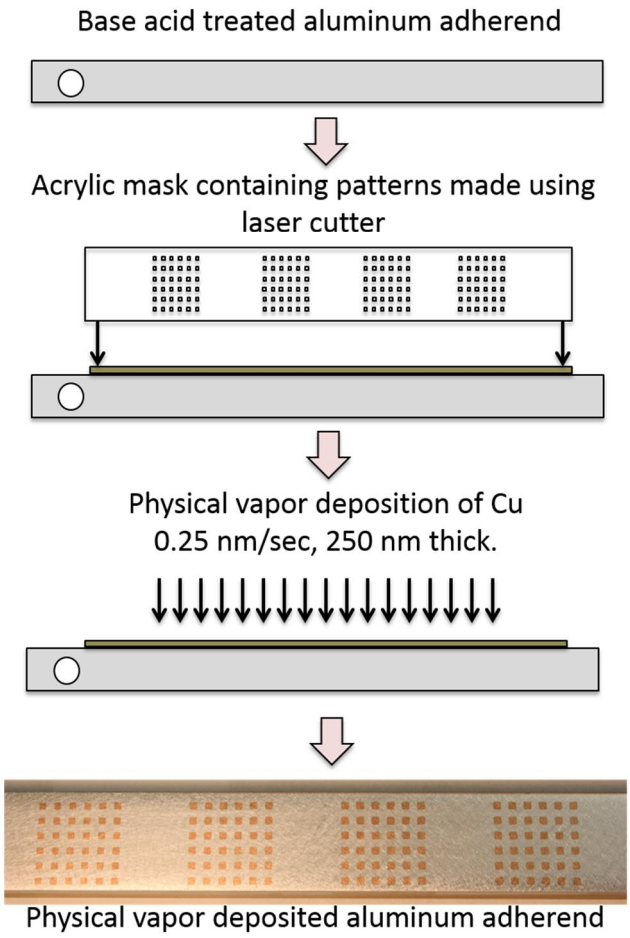

Figure 3-1: Procedure used to create patterns with local weak interfaces on the bonding surface of base-acid treated aluminum adherends

Figure 3-2 summarizes dimensions of the weak interface patterns for all tested specimens and the crack grew from left to right in subsequent DCB testing. Except for specimens of type A and B, one specimen was tested from each specimen type.

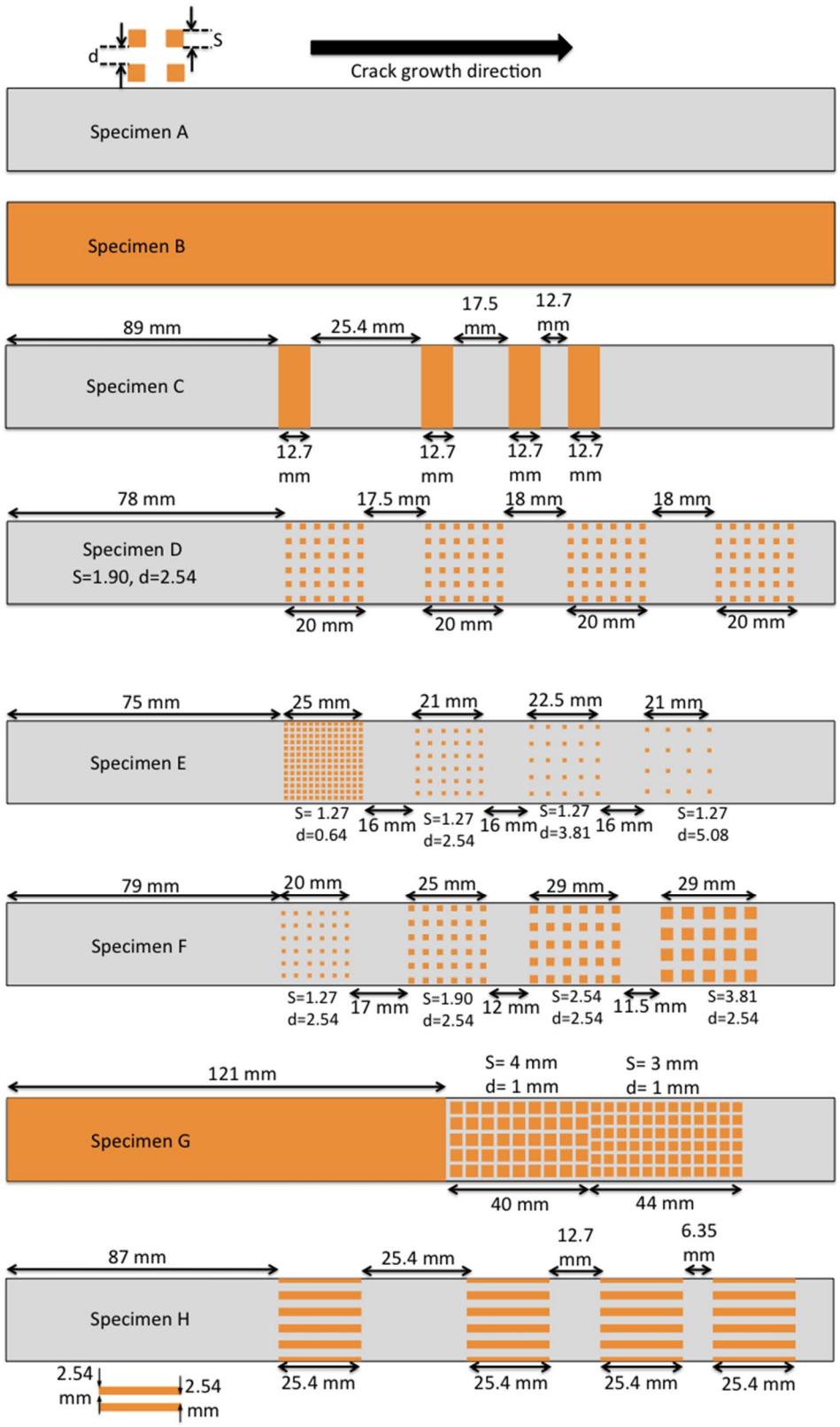

Figure 3-2: Schematic representation and dimensions of weak interface topology in specimens used in the study

A commercially available LORD^{TM} 320/322 structural epoxy adhesive was used to bond the prepared aluminum adherends. For all the specimens, a bondline thickness of about 0.2 mm was maintained by placing spacers at each end of the specimen during assembly. As per manufacturer recommendation specimens were cured for 14 hours at room temperature and post-cured at 60°C for 3 hours. All DCB tests (mode I and mixed mode) were carried out at a total crosshead rate of 0.1mm/min. A 5800R Instron tensile testing machine was used for mode I tests while mixed mode tests were carried out using a dual actuator load frame, details of which have been reported elsewhere [24, 25]. A mode mixity angle (ψ) of 60° was used in all mixed mode tests. Procedure used for calculation of mode mixity angle during mixed mode DCB tests in dual actuator load frame has been described earlier [24]. Mode I and mixed mode fracture energies were calculated using the corrected beam theory (Equation 3.1) [26-28].

$$G_{Ic} = \frac{3P\delta}{2B(a+\hat{a})}F \tag{3.1}$$

G_{Ic} is mode I fracture energy
P is load measured by load cell
a is crack length
δ is crosshead displacement at crack length a
F is large displacement correction
B is width of the specimen
$\hat{a}$ is the crack length correction for a beam that is not perfectly built in

During the DCB tests, crack lengths were measured by visual observation of the crack tip using a magnifying glass. This limits the number of data points that can be gathered for a given specimen. For a DCB specimen with drilled holes, flexural modulus relates with the compliance of the specimen and the measured crack length through Equation 3.2 [28].

$$E_f = \frac{8(a+\hat{a})^3}{CBh^3} \tag{3.2}$$

where, $C = \frac{\delta}{P}$

Rearranging Equation 3.2 leads to,

$$C = \left[\frac{8}{E_f b h^3}\right](a + \hat{a})^3 \tag{3.3}$$

Thus using Equation 3.3 by plotting measured compliances at visually observed crack lengths, a $C^{1/3}$ vs. crack length relationship was obtained for a given specimen (with $R^2 > 0.99$ for all specimens). Figure 3.3 shows a representative $C^{1/3}$ vs. crack length relationship obtained using Equation 3.3.

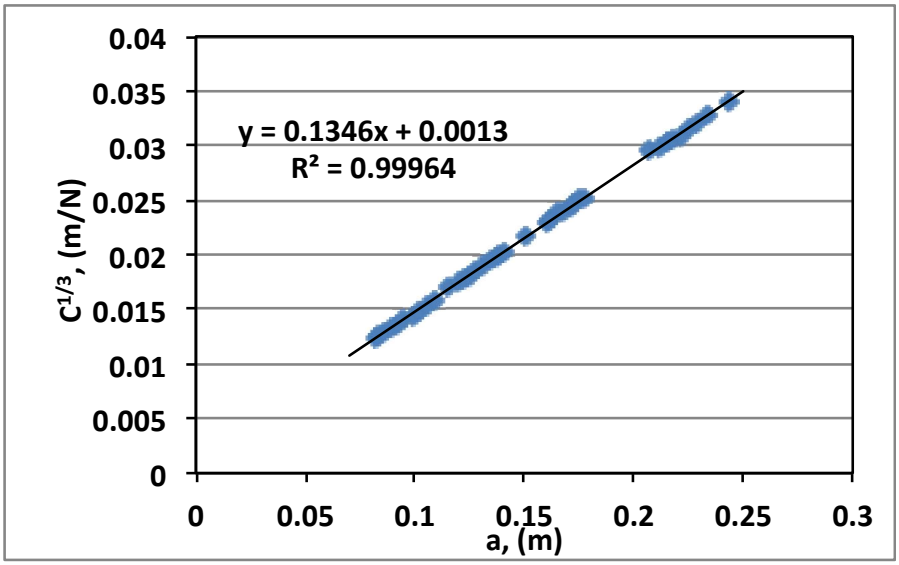

Figure 3-3: $C^{1/3}$ vs. crack length data from specimen A

Since load and beam deflections (crosshead displacements) were measured at every 0.1 sec during the tests; load, crosshead displacement and compliance vs. crack length relationship (compliance determined using Instron measured loads and crosshead displacements and crack lengths from visually observed crack tip location) using Equation 3.3 were then used to estimate crack lengths over an entire test. The estimated crack lengths were in reasonable agreement with the visually measured crack lengths. Using Equation 3.1 fracture energies were then calculated from visually observed crack lengths as well as from estimated crack lengths. In the following sections, fracture energy

data based on experimentally measured crack lengths is shown using red data markers, while the fracture energies calculated using estimated crack lengths (Equation 3.3) are shown using blue colored data markers.

3.2.2 Single edge notch bend (SENB) tests

SENB tests were used to calculate the plane strain fracture toughness (K_{Ic}) of the bulk adhesive, following the ASTM D 5045-99 standard. Specimens were cast using silicone molds and cured at the same conditions as those used for the DCB test specimens. The SENB specimens had dimensions of about 57.1 mm x 12.7 mm x 6.3 mm (length x width x thickness). Specimens were pre-cracked by driving a fresh, sharp razor blade by gentle tapping such that the crack tip was a few millimeters ahead of the razor blade tip. Due to the lack of distinguishing features on the fractured surfaces of the SENB specimens, it was not possible to unambiguously measure the length of the pre-crack from fractured specimens. Crack lengths were measured using high-resolution images of the pre-cracked specimens and**,** digital image analysis software (Photron FASTCAM Analysis, Photron USA Inc., San Diego, CA, USA). Pre-cracked specimens were then mounted crack down on a 3-point bend fixture in an Instron model 5500R and loaded at a constant crosshead rate of 0.1 mm/min. The distance between the supporting rollers in the 3-point bend fixture was 4 times the width of the specimens. Plane strain fracture toughness values were calculated per ASTM D 5045-99 utilizing tensile yield strength ($\sigma_{y\ tensile}$) values estimated from compression tests, as described in the next section [29]. The plane strain plastic zone size, r_p, was estimated using the following expression (Equation 3.4) [30].

$$\text{Plastic zone size} = \frac{1}{2\pi}\left(\frac{K_{Ic}}{\sigma_{ytensile}}\right)^2 \tag{3.4}$$

3.2.3 Compression tests

Dogbone specimens tested in tension to obtain tensile yield strength values failed in a brittle manner before yielding, precluding the use of tensile tests for obtaining the tensile yield strength values. For a toughened epoxy system, it has been reported that the tensile yield strength is approximately 0.75 times the compressive yield strength [29]. For

compression tests, three cylindrical specimens were cast and then machined to a height/diameter ratio between 2 to 1.5. The three specimens had a diameter in the range of 10.16 mm to 15.24 mm. The specimens were loaded between polished steel plates in an Instron 5500R test frame at a 0.1mm/min test rate. The load values were converted into the nominal axial stress by dividing the load by the original cross-sectional area of the specimen. The change in the specimen length was obtained through crosshead movement and converted to the average axial strain by dividing it by the original specimen length. Compressive yield strength ($\sigma_{y\ compresion}$) was calculated from the stress-strain curves by using a 1% strain offset. Compressive modulus values were obtained from the slope of the linear part of the stress-strain curve. Compressive stress vs. strain curves corrected for a toe region (artifact caused by take up of slack, alignment or seating of the specimen) using guidelines from ASTM D 695 – 02a standard are shown in Figure 2-4.

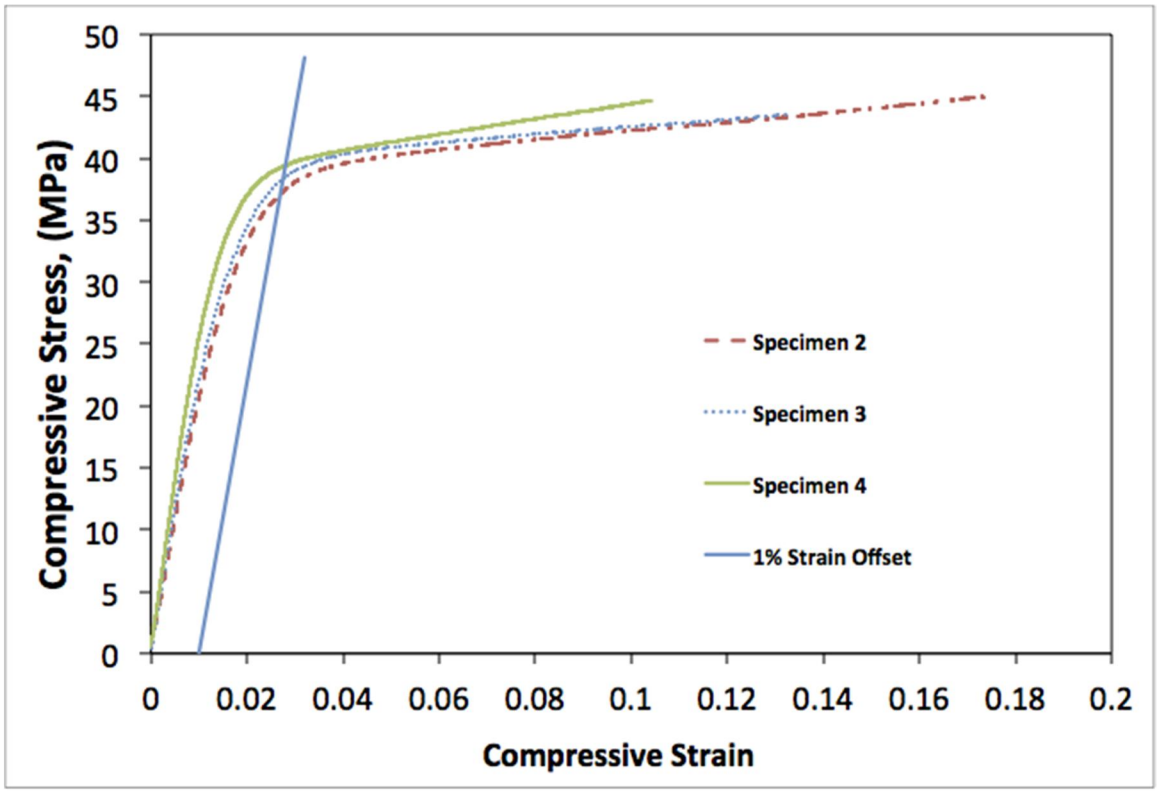

Figure 3-4: Engineering compressive axial stress vs. compressive axial strain curves from compression tests

3.3 Results and Discussion

3.3.1 Mode I test results

Specimens of type A and B were control specimens. Figure 3-5 shows representative failure modes and a schematic representation of observed failure locus for specimens of type A, a DCB specimen having no copper coating on either adherend bonding surface and for specimens of type B with one adherend bonding surface having a PVD copper coating (100% coverage). Upon visual examination of the failure surfaces, it was observed that the specimens of type A showed a cohesive failure within the adhesive layer while specimens of type B showed an apparent interfacial failure at the copper/aluminum interface. Repeatability of the observed failure modes was confirmed by testing four DCB specimens of type B and two specimens of type A. Representative mode I DCB tests results for specimens of type A and B are shown in Figure 3-6. In DCB tests on specimens of type B, the crack propagated at relatively high speeds through the copper/aluminum interface, thus very few data points could be gathered. It was observed that specimens of type B with apparent interfacial failures at the copper/aluminum interface had interfacial fracture energy of about 20 J/m^2 (calculated based on Equation 3.1). These fracture energies were much lower than the average fracture energy (for multiple points on the same specimens) of 464 J/m^2 obtained for cohesive failures in specimen A. Thus, when coupled with exposure masks, the PVD technique enabled the preparation of locally weakened interfaces having an interfacial fracture energy that was about 4.5% of the fracture energy of an adhesive joint having good interfaces.

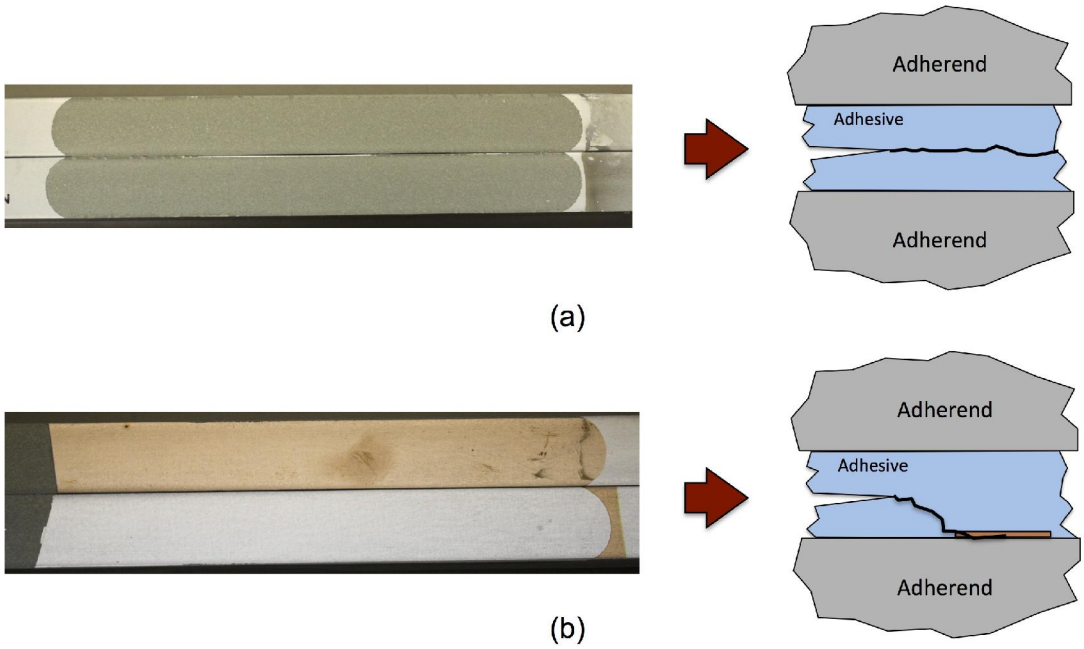

Figure 3-5: Failure surfaces for mode I DCB tests (a) cohesive failure within adhesive layer for the specimen A (control specimen), (b) apparent interfacial failure at copper/aluminum interface for a DCB specimen with PVD copper coating on the entire surface of one adherend (specimen B).

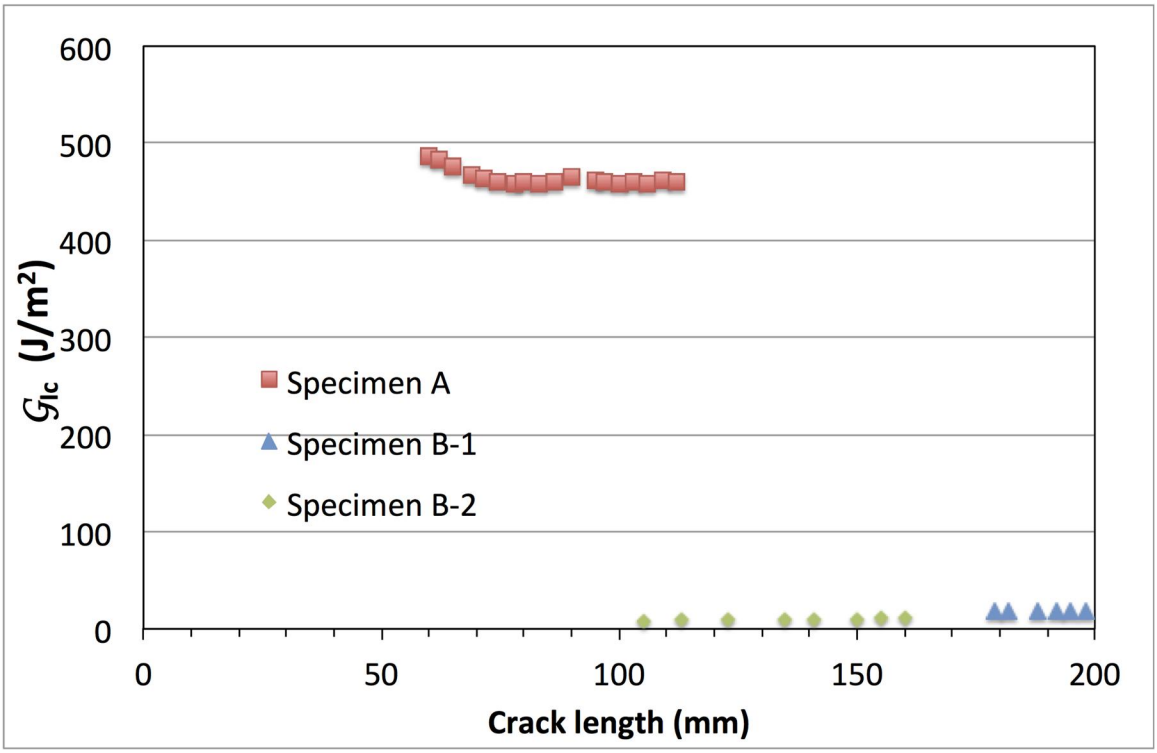

Figure 3-6: Mode I DCB test results for control specimens, specimen A with no copper coating on either adherend and for B specimens with one adherend having a PVD copper coating over the entire bonding surface

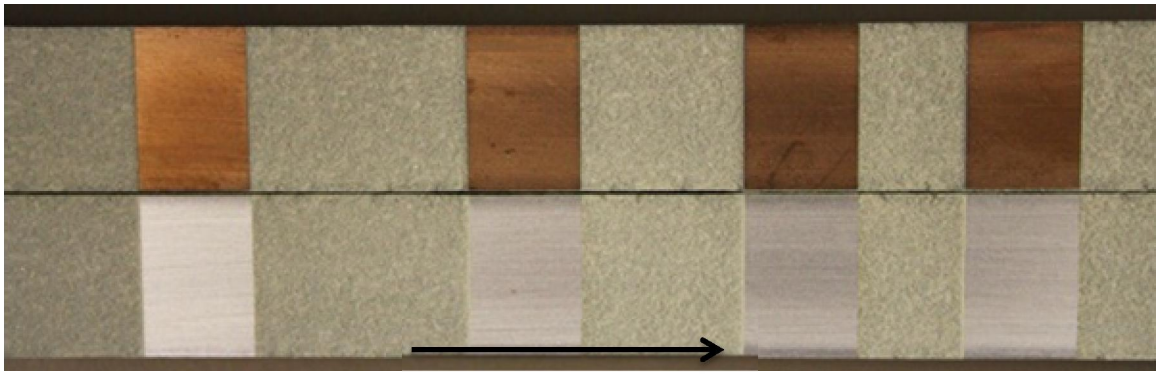

Figure 3-7: Failure surfaces of specimen C, copper covered region

As shown schematically in Figure 3-2, the specimen of type C had four localized weak interfaces covering the entire width of the specimen that were separated by control regions. The specimen with type C pattern, when tested in mode I, would offer insights into the performance of an adhesive joint in which a propagating crack is approaching a localized weak interface that covers the entire width of the adherend. Also, the control region length between successive localized weak interfaces was decreased, allowing us to probe the effect of separation distance between weakened interfaces on the fracture performance of the adhesive in the control regions. Figure 3-7 shows failure surfaces of the C type specimen when tested under mode I conditions. It was observed that similar to failure modes shown schematically in Figure 3-5, copper deposited regions in the C type specimen showed an apparent interfacial failure at copper/adherend interface, while regions without copper depositions (control regions) showed a cohesive failure. Figure 3-8 shows mode I test results for the specimen of type C with localized weak interface regions highlighted in light copper red color (Here, crack length is based on the visually observed crack tip at the edge of the specimen, though actual crack length will vary somewhat across the width of the specimen.). It is observed that the fracture energy of the adhesive joint was not affected until the crack tip was within about 8 to 10 mm from the first localized weak interface. At this distance and upon further loading of the specimen a reverse R-curve type behavior was observed and eventually the crack became unstable, leading to an unstable crack growth till the end of the first weak interface region. Apparent R-curve type behavior was observed upon further loading of the specimen, wherein the fracture energy of the specimen increased with an increase in crack length

and reaching a maximum [31]. Similar behavior was observed as the crack tip approached the next weak interface regions.

The R-curve or resistance curve trend has been observed in the fracture analysis of materials such as composites and polymers [31]. Crack propagation in toughened structural adhesive joints begins with the energy dissipation mechanisms such as cavitation, micro-cracking, shear yielding etc. These mechanisms lead to growth of a plastic zone that consists of yielded material and distributed micro-cracks [32]. With further loading of the specimen, the micro-cracks coalesce and form a macro-crack, which then propagates with formation of new micro-cracks and the plastic zone into the adhesive layer [33, 34]. Thus during initial stages of fracture, the plastic zone continues to expand, leading to a progressive toughening of the joint as the input strain energy is dissipated by the plastic deformation. This process results in the fracture resistance curve (R-curve) of fracture energy versus the crack length. Eventually, the plastic zone reaches a steady-state size and the fracture energy becomes constant.

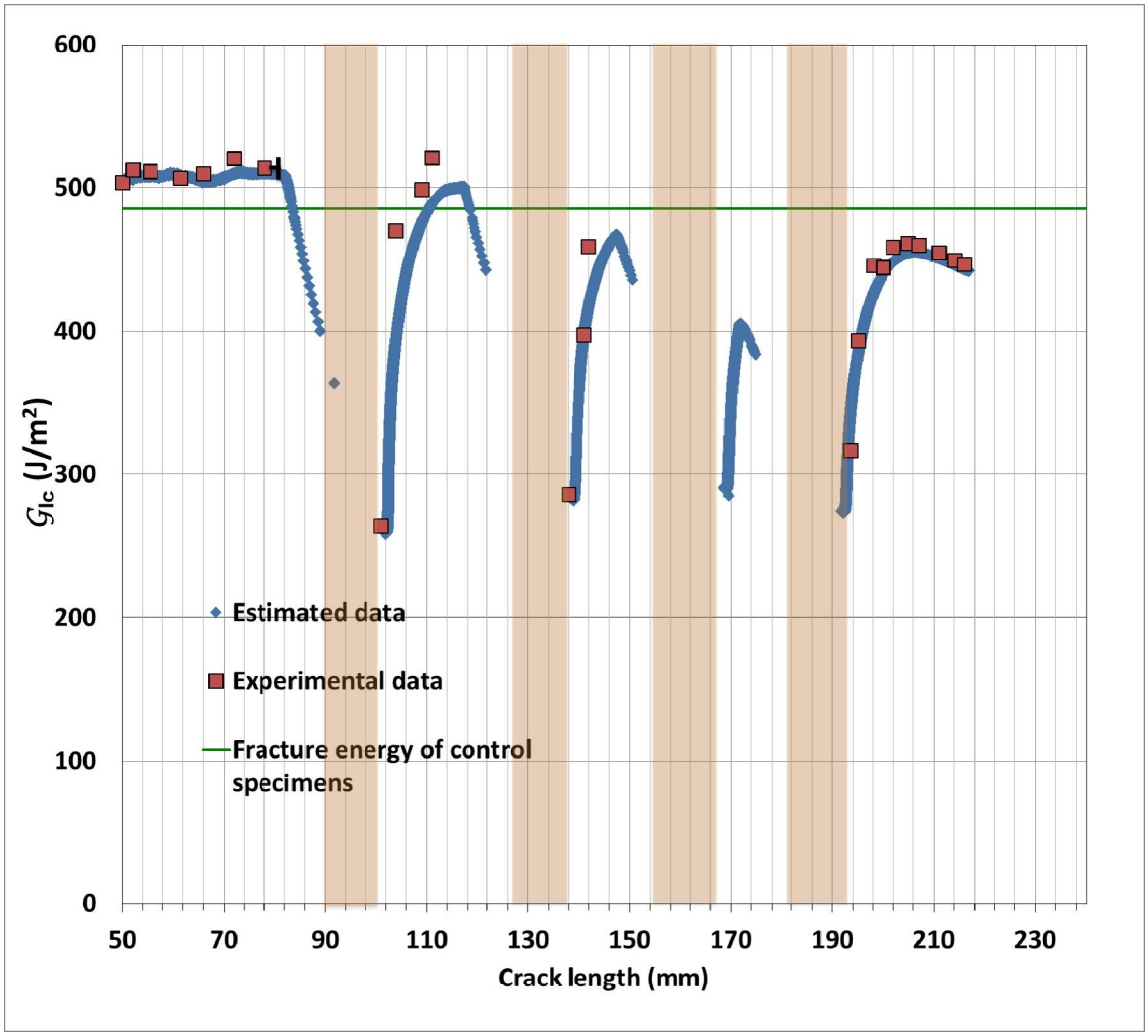

Figure 3-8: Mode I DCB test results for specimen C

These observations indicate that the crack propagation behavior is influenced over a considerable distance both preceding and in the wake of weak interface regions that cover the entire width of the specimen. At this point, the distances mentioned above are tentative in nature as the location of crack is being inferred from observation of crack tip on the bondline surface. In light of the possible thumbnail shaped crack tip, the crack length at the center of the specimen may be longer than the crack length at the edge of the specimen. As crack lengths were measured at the edge of the specimen, the actual distance around pattern regions over which the crack became unstable might be smaller than that mentioned above. A rough estimate of the crack tip shape was obtained using a dye-penetrant ink during a separate mode I DCB tests on specimens of type A, which did not have copper deposited surfaces. The distance between the crack tip around the central

location in a specimen and at the edge where crack lengths were measured, was about 2 mm. The error bar on a single data point in Figure 3-8 and in subsequent figures represents this distance. For clear representation of the data, all fracture energy data points were not marked by the error bars.

In the specimen of type C, for a crack tip approaching the weak interface a reverse R-curve type trend was observed where fracture energy decreased with the growing crack length and the crack became unstable few millimeters ahead of weak interface regions. The occurrence of reverse R-curve type trends might be due to plastic zone size evolving towards the smaller steady state dimensions as the crack tip nears the weak interface. The unstable crack growth might be due to interplay of the available strain energy owing to the toughness of the adhesive in good interface regions with the fracture energy of the weakened interface at above mentioned distances. When the distance between the crack tip and the weak interface becomes sufficiently small, the resulting tractions at weak interfaces are insufficient and the crack suddenly advances along the weakened interface in a rapid release of available strain energy. The unstable crack growth would continue till the adhesive in front of the growing crack tip is able to sustain the remaining stored elastic energy. It must be noted that dynamic effects associated with the unstable crack growth would also affect the distance over which a crack would grow in an unstable manner. In the specimen of type C, the length of the control regions between successive weak interfaces was decreased. In the first control region the maximum at the end of the R-curve was similar to the fracture energy of the control specimen (type A). Interestingly, within the second and third control regions, the maximum attained by the fracture energy at the end of the R-curve decreased with the length of the control regions.

Unlike the specimen of type C, the specimens of type D, E and F did not have a single continuous weak interface covering the entire width of the specimen, but each specimen type had four patterns of weak interfaces separated by control regions. Within all the patterns in each specimen type, good interface regions separated discreet localized weak interfaces throughout the width of the specimen. Details of the size of the localized weak interfaces (s) within patterns, separation distances within (d) and between successive patterns are provided in Figure 3-2. All four patterns in the specimens of type

D had identical dimensions. In the specimen of type E the separation distance (d) between the local weak interfaces within a pattern was increased in successive patterns, while keeping the local weak interface size (s) constant for all four patterns. Control regions with similar lengths separated all four patterns in specimens of type D and E. In specimens of type F, the size of the local weak interface (s) in a pattern was increased for successive patterns, keeping a constant separation distance (d) between squares for all four patterns within the specimen. In specimens of type F the distance between the successive patterns was not similar as in specimens of type D and E but this distance was decreased in successive patterns.

Figure 3-9 shows failure surfaces of specimen type D, E and F when tested under mode I conditions. It was observed that, similar to failure modes shown schematically in Figure 3-2, copper deposited regions showed apparent interfacial failures at the copper/adherend interface, while regions without copper depositions showed cohesive failure within the adhesive layer. Specimens of type D had four patterns of weak interfaces. All patterns had identical dimensions (s, d) and the length of the control regions between successive patterns was similar.

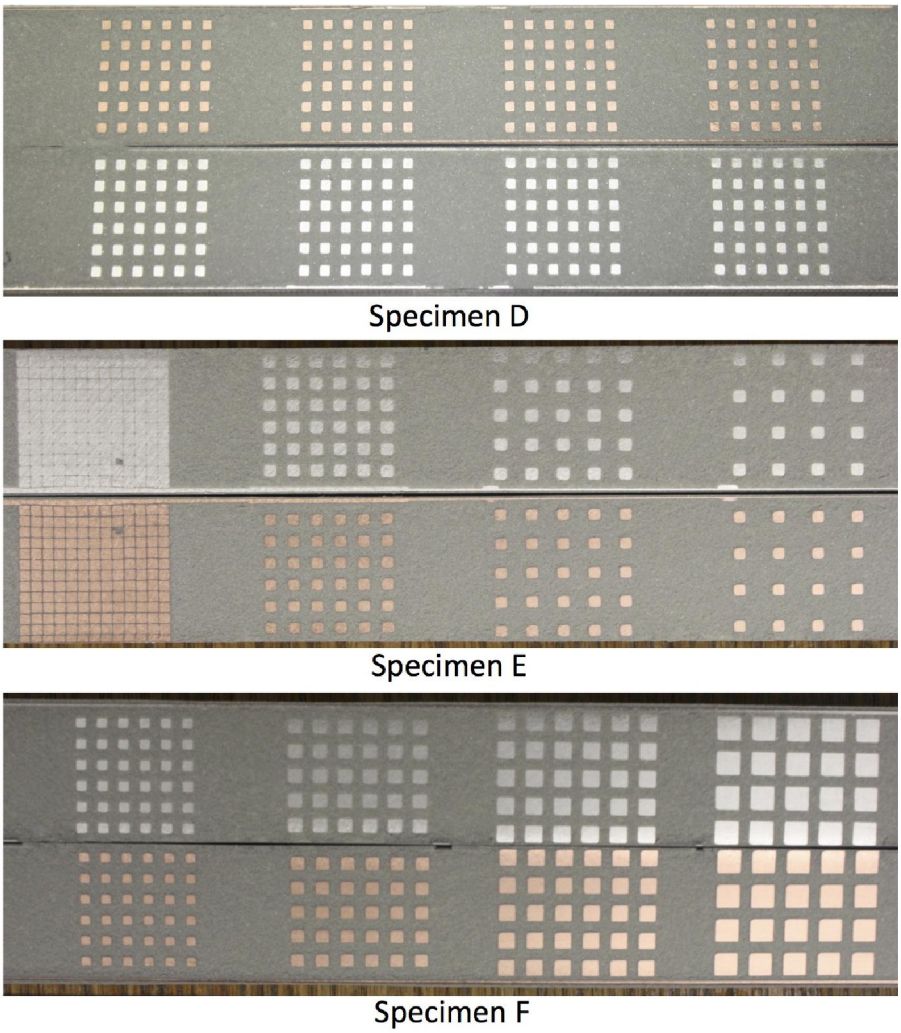

Figure 3-9: Failure surfaces of specimen D, E and F tested in mode I conditions

Figure 3-10 to Figure 3-12 show mode I test results for specimen types D, E and F. Patterned regions are highlighted using copper color and error bar attached to the first visually observed crack length shows the likely uncertainty in the crack length measurements owing to the thumbnail shaped crack tip. For clear representation, only one data point based on visually observed crack length is marked with an error bar though similar crack length uncertainty exists for all the crack length data points. In all three specimens, a reversed R-curve type of behavior was observed for the crack tip approaching a patterned region where fracture energy starts to decrease about 10 mm before the crack tip reaches a patterned region and then appears to reach a plateau within a given patterned region. An R-curve type of behavior is observed as the crack tip leaves the patterned region and enters the control regions between successive weak interfaces.

The R-curve type of trend continues in the control region till the fracture energy reaches a maximum. For the specimen of type D and E, the maximum fracture energy observed in successive control regions between patterns was reasonably constant and was similar to the fracture energy of specimen of type A. For specimen of type F, the maximum fracture energy observed in successive control regions between patterns (strong interface regions) decreases with decrease in the length of the control regions indicating that in such cases control regions were too short to fully develop the R-curve. These observations indicate that the presence of local weak interface regions influences the fracture energy of an adhesive joint over a considerable distance around weak interface regions, about 10 mm for the geometry and materials used in this study. This is probably due to the insufficient tractions at the weak interfaces influencing the size (and energy dissipation) of the plastic zone that can be formed ahead of the crack tip. Though as mentioned previously in light of the expected thumbnail shaped crack tip, the actual distance around pattern regions over which the fracture energy is influenced might be slightly smaller than that mentioned above. Also, it was observed that the minimum or a plateau fracture energy generally correlated with the fraction of good interface area within a pattern, as also shown in the figures. In specimen type D to F an appearance of a minimum or a plateau in the patterned regions having a range of s and d values hints towards the overall reduction in the fracture energy as the net weakened area increases rather than local contributions that arise due to micro-mechanisms at crack tip. This will be discussed in detail in a following section.

Many studies have shown that for a thin bondline thickness DCB specimen, where height of the plastic zone is in the order of or greater than the bondline thickness of the specimens, local tensile stresses ahead of the crack tip act over a considerably longer distance than compared with bulk adhesive specimens [35-39]. Based on such studies, it has been suggested that for thin bondline DCB specimens bonded with a toughened structural epoxy adhesive, the plastic zone ahead of the crack tip can be considerably longer in length compared to the plastic zone length in bulk adhesive specimens [29, 37].

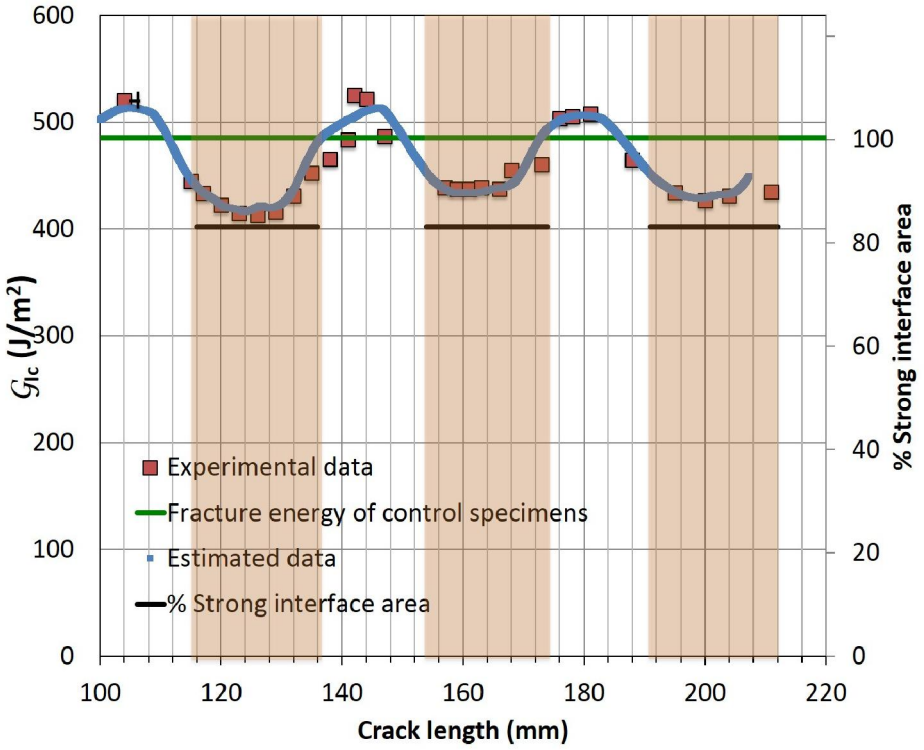

Figure 3-10: Mode I DCB test results for specimen D

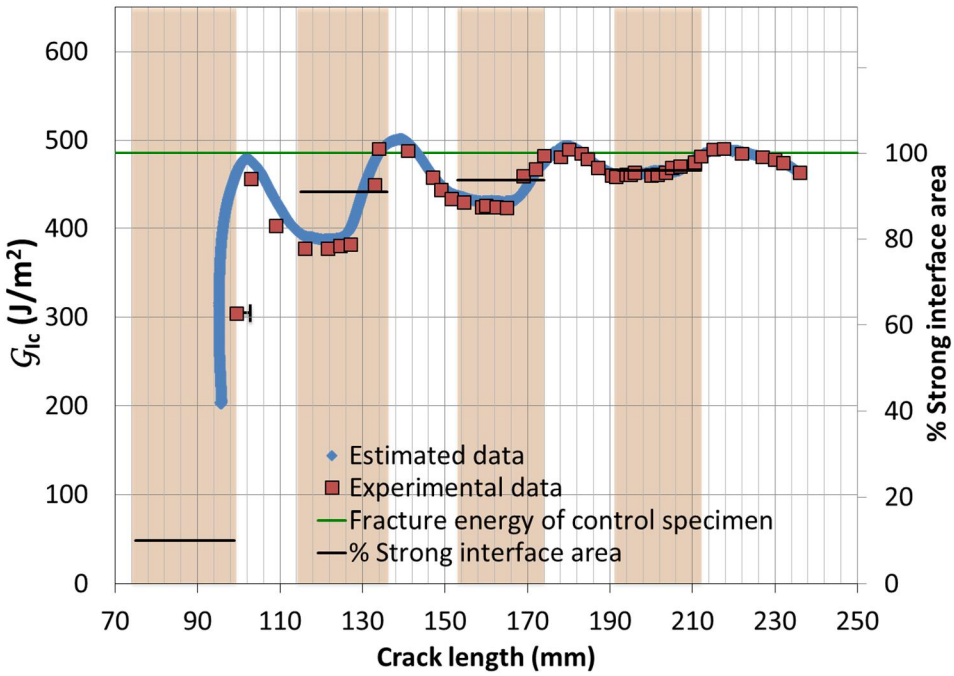

Figure 3-11: Mode I test results for specimen E

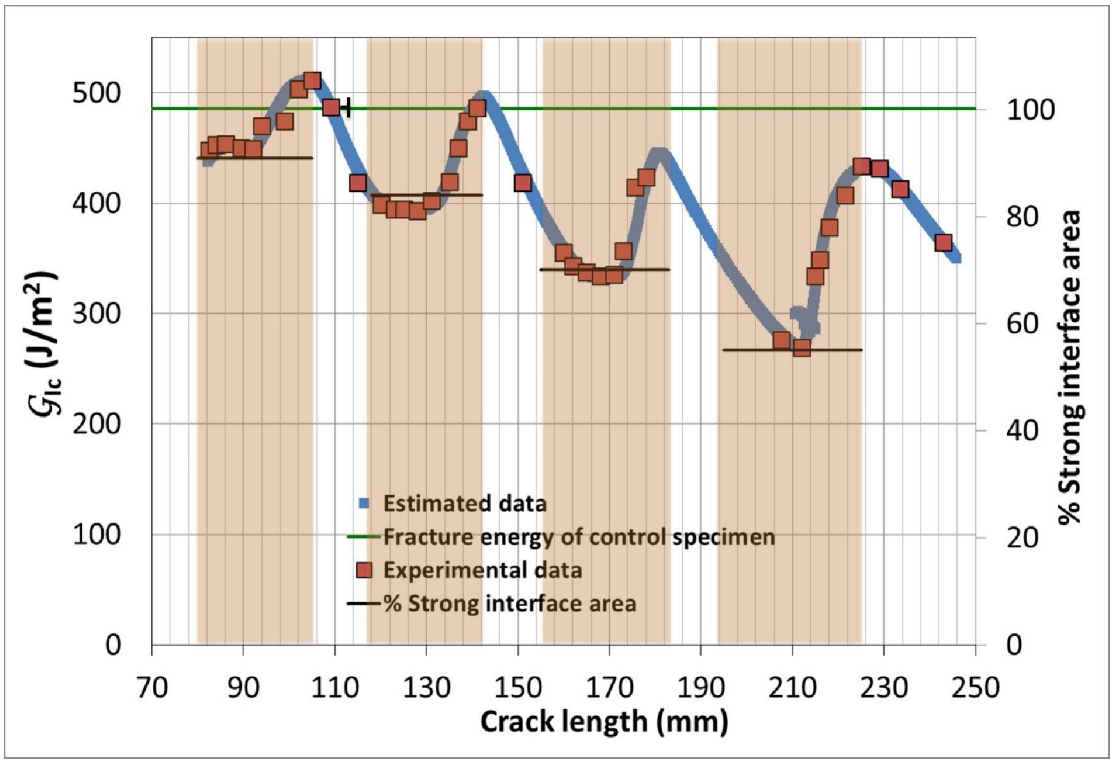

Figure 3-12: Mode I test results for specimen F

The plane stress plastic zone height in a bulk adhesive specimen can be estimated using equation 3.4. In Table 3-1 lists the average plane strain fracture toughness obtained from the SENB tests, results from compression tests, and average plane stress plastic zone height calculated using equation 3.4.

Table 3-1: SENB and compression test results

	Compressive modulus (GPa)	**Compressive yield strength [(a)] (MPa)**	**Tensile yield strength[(b)] (MPa)**	**K_{Ic} (MPa•m$^{0.5}$)**	**Plastic zone diameter[(c)] (mm)**
Average	2.45	37.77	28.33	1.16	0.51
Standard deviation	0.32	0.63	0.47	0.15	0.13

(a) Calculated using 1% offset

(b) Equal to 75% of the yield strength in compression [40]

(c) Calculated using equation (3.4)

From SENB tests, the plane stress plastic zone height for bulk adhesive specimens was around 0.51 mm, which is over twice that of the bondline thickness (0.2 mm) used in this study. Thus the onset of reverse R-curve type trends at 8 to 10 mm prior to weak interfaces might be due to longer plastic zone that develops ahead of the crack tip. In light of a longer plastic zone, the reverse R-curve type trends might be due to plastic zone dimensions ahead of the crack tip evolving towards smaller steady state dimensions as insufficient tractions at the weak interface start influencing the development of plastic zone.

For the specimen with the type C pattern and for the first pattern in the specimen of type E, it was observed that the presence of a control region prior to the weak interfaces led to unstable crack propagation. As mentioned earlier the unstable crack propagation was probably due to excess stored elastic energy available as the crack tip approaches a sufficiently weakened interface region. In order to test this hypothesis, a specimen of type G was prepared such that no long control regions separated the patterned regions. Pattern dimensions (d, s) were chosen such that fraction of weak interface area decreased as the growing crack entered the successive patterns. The pattern topology for specimen type G is shown schematically in Figure 3-2. In the specimen of type G the entire bonded area between the drilled holes up to the first pattern was coated with copper (100% coverage). Two patterns followed this fully coated area where separation between patterns was essentially the local weak interface separation distance (d) for the next pattern. Mode I test results for specimen of type G are shown in Figure 3-13. In the test region where the entire bonded area was covered with copper, the fracture energies were similar to that of specimen type B. In patterns following this region, it was observed that the fracture energy remained reasonably constant within a given pattern and that fracture energy increased with decreasing fraction of weak interfaces.

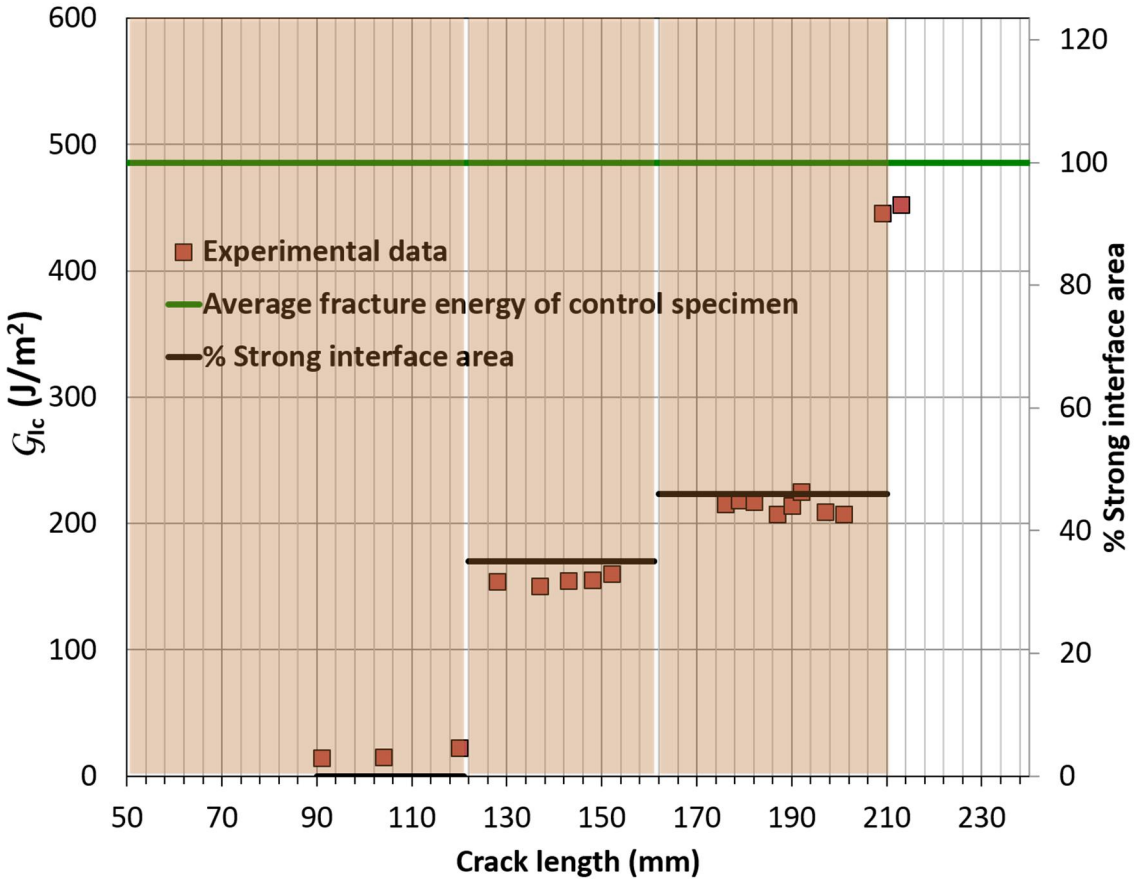

Figure 3-13: Mode I DCB test results for specimen G

Specimens of type D, E, F and G patterns contained several discrete localized weak interfaces along the length of the specimens. Along the width and the length of the specimens, the localized weak interfaces within a pattern were separated by good (control) interfaces. In specimen type H the localized weak interfaces were separated along the width of the specimens but they were continuous along the length of the specimens. Figure 3-2 schematically shows type H pattern topology and dimensions. It was observed that similar to failure modes shown schematically in Figure 3-5, copper deposited regions showed an apparent interfacial failure at copper/adherend interface, while regions without copper depositions showed cohesive failures within the adhesive layer. Mode I test results for the specimen of type H are shown in Figure 3-14, revealing similar R-curve type trends as observed in the case of specimen types D, E, F and G. Also the maximum in fracture energy within control regions correlated with the size of the control regions between successive patterns indicating that control regions being too

small for a fully developed R-curve.

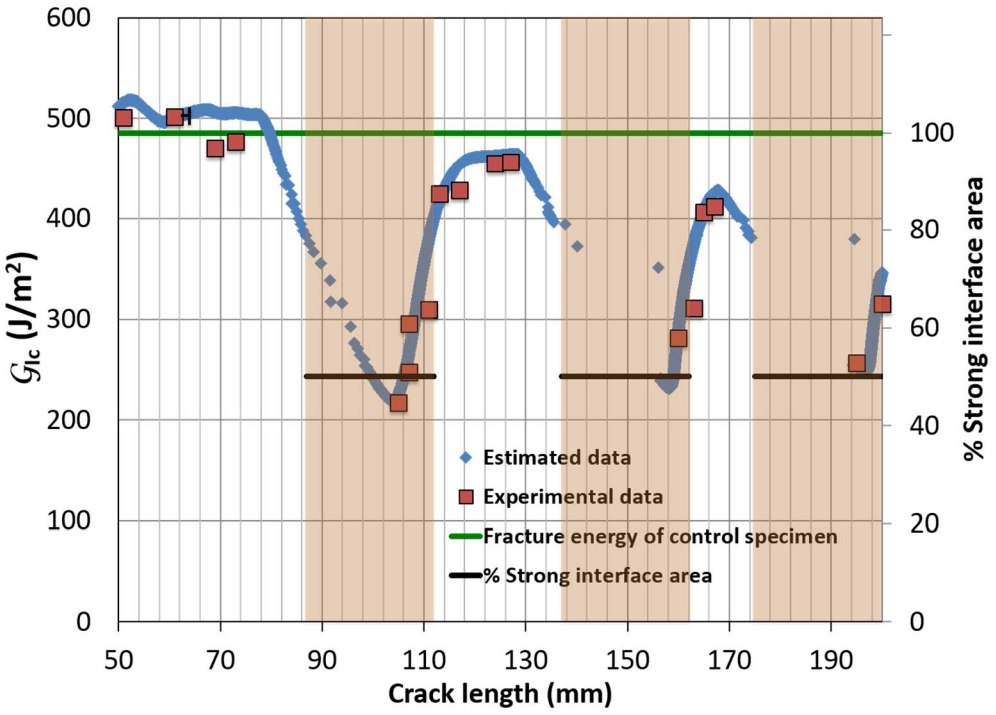

Figure 3-14: Mode I test results for specimen H

The figures above have hinted at a correlation between the measured fracture energies and the fraction of non-weakened bond area. Figure 3-15 compiles this information, showing minimum fracture energy values within patterned regions of specimen types D, E, F, G, H and fracture energies of control specimens (specimen type A, B) plotted against the area fraction of good interfaces within the pattern. The onset of reverse R-curve type trends at 8 to 10 mm prior to patterned regions indicate that the reduced tractions in patterned regions affect the fracture performance over such distances. For a crack tip in the pattern regions the local weak interfaces will be in the immediate vicinity of the crack tip thus significantly reducing the plastic deformation length scales though one must take into account the changes in stress state from plane strain to plane stress conditions. Also, in specimen types D, E, F, G, H the lengths of patterns were more than twice the distance between a pattern region and the onset of reverse R-curve type trends prior to a patterned region. Interestingly, it was observed that the measured fracture energy at the minimum within patterned weak interfaces of various densities with several sizes and separations were accurately modeled by a simple rule of mixtures:

$$G_{Total} = A_{Weeak} G_{weak} + A_{Strong} G_{Strong} \tag{3.5}$$

where G_{Total} is an effective fracture energy, G_{weak} is an interfacial fracture energy at the Cu/Al interface from Figure 3-6, G_{strong} is the cohesive fracture energy of the adhesive for the geometry used in this study, A_{weak} and A_{strong} are respectively the area fractions of weak interfaces and strong interfaces within a pattern determined using mask pattern dimensions.

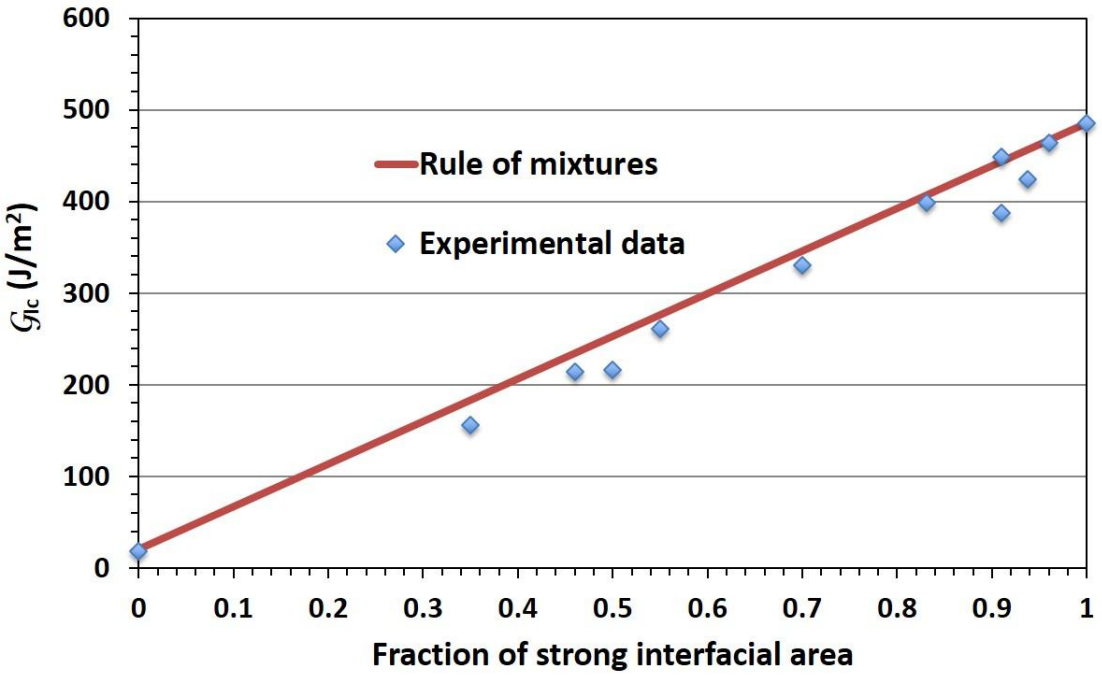

Figure 3-15: A minimum fracture energy within a patterned region as a function of area fraction of weak interface regions and the rule of mixtures according to equation 3.5

It is interesting to note that Figure 3-15 includes data from all the patterns used in this study. As shown in Figure 3-2, these patterns contained localized weak interfaces of several sizes and several separation distances. These results are very different than those observed for adhesive joints containing patterns of weak interfaces and are bonded with a soft adhesive [23]. During these tests higher or lower fracture energies than predicted by the rule of mixture type behavior were observed depending upon the shape of weak or strong discrete interfaces facing the crack tip. Chung et al. studied the behavior of adhesion and crack propagation in patterned adhesive films. The adhesive films consisted

of silicone elastomer patterned using longitudinal, lateral and crosswise incisions. Significant enhancement in fracture energy was observed for crosswise incisions, which was attributed to crack pinning mechanisms at the incisions [41]. However it must be noted that the modulus of adhesive used in the current study is orders of magnitude higher than the typical modulus range of a soft adhesive. In lap shear tests conducted on joints having stiff adherends bonded with a structural adhesive, it has been observed that the shape of the defects does not significantly affect the lap shear joint strength [12, 13]. In these tests the strength of the lap shear joint varied linearly with the function of defect area for joints of high modulus steel using a ductile adhesive indicating that yield and failure mechanisms over defect free regions act independent of the defect area and scale with a linear relationship with the bonded area. In our case rule of mixture type behavior in the patterned regions suggests similar behavior of yield mechanisms acting around the defects. Furthermore, an agreement with the rule of mixture type of behavior around weak interface suggests that the effect of a localized weak interface on the fracture energy of the adhesive is not dependent upon the presence of other local weak interface regions in the vicinity, at least for the length scales used within the patterns. Though, fracture energy does show reverse R-curve type trends over length scales corresponding to those of control regions between successive patterns indicating that at such large length scales the rule of mixtures type behavior might not apply but fracture energy would be a result of interplay of plasticity ahead of crack tip which in turn would be dependent upon the extent of available tractions at the weak interfaces in nearby regions.

3.3.2 Mixed mode test results

The locus of failure in an adhesive joint and resulting fracture energy are often reported to depend on the mode mixity applied [24]. Upon application of mixed mode conditions, the stress state ahead of crack tip often tends to drive the growing crack toward the adherend whose bonded surface is in tension. Thus by using mixed mode loading, cracks can be steered preferentially towards one adherend or other. As shown earlier in Figure 3-10, when the specimen of type D was tested in mode I conditions, R-curve type trends were observed around patterned regions with about a 20% drop in fracture energy within the patterned regions. Also the onset of reverse R-curve type trends was observed when the crack tip was within 8 to 10 mm distance from the

patterned regions. Figure 3-16 shows failure surfaces around patterned region of specimen of type D when tested in mixed mode conditions such that the adherend surface with weak interfaces was in axial tension. This leads to a stress state ahead of the crack tip that steers the crack towards the adherend containing the weak interface patterns (ψ = +60°).

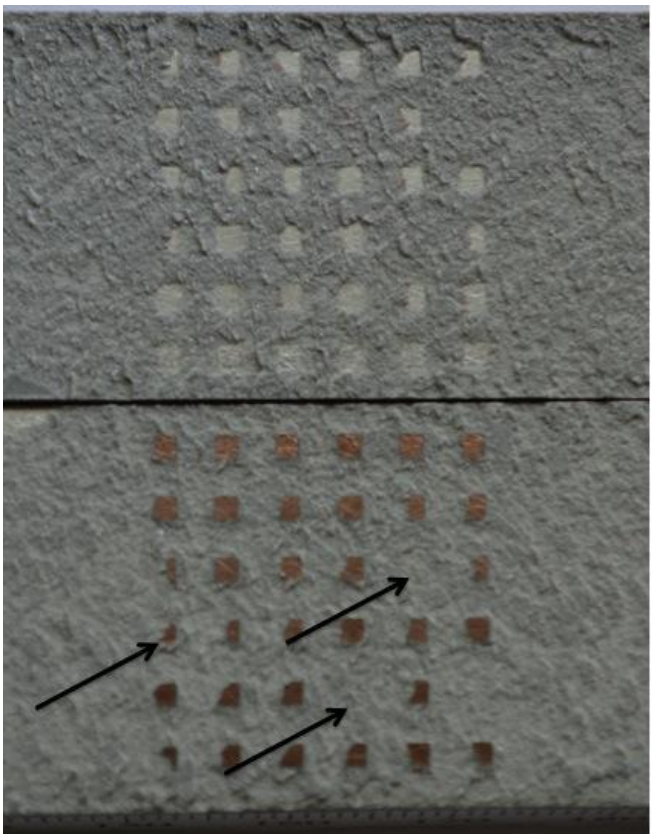

Figure 3-16: Failure surfaces of specimen D when tested in mixed mode (ψ = +60°) conditions

From Figure 3-16, it is observed that, unlike the failure modes observed for mode I conditions, several weak interface regions within a pattern were not detected by the propagating crack. Also, many local weak interfaces were only partially detected, with a cohesive failure in the adhesive layer over a portion of these weak interface regions. Mixed mode DCB test results for specimen of type D are shown Figure 3-17.

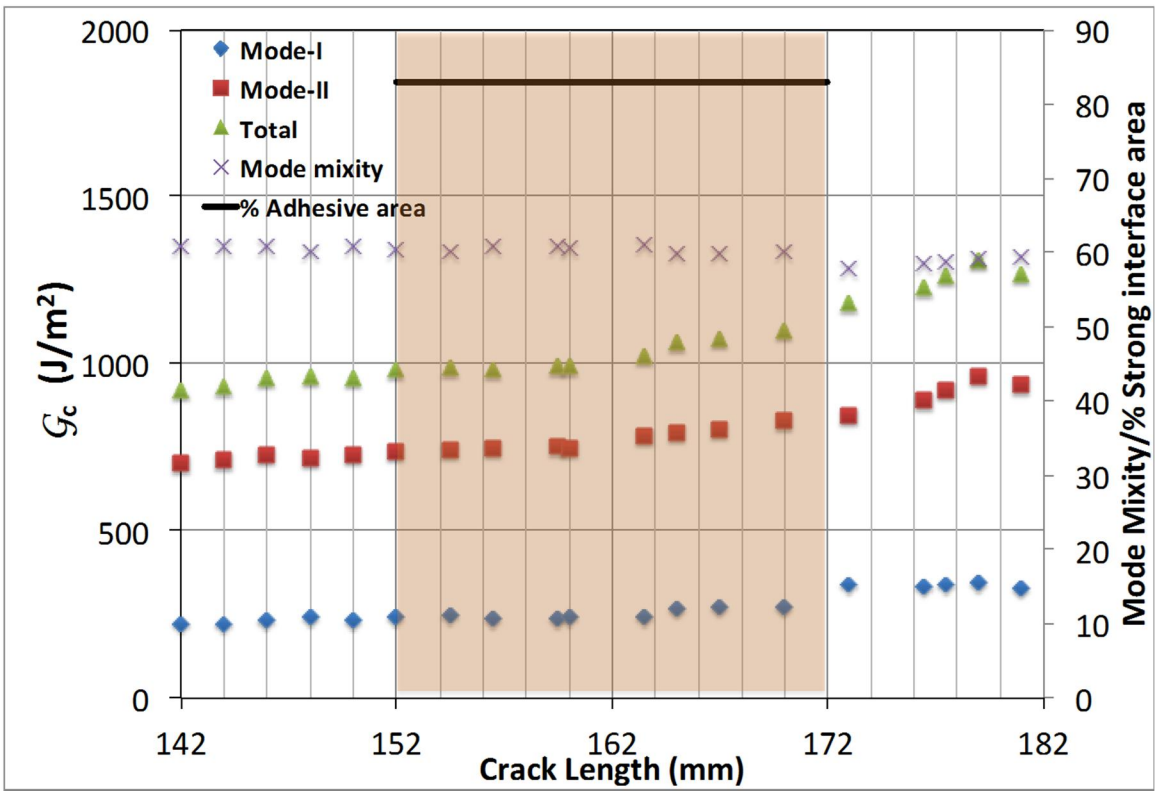

Figure 3-17: Mixed mode (ψ = +60°) test results for specimen D

Interestingly, when a specimen of type D was tested under mixed mode conditions no R-curve type trends were observed around patterned region. Mode I test data around the identical pattern is shown in Figure 3-10. It was observed that the fracture energy remained reasonably constant as the crack tip approached and entered a patterned region. Thus the same weak interface pattern when tested in mixed mode conditions did not show a significant effect on the fracture energy compared to the approximately 20% drop in fracture energy in the patterned region when loaded in mode I. It has been observed that interfacial fracture toughness is strongly dependent upon the mode mixity angle [42]. In light of such reports, higher interfacial resistance might provide sufficient interfacial tractions needed for the plasticity ahead of the crack to develop leading to absence of R-curve type trends in mixed mode I conditions.

Figure 3-18 shows failure surfaces of identically patterned DCB specimens tested in mode I and under mixed mode conditions (ψ = -60°) such that the adherend surface with defects was in axial compression resulting in a stress state ahead of crack tip which drives the crack away from the weak interfaces.

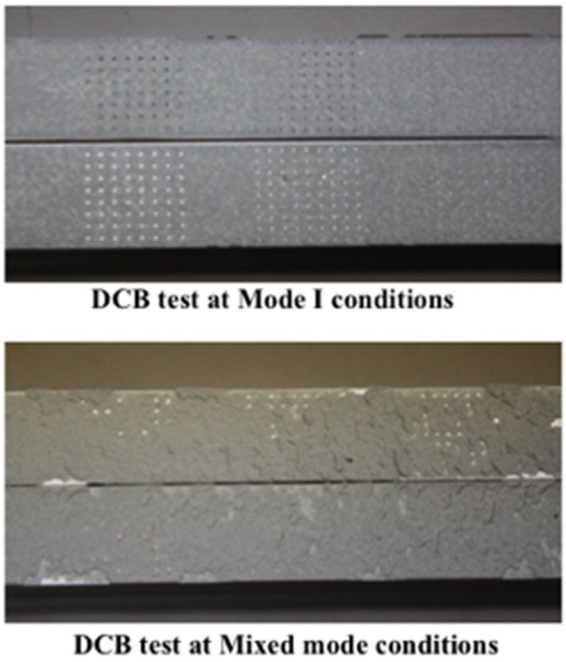

Figure 3-18: Failure surface of identically patterned DCB specimens tested in mode I and in mixed mode conditions (ψ = -60°)

It was observed that almost all the weak interfaces in patterns were detected by the crack tip in mode I conditions, while in mixed mode conditions (ψ = -60°) very few local weak interfaces were detected by the growing crack, resulting in predominantly cohesive failures within the adhesive layer, even in the presence of very weak local interfaces in the patterned regions, confirming the possibility of diverting failures away from small but very weak interfaces. It should be noted that above results are based on a single set of pattern dimensions (s, d) and for the geometry and materials used in this study. Nevertheless, these are interesting outcomes when considered in terms of potential applications such as controlled disassembly of the adhesive joints. For example, although based on preliminary and limited results, patterned bonds indicate towards the possibilities to tune the mode I fracture energy without significantly affecting mixed mode fracture behavior. Though it should be noted that under infield applications, factors such as environmental conditions or other loading conditions such as fatigue etc. that might exist simultaneously or independently might lead to changes in the trends observed in this study.

3.4 Conclusions

A technique is reported for creating well-defined and quantifiable localized weak interfaces on base-acid treated aluminum adherends using physical vapor deposition of copper. By using this technique to create several systematic patterns, the effect of the presence of localized interface defects on the performance of structural epoxy adhesive bonds was studied. Under mode I loading conditions, the presence of localized weak interfaces influenced the fracture energy of a propagating debond over a considerable distance both before and following a local pattern of weakened interfaces. Furthermore, the mode I fracture energy scaled with the area fraction of weak interfaces, according to the simple rule of mixtures. For the adhesive system and joint geometry used in this study, it was observed that under mixed mode loading such that the bonding surface with defects is in tension, crack tip detects most of the defects but does not show a significant effect on the fracture energy. In contrast, a crack could be made to avoid exceptionally weak interfaces, when loaded under mixed mode conditions such that bonding surface with defects is in axial compression. This possibility combined with an ability to tune fracture energies in mode I conditions, may offer joint design options to allow a joint to either tolerate or be more susceptible to interfacial defects, offering the ability to tailor joint performance for performance, designed failure modes, or easier disassembly.

3.5 References

[1] B. Chen and D. A. Dillard, "The Effect of the T-Stress on Crack Path Selection in Adhesively Bonded Joints," *International Journal of Adhesion and Adhesives,* **21**, 357-368, 2001.

[2] B. Chen, D. A. Dillard, J. G. Dillard, and R. L. Clark Jr, "Crack Path Selection in Adhesively Bonded Joints: The Roles of External Loads and Specimen Geometry," *International Journal of Fracture,* **114**, 167-190, 2002.

[3] B. Chen, D. A. Dillard, J. G. Dillard, and R. L. Clark, "Crack Path Selection in Adhesively-Bonded Joints: The Role of Material Properties," *The Journal of Adhesion,* **75**, 405-434, 2001.

[4] H. R. Daghyani, L. Ye, and Y. W. Mai, "Effect of Thermal Residual Stress on the Crack Path in Adhesively Bonded Joints," *Journal of Materials Science,* **31**, 2523-2529, 1996.

[5] N. A. Fleck, J. W. Hutchinson, and S. Zhigang, "Crack Path Selection in a Brittle Adhesive Layer," *International Journal of Solids and Structures,* **27**, 1683-1703, 1991.

[6] E. P. Chan, D. Ahn, and A. J. Crosby, "Adhesion of Patterned Reactive Interfaces," *The Journal of Adhesion,* **83**, 473-489, 2007.

[7] G. Bresson, J. Jumel, M. E. R. Shanahan, and P. Serin, "Statistical Aspects of the Mechanical Behaviour a Paste Adhesive," *International Journal of Adhesion and Adhesives,* **40**, 70-79, 2013.
[8] M. Budzik, J. Jumel, K. Imielińska, and M. E. R. Shanahan, "Fracture in Composite/Aluminium Joints of Variable Adhesive Properties," *The Journal of Adhesion,* **85**, 736-754, 2009.
[9] M. Budzik, J. Jumel, and M. R. Shanahan, "Experimental Investigation of Mesoscale Crack Front Triple Line," *Applied Physics A,* **114**, 495-501, 2014.
[10] M. K. Budzik, J. Jumel, and M. E. R. Shanahan, "Adhesive Fracture of Heterogeneous Interfaces," *Philosophical Magazine,* **93**, 2413-2427, 2013.
[11] M. K. Budzik, J. Jumel, and M. E. R. Shanahan, "Antagonist Adhesion Effects due to Variable Substrate Surface," *Soft Matter,* **8**, 8321-8326, 2012.
[12] E. F. Karachalios, R. D. Adams, and L. F. M. da Silva, "Strength of Single Lap Joints with Artificial Defects," *International Journal of Adhesion and Adhesives,* **45**, 69-76, 2013.
[13] H. Schonhorn, F. W. Ryan, and T. T. Wang, "Effects of Symmetrical Bonding Defects on Tensile Shear Strength of Lap Joints Having Ductile Adhesives," *Journal of Applied Polymer Science,* **15**, 1069-1078, 1971.
[14] T. T. Wang, F. W. Ryan, and H. Schonhorn, "Effect of Bonding Defects on Shear Strength in Tension of Lap Joints Having Brittle Adhesives," *Journal of Applied Polymer Science,* **16**, 1901-1909, 1972.
[15] N. G. Berry and J. R. M. d'Almeida, "The Influence of Circular Centered Defects on the Performance of Carbon–Epoxy Single Lap Joints," *Polymer Testing,* **21**, 373-379, 2002.
[16] H. Kan and M. Ratwani, "Stress Analysis of Stepped-Lap Joints with Bondline Flaws," *Journal of Aircraft,* **20**, 848-852, 1983.
[17] J. N. Rossettos, P. Lin, and H. Nayeb-Hashemi, "Comparison of the Effects of Debonds and Voids in Adhesive Joints," *Journal of Engineering Materials and Technology,* **116**, 533-538, 1994.
[18] J. N. Rossettos and E. Zang, "On the Peak Shear Stresses in Adhesive Joints With Voids," *Journal of Applied Mechanics,* **60**, 559-560, 1993.
[19] M. Olia and J. N. Rossettos, "Analysis of Adhesively Bonded Joints with Gaps Subjected to Bending," *International Journal of Solids and Structures,* **33**, 2681-2693, 1996.
[20] T. P. Lang and P. K. Mallick, "The Effect of Recessing on The Stresses in Adhesively Bonded Single-Lap Joints," *International Journal of Adhesion and Adhesives,* **19**, 257-271, 1999.
[21] A. Chadegani and R. C. Batra, "Analysis of Adhesive-Bonded Single-Lap Joint with an Interfacial Crack and a Void," *International Journal of Adhesion and Adhesives,* **31**, 455-465, 2011.
[22] R. B. Heslehurst, "Observations in the Structural Response of Adhesive Bondline Defects," *International Journal of Adhesion and Adhesives,* **19**, 133-154, 1999.
[23] E. P.-N. Chan, "Adhesion of Patterned Polymer Interfaces," 3289211 Ph.D., University of Massachusetts Amherst, Massachusetts, United States 2007.
[24] E. Nicoli, "Characterization of Mixed-Mode Fracture Testing of Adhesively Bonded Wood Specimens," Virginia Polytechnic Institute and State University,

2010.
[25] E. Nicoli and D. Dillard, "Procedures for Mixed Mode Fracture Testing of Bonded Beams in a Dual Actuator Load Frame," in *Time Dependent Constitutive Behavior and Fracture/Failure Processes, Volume 3*, T. Proulx, Ed., ed: Springer New York, 2011, pp. 25-31.
[26] B. R. K. Blackman, H. Hadavinia, A. J. Kinloch, M. Paraschi, and J. G. Williams, "The Calculation of Adhesive Fracture Energies in Mode I: Revisiting the Tapered Double Cantilever Beam (TDCB) Test," *Engineering Fracture Mechanics,* **70**, 233-248, 2003.
[27] B. R. K. Blackman, A. J. Kinloch, M. Paraschi, and W. S. Teo, "Measuring the Mode I Adhesive Fracture Energy, Gic, of Structural Adhesive Joints: The Results of an International Round-Robin," *International Journal of Adhesion and Adhesives,* **23**, 293-305, 2003.
[28] ISO, "Adhesives — Determination of The Mode I Adhesive Fracture Energy of Structural Adhesive Joints Using Double Cantilever Beam and Tapered Double Cantilever Beam Specimens," vol. 25217, ed. Switzerland: ISO 2009.
[29] A. J. Kinloch and S. J. Shaw, "The Fracture Resistance of a Toughened Epoxy Adhesive," *The Journal of Adhesion,* **12**, 59-77, 1981.
[30] D. Broek, *Elementary Engineering Fracture Mechanics*. Alphen aan den Rijn: Sijthoff & Noordhoff, 1978.
[31] A. Ameli, M. Papini, J. A. Schroeder, and J. K. Spelt, "Fracture R-Curve Characterization of Toughened Epoxy Adhesives," *Engineering Fracture Mechanics,* **77**, 521-534, 2010.
[32] M. a. Arias, P. Frontini, and R. Williams, "Analysis of the Aamage Zone Around the Crack Tip for Two Rubber-Modified Epoxy Matrices Exhibiting Different Toughenability," *Polymer,* **44**, 1537-1546, 2003.
[33] M. Papini, G. Fernlund, and J. Spelt, "Effect of Crack-Growth Mechanism on the Prediction of Fracture Load of Adhesive Joints," *Composites Science and Technology,* **52**, 561-570, 1994.
[34] A. Sheppard, D. Kelly, and L. Tong, "A Damage Zone Model for the Failure Analysis of Adhesively Bonded Joints," *International Journal of Adhesion and Adhesives,* **18**, 385-400, 1998.
[35] S. S. Wang, J. F. Mandell, and F. J. McGarry, "An Analysis of the Crack Tip Stress Field in DCB Adhesive Fracture Specimens," *International Journal of Fracture,* **14**, 39-58, 1978.
[36] T. Ikeda, A. Yamashita, D. Lee, and N. Miyazaki, "Failure of a Ductile Adhesive Layer Constrained by Hard Adherends," *Journal of Engineering Materials and Technology,* **122**, 80-85, 2000.
[37] D. L. Hunston, A. J. Kinloch, and S. S. Wang, "Micromechanics of Fracture in Structural Adhesive Bonds," *The Journal of Adhesion,* **28**, 103-114, 1989.
[38] P. Martiny, F. Lani, A. J. Kinloch, and T. Pardoen, "A Maximum Stress at a Distance Criterion for the Prediction of Crack Propagation in Adhesively-Bonded Joints," *Engineering Fracture Mechanics,* **97**, 105-135, 2013.
[39] P. Martiny, F. Lani, A. J. Kinloch, and T. Pardoen, "A Multiscale Parametric Study of Mode I Fracture in Metal-to-Metal Low-Toughness Adhesive Joints," *International Journal of Fracture,* **173**, 105-133, 2012.

[40] A. J. Kinloch, *Adhesion and Adhesives: Science and Technology*. London; New York: Chapman and Hall, 1987.
[41] J. Y. Chung and M. K. Chaudhury, "Roles of Discontinuities in Bio-Inspired Adhesive Pads," *Journal of The Royal Society Interface,* **2**, 55-61, 2005.
[42] V. Tvergaard and J. W. Hutchinson, "The influence of plasticity on mixed mode interface toughness," *Journal of the Mechanics and Physics of Solids,* **41**, 1119-1135, 6// 1993.

4 Developing Characterization Procedures to Assess Adhesion Fundamentals for Chewing Gum Cud

4.1 Introduction

Chewing gum is a highly popular confectionary with annual global sales in the region of USD 26 billion [1]. A freshly chewed gum cud is a soft, compliant and tacky material. These properties allow spreading of gum cuds when discarded on concrete or other surfaces. With sufficiently long times and with the aid of vehicular or foot traffic a fresh gum cud can penetrate into porous surfaces. Once attached or embedded on a surface, loss of water content and other plasticizers leads to reduced mobility, essentially hardening the gum cud in place. Once hardened, a discarded gum cud is difficult to remove via mechanical scraping, power washing or other processes , thus resulting in measurable clean-up costs to municipalities [2-4].

A typical chewing gum formulation consists of a gum base combined with sweetening and flavoring agents. Additional functional agents such as fats, waxes, gum base compatible resins, fillers, emulsifiers, softening agents, antioxidants, etc. are added to enhance the sensory experience and storage life. Fats and waxes acting as softening agents enhance flow characteristics of the gum while gum base compatible resins are sometimes added to enhance chew bulkiness [2, 3, 5]. Interestingly, some gum base compatible resins used in gum formulations (e.g. rosins) are also used as tackifiers in pressure sensitive adhesive (PSA) formulations to enhance tackiness of the adhesive [6]. Above glass transition temperature, tackifiers act as swelling agents or in a sense diluents in the entanglement network, thus essentially lowering the rubbery plateau modulus and thus improving the flow properties of the PSA [7]. Apart from flow characteristics, the adhesion performance of soft materials or PSAs is also dependent upon the surface chemistry of the substrates with which they interact [8]. Once attached to a surface, the debonding behavior of PSAs is dependent upon their energy dissipation behavior and nonlinear properties of PSAs, e.g. strain hardening behavior [7, 9]. Unlike PSAs, which do not harden or cure over time, discarded chewing gum cuds, upon loss of moisture harden, similar to adhesives such as rubber cement [10]. Thus chewing gum cuds, once

discarded and upon contact with the surface, show a combination of adhesion promoting properties of PSAs and solvent borne adhesive systems.

The probe tack test is a widely used test method to study the effect of rheological and surface parameters on adhesion performance of soft materials and PSA [7, 9, 11-14]. In a probe tack test, an axisymmetric probe is typically brought into contact with a film of material or an adhesive at a given rate until a desired load is reached. After a given contact time the probe is pulled away from the material at a constant rate and the tensile load is measured as a function of the probe displacement. Sometimes a reverse configuration is used, where an adhesive to be tested is adhered to the probe and then the probe covered with the adhesive is brought into contact with the substrates of interest. Thus using probe tack test, adhesion performance of an adhesive can be studied as a function of adhesive rheological properties, surface chemistry, and surface topology of the substrates [11, 12, 14].

Although the probe tack test is a common method to characterize PSA performance, characterizing the adhesion of gum cuds involves several challenges. The first challenge lies in developing a consistent chewing method that can hydrate gum in a manner than mimics the expected loss of gum ingredients (sugar, flavoring agents, etc.) that would occur in a typical oral chewing process. Secondly, a freshly chewed gum is a dynamic material whose surface chemistry and constitutive properties change as a function of loss of water. Thirdly, in order for results to be relevant to gum adhesion characterization and removal methods, the failures are desired at the gum cud/test substrate interface or within the gum cud (Figure 4-1). Thus challenge lies in avoiding failures at the interfaces that are not of interest e.g. gum cud/adherend interface (Figure 4-1). Sometimes failures can occur within the gum cud as well.

In the current study a probe tack test based approach was developed to address the above-mentioned challenges and to quantify adhesion performance of gum cuds as a function of gum cud rheology and substrate surface parameters. Using this approach the adhesion performance of four chewing gum formulations was studied using substrates with well-defined surface chemistry and surface topology. The debond load-displacement

traces obtained using the probe test approach on a series of gum cud-substrate combinations were successfully obtained, thus providing insights into the effect of parameters such as substrate roughness, substrate surface energy, and gum cud rheology on the adhesion performance of gum cuds. An approximate relationship was proposed to correlate the effects of these parameters with the gum cud adhesion performance. It is envisioned that this approach could be helpful towards quantifying gum cud adhesion, which could be helpful in developing chewing gum formulations, which when chewed and improperly discarded, facilitate easier removal from adhering surfaces during the cleanup process.

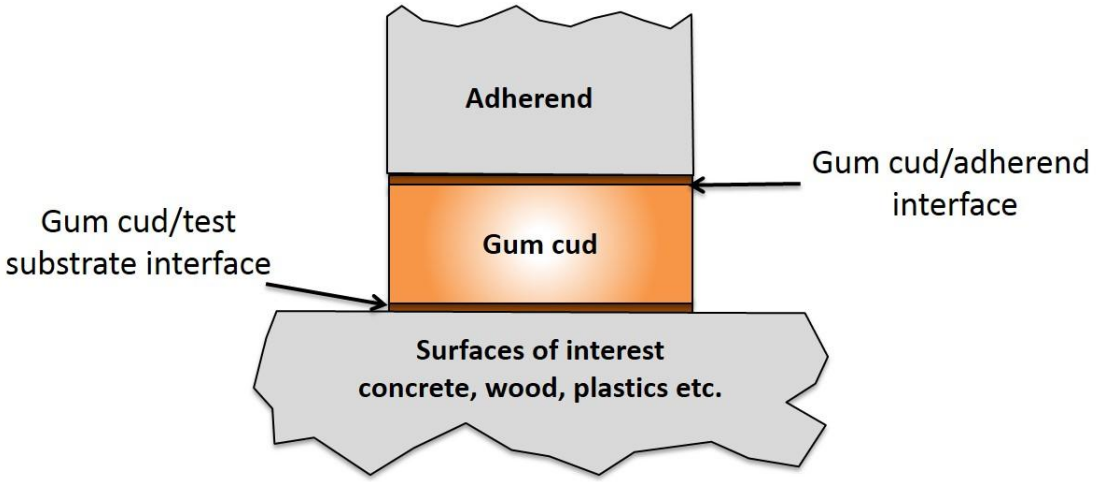

Figure 4-1: Schematic representation of test components involved during characterization of gum cud adhesion. Failures are desired at gum cud/test substrate interface or within the gum cud.

4.2 Experimental

4.2.1 Materials

Four gums A1, B1, A2 and B2 were considered during this study. Gums were formulated, prepared and supplied by sponsors in sealed containers. Although the specific formulations of the materials are not conveyed, A2 and B2 gums have similar composition as A1 and B1 formulations, respectively, except for the quantity of flavoring agent. The quantity of flavoring agent in formulations ending in 2 was lower than those ending in 1. The differences between the formulations are highlighted in next sections through rheological characterizations, which will be discussed in later sections. Amongst the above-mentioned formulations, A1 is reportedly a commercially available formulation.

Four types of Pyrex glass based test substrates with known surface roughness and surface energies were used during the study. Prior to their use, all as-received stationary substrates were thoroughly cleaned using reverse osmosis (RO) water and isopropyl alcohol (IPA). The substrates were then dried using compressed house nitrogen gas followed by drying in a convection oven at 105°C for 1 hour. For each test in this study, a cleaned, freshly prepared and unused test substrate was used. The first type of substrate ("Glass") consisted of smooth, transparent Pyrex glass pieces (McMaster Carr®, Atlanta, GA, USA, Catalog No: 8476K12) having dimensions 50.8 mm x 50.8 mm x 6.35 mm (length x width x thickness). For the second type of substrates ("Glass-GS"), the same Pyrex glass pieces as in substrates Glass were used but whose surface was coated with a commercially available Gum Stopper (GS) solution (4Earth Solutions, Sunderland, UK). The GS solution is reportedly a low viscosity water based system, which is used as a barrier coating to reduce gum adhesion. The GS solution coating was applied using Kimwipe® (Kimberly Clark® Corporation, Neenah, WI, USA) paper soaked in the GS solution and for all the tests. As per manufacturer instructions, the GS coated substrates were dried under ambient conditions for 4 hours. The third type of substrate ("Frit") consisted of sintered fine porosity Pyrex glass frits (R&H Glass Filters Inc. Georgetown, DE, USA, Catalog No: RH-1000-F, fine porosity, 55 mm diameter, 6.12 mm thickness)

having a higher surface roughness compared to Glass and Glass-GS substrates. For the fourth type of substrate ("Frit-GS"), the same glass frits were used but with surface coated with the GS solution, applied using the same technique as that used for the Glass-GS substrates. Due to porous nature of frits, gum stopper solution permeated through the frit. The application of GS solution was continued till the entire frit surface appeared evenly wet. The GS coated frits were then dried for at least 4 hours before use in the probe tests.

Substrate surface chemistry:

Collaborators from Professor Alan Esker's lab (Department of Chemistry, Virginia Tech, Blacksburg, VA, USA) carried out substrate surface chemistry analysis and contact angle measurements. Contact angle measurements were performed using an FTA 200 Contact Angle Analyzer (First Ten Angstroms, Portsmouth, VA) using a sessile drop technique. The surfaces of interest were placed on an adjustable platform and approximately 5 μL of solvent were placed on the surface using a syringe. These solvents included Milli-Q water (Millipore Gradient A10, Esker Laboratories, Virginia Tech), glycerol (HPLC Grade, Alfa Aesar), formamide (99%, Fisher Scientific), and diiodomethane (99%, Aldrich). For the contact angle analysis, a single frame movie was taken using a video CCD camera. The contact angle was measured by fitting a mathematical expression to the shape of the drop, and then calculating the slope of the tangent to the drop at the liquid-solid-vapor interface (FTA Operator's and Installation Manuals, revision 2.0, May 30, 1997). Four replicates were performed for the calculation of the average contact angle. Thermodynamic work of adhesion between gum cuds and substrates were estimated using an approach based on Fowkes' equation, Young's equation, Dupre's equation, and contact angle measurements on gum cuds and test substrates. Details of this approach are mentioned in Appendix E.

Substrate surface roughness:

Surface roughness profiles of the Pyrex glass pieces (used in Glass and Glass-GS substrates) and glass frits (used in Frit and Frit-GS substrates) were characterized using a Dektak stylus profilometer, "DektakXT" (Bruker Corporation, Billerica, MA, USA),

equipped with a 12.5-micron diameter tip. Figure 4-2 shows a comparison of typical surface roughness profiles of smooth Pyrex glass pieces and sintered glass frits. As expected, the roughness of the Pyrex glass pieces was significantly lower than the roughness of the Pyrex glass frits. Based on the roughness data, the Pyrex glass pieces had a relatively negligible root mean square roughness (Z_{rms}) (about 0.001 microns) while Z_{rms} of the Pyrex glass frits was on an average of 21.09 microns (Standard deviation, S = 0.94 microns). Application of GS solution on glass frits (GS-Frit substrates) showed a negligible effect on the roughness of the frits.

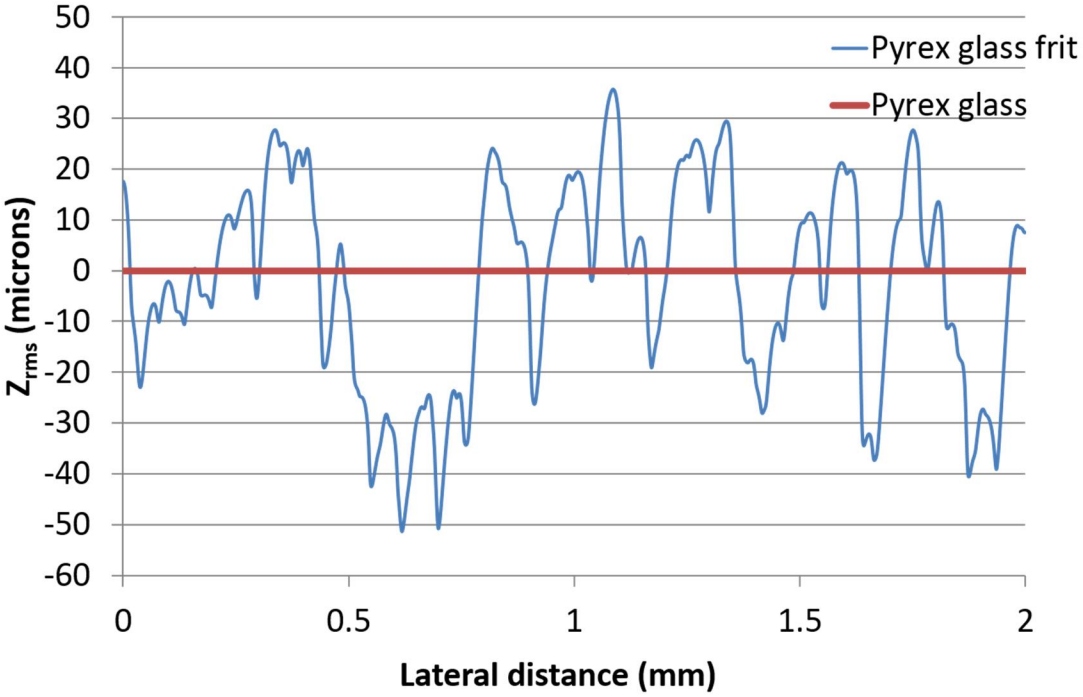

Figure 4-2: Typical roughness profile of the bonding surface of the Pyrex glass piece (used in Glass and Glass-GS substrates) and Pyrex glass frits (used in Frit and Frit-GS substrates)

4.2.2 Probe Tests

4.2.2.1 Test Setup

Figure 4-3 schematically shows the test setup used for the probe tests. The probe test setup consists of a steel probe to which gum cud test samples are bonded, a stationary test substrate, and a clamping fixture and mirror assembly that permits visual observation of debonding from transparent substrates. The steel probe was connected to the movable

crosshead of an Instron 5500R tensile testing machine. The stationary substrates (discussed in the next section) were mounted on a mirror assembly via a clamping fixture as shown in Figure 4-3 and Figure 4-4. The clamping fixture facilitated the convenient mounting of a fresh stationary substrate for each probe test. The mirror assembly consisted of a front surface mirror mounted at a 45° angle with respect to the test axis and surface of the stationary substrate. The mirror assembly was equipped with three fine threaded leveling screws for alignment purposes. Figure 4-4 shows a photograph of the probe test setup.

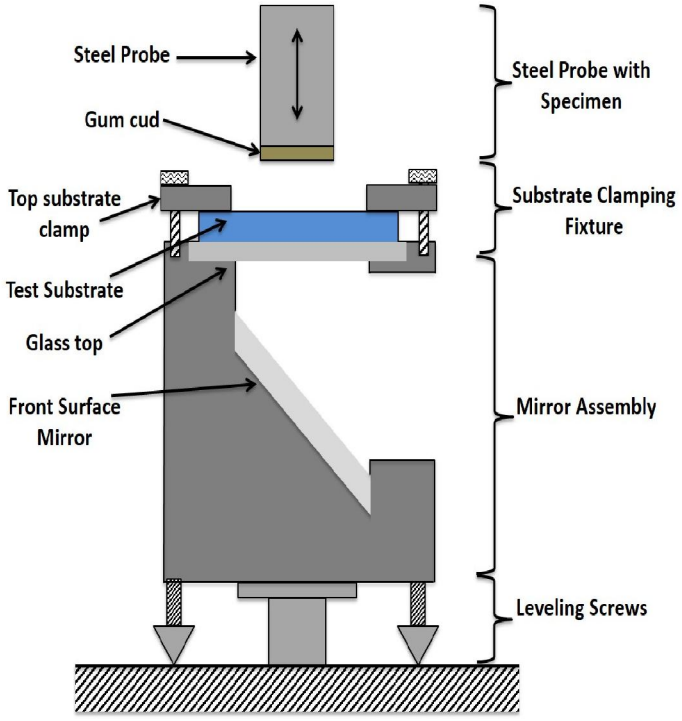

Figure 4-3: Schematic representation of a cross-section of the probe test setup

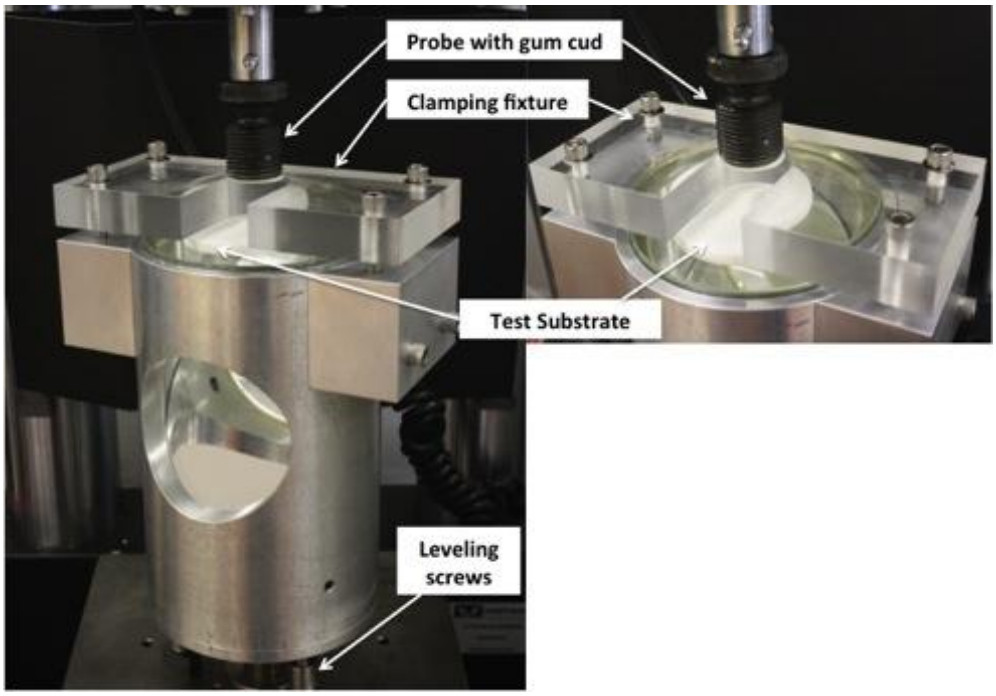

Figure 4-4: Probe test setup

4.2.2.2 Gum cud preparation

A recirculating water bath was set at 30 ºC. This temperature was checked periodically with a thermometer to ensure the bath temperature stayed within 30 ± 1 ºC. The total mass of the gum sample was weighed to the nearest 0.001 g and recorded. A beaker was filled with deionized water to have 100 mL H_2O/1 g gum sample. This beaker was placed into the water bath until the temperature had equilibrated. The gum pellets were then placed into the beaker for 15 minutes. During this time, the calendaring machine (My Perfect Kitchen Pasta Machine, Bed Bath and Beyond, SKU # 13748136) was wiped clean using acetone and Kimwipes. The calendaring machine consisted of two manually rotated counter-rotating steel cylinders separated by an adjustable nip gap. The entire machine was then rinsed with deionized water. Once the gum sample had finished the initial 15-minute soak, it was removed from the beaker. Samples from this step were either combined and processed as one large sample for surface chemical analysis, or processed piecewise for mechanical testing. The gum sample was rolled once through the largest nip distance (2.5 mm) of the calendaring machine and briefly returned to the beaker of warm water to keep the sample near 30 ± 1ºC. The calendaring machine was then set to a 1.6 mm nip gap and the gum sample was rolled through again and the

sample was then temporarily returned to the beaker of warm water equilibrated at 30 ± 1ºC. The calendaring machine was then set to the smallest nip setting (0.6 mm) and the sample was rolled through the machine 10 times. In between each roll, the sample was dipped in the warm deionized water beaker at 30 ± 1ºC, and folded in half to ensure the sample would continue to fit the nip width of the rollers. After the final roll, the sample was placed on a 4" x 6" piece of poly-vinyl coated fiberglass mesh, and the mesh and gum sample were placed into a beaker containing fresh deionized water at 30± 1ºC. After every 1.5 hours the sample was placed into a fresh beaker of 30 ± 1 ºC deionized water for a total post-rolling soak time of 4.5 hours. After this soaking schedule was complete, gum cuds were removed from the water bath and were passed through the smallest nip gap setting of the calendaring machine in order to obtain gum cud sheets with a consistent thickness. The 100 mL H_2O/ 1 g sample ratio was maintained throughout the procedure. Based on extensional viscosity tests conducted by the sponsors, the gum cuds chewed using above procedure showed extensional viscosities within the similar range as of a typical mouth chewed gum cud.

Rolled gum cud sheets were then conditioned in an oven maintained at 30 °C and at about 50% relative humidity (RH) for 24 hours. The humidity in the oven was maintained using a humidity controller (LF-HS, Gas Humidifications Systems, Fuel Cell Technologies Inc., Albuquerque, NM, USA). Disks of 22.8 mm diameter (same as the steel probe) were then punched from the conditioned gum cud sheets. Punched gum cud discs were then placed back in the oven at 50% RH at 30 °C. Once the punching process was complete gum cuds were used for probe tests within 45 min.

4.2.2.3 Steel Probe Bonded with a Gum Cud

Prior to each probe test, a fresh gum cud disc was bonded to the movable steel probe using a very thin layer of cyanoacrylate (Elmer's Super Glue, Columbus, OH, USA) (Without this step, failures often occurred at the steel probe interface, but the adhesive bonded well enough to the hydrated gum cuds that this undesirable failure mode was eliminated.). This forced the failure modes during the debonding stage of a probe test to either a cohesive failure within gum cud or a failure at the test substrate/gum cud interface. During preliminary tests, it was observed that gum cud specimens spread out

beyond the probe contact area during the bonding stage of the tests, thus increasing the effective bonded area. As this increase in the area is dependent upon the rheological response of the specimens for a given test geometry, it was suspected that this increase in the area could affect the debonding response across specimens having a dissimilar rheological response. In order to minimize this effect, prior to each probe test, the specimen bonded on the steel probe was masked using a wax paper sheet having a centrally located circular hole of 15.8 mm diameter within the probe contact area. Thus, the bonding area was restricted to the mask hole, ensuring a constant bond area during each test. Though the contact area was controlled using wax paper, it's not possible to maintain a constant gum cud thickness during the probe tests. For probe tests, it has been observed that the degree of confinement represented by the ratio of radius of the contact area to the thickness of the adhesive film, when plotted on log scale, could affect the failure locus observed during the probe tests (Figure 4-5) [15]. Based on rheological characterizations of all the gum cuds (discussed in later sections), it is expected that the changes in the gum cud thickness across gum cud formulations would be minor when plotted on log scale.

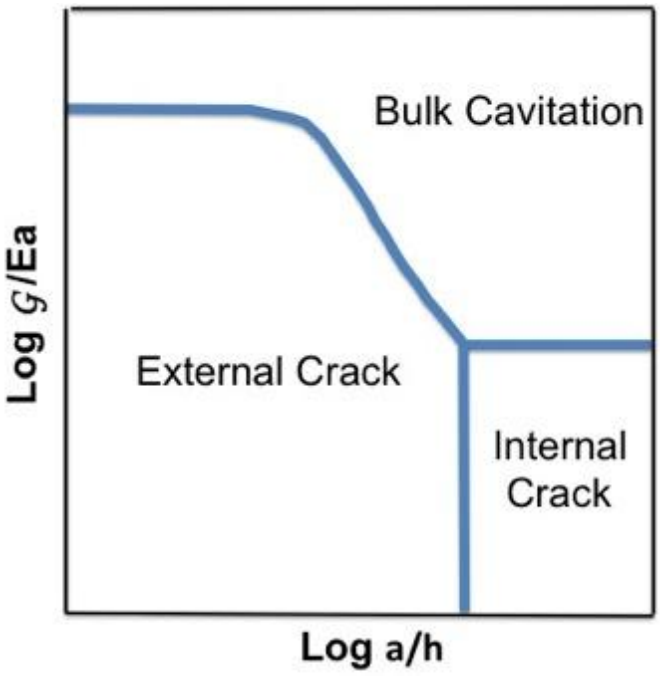

Figure 4-5: Schematic representation of failure locus observed in probe test as a function of geometry and material properties [15]

4.2.2.4 Probe Test Procedure

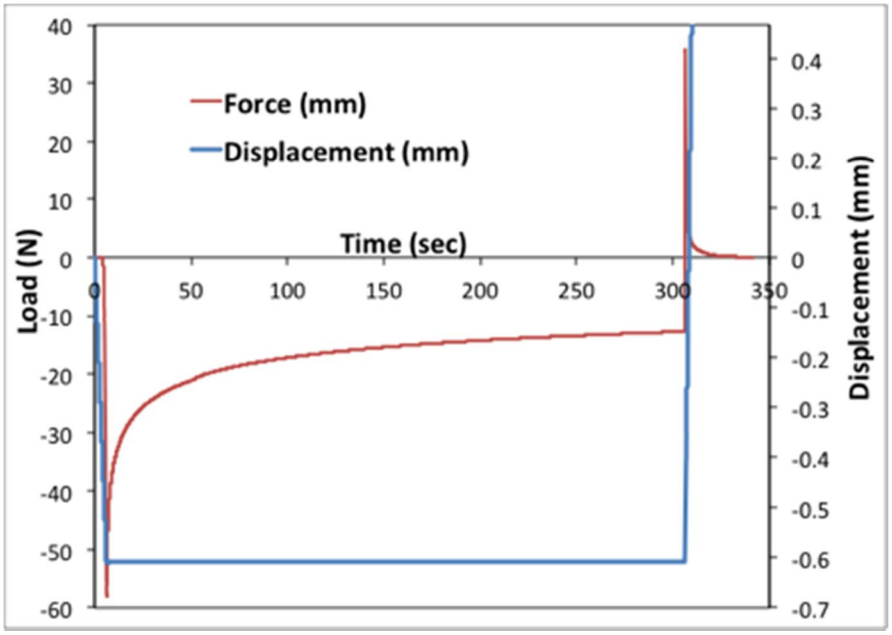

Figure 4-6: Probe test profile

Figure 4-6 shows the test profile used during probe tests. All probe tests were carried out in displacement control mode. A gum cud bonded steel probe was brought into contact with a stationary substrate at 0.1 mm/s until the load cell detected a load corresponding to a desired stress (300 kPa nominal, as measured over the net area of wax paper hole). At this point, the probe was kept at a fixed displacement for a desired dwell time (300 s). Following the dwell time, the probe was pulled away at the rate of 0.3 mm/s. During the test, the debonding force and displacements were recorded at regular time intervals. Three replicate tests were carried out for each gum cud-test substrate combination.

4.2.3 Rheological Characterization of Gum Cuds

Rheological characterizations were conducted by the sponsors in their lab facility. Gum cuds, prepared as described in section 2.2.2, were used for rheological characterizations and were shipped to the sponsor's facility. To limit moisture loss during shipping, conditioned gum cuds were sealed using aluminum foil and PSA tapes prior to shipping to the sponsor's facility. Rheology characterizations were carried out using a TA

Instruments ARGIII Discovery series rheometer within 48 hours from the sealing of specimens. Linear viscoelastic properties of gum cuds were characterized using frequency-sweep tests (100 rad/sec to 0.1 rad/sec) at 25 °C in a parallel plate geometry. For each type of gum cud, five replicates were tested and the average values were reported along with standard deviations.

4.3 Results and Discussion

4.3.1 Gum cud rheology

Figure 4-7 shows a comparison of storage and loss moduli of all four types of gum cuds. As seen in Figure 4-7, A1 gum cuds had higher storage and loss moduli compared to B1 type gum cuds. As mentioned earlier, A2 and B2 had similar compositions as A1 and B1 type gum cuds, respectively, except that the former had less flavoring agent content. It was observed that reducing the flavor content did not affect the storage and loss modulus values significantly. As shown in Figure 4-8, reducing the flavor content led to changes in average tan δ values. It was observed that reducing the flavor content in A gum cuds led to a decrease in tan δ values at frequencies less than 2 rad/sec while B type gum cuds showed an overall increase in tan δ values for frequencies less than 30 rad/sec. From Figure 4-8 it can be observed that at frequencies less than about 2 rad/sec, A1 shows higher tan δ values compared to B1 type gum cuds while both gum cuds show similar tan δ values at frequencies greater than about 2 rad/sec.

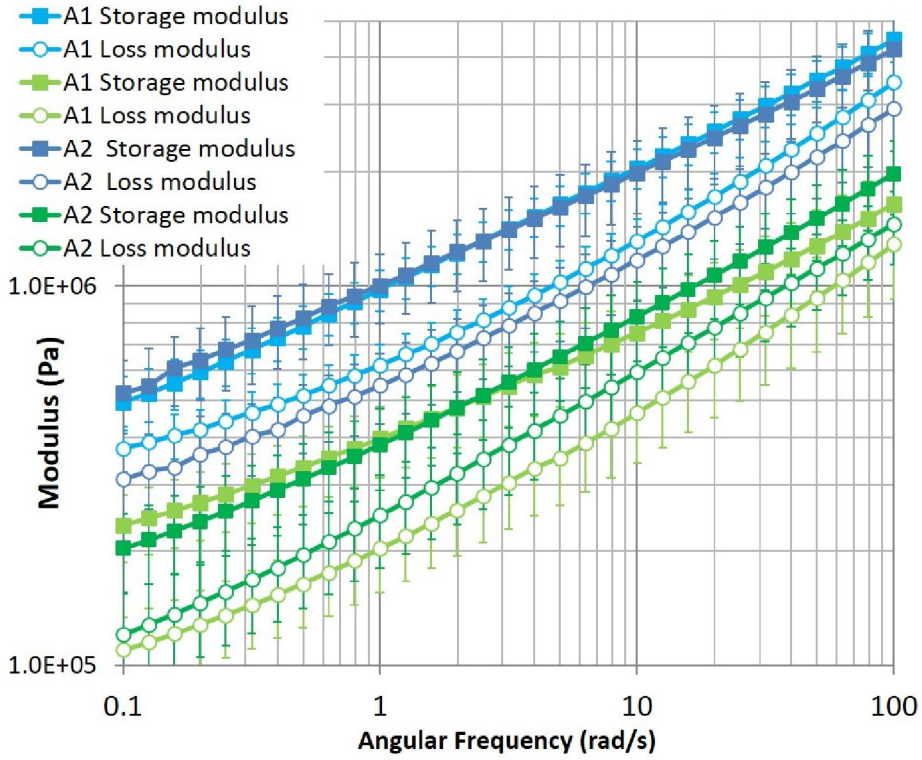

Figure 4-7: Storage and loss modulus as a function of frequency at 25 °C

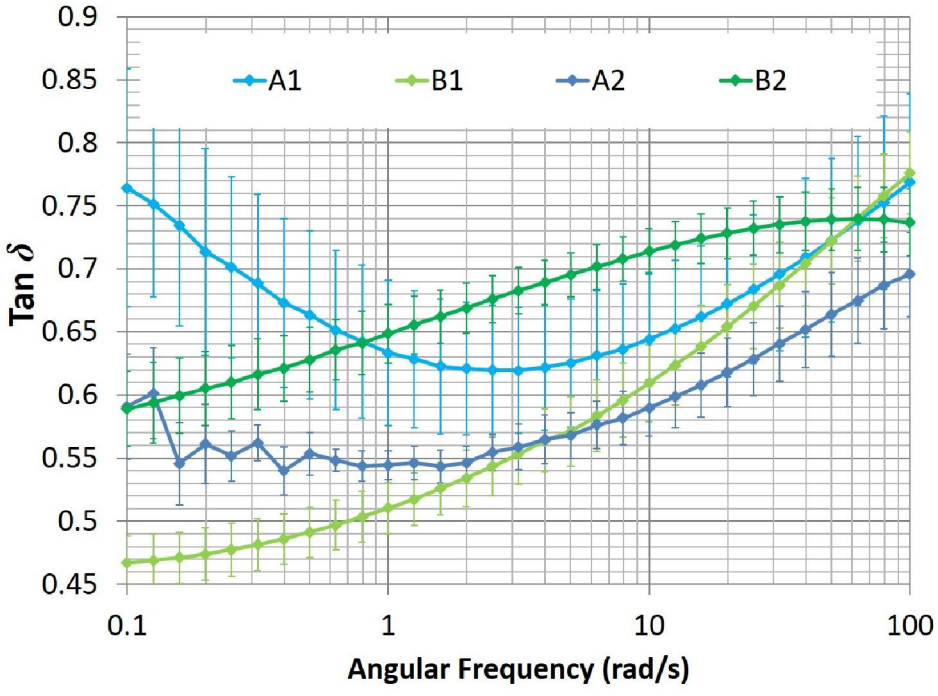

Figure 4-8: Tan δ as a function of frequency at 25 °C

Rheological data reported here represent a spectrum, which shows rheological properties for a range of frequencies or time-scales at 25 °C. In order to put measured rheological properties into perspective for interpreting probe tests results, it is important to identify relevant time-scales during probe tests that correspond with the appropriate frequencies in the rheological spectrum. The rheological characterization was performed in the linear viscoelastic regime via sinusoidal displacement input while the probe tests followed a displacement input as shown in Figure 4-6. Due to different displacement inputs in both the tests, only a rough estimate of the relevant timescale can be made. As shown in Figure 4-9, bonding timescales during probe tests were determined by approximating probe test displacement input as a sinusoidal input whose period is twice the sum of time it takes for the probe to compress the gum cud (region AB), the dwell time (region BC) and the time involved during the debonding of the gum cud (region CD). In all the probe tests it took rapproximately six seconds for the probe to compress the gum cud (region AB), till a 300 kPa stress was detected. The dwell time was 300 sec (region BC) and the unloading time was roughly about two seconds (region CD).

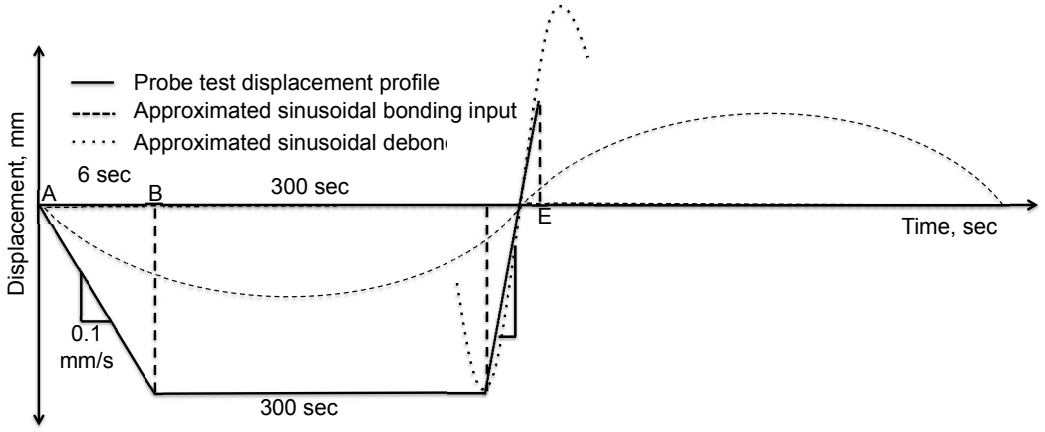

Figure 4-9: Approximating the displacement profile of probe tests with a sinusoidal input to estimate relevant bonding and debonding timescales

Thus the total time was about 308 seconds, which corresponds to a period of 616 sec for an approximated sinusoidal input and the corresponding angular frequency of 0.01. The smallest angular frequency used during the rheological characterizations was 0.1. Hence tan δ values at an angular frequency of 0.1 are used to study the effect of tan δ on gum adhesion. Nevertheless these tan δ values might be different if the trends change

between 0.1 and 0.01 angular frequencies. Table 4-1 summarizes tan δ, storage and loss modulus of all the gum cuds at the angular frequency of 0.1 rad/sec and at 25 °C.

Table 4-1: Rheological properties of all the gum cuds at the angular frequency of 0.1 at 25 °C

Gum Type	Storage Modulus, MPa	Loss Modulus, MPa	Tan δ
A1	0.49	0.37	0.76
A2	0.52	0.30	0.59
B1	0.23	0.10	0.46
B2	0.20	0.12	0.58

Similarly, as shown in Figure 4-9, the debonding displacement input (region CE) of probe tests can be approximated as sinusoidal input and debonding time scales for the probe tests can be roughly estimated. Point E represents the time at which complete debonding has occurred (Figure 4-6). This point was different during each test depending upon the time at which complete separation of gum cud was observed during the probe tests. Table 4-2 lists rheological properties corresponding to the debonding timescales for all gum cud-substrate combinations at 25°C.

Table 4-2: Rheological properties at approximate debonding timescales at 25 °C

Gum type-test substrate	Angular frequency, (rad/sec)	Loss modulus, (MPa)	Storage modulus, (MPa)	Tan δ
A1-Frit	0.19	0.38	0.58	0.66
A1-Frit-GS	0.22	0.40	0.60	0.67
A1-Glass	0.16	0.36	0.55	0.66
A1-Glass-GS	0.16	0.36	0.55	0.66
A2-Frit	9.72	1.21	1.97	0.61
A2-Frit-GS	12.15	1.30	2.11	0.62
A2-Glass	1.94	0.71	1.22	0.59
A2-Glass-GS	9.72	1.21	1.97	0.61
B1-Frit	0.81	0.20	0.38	0.52
B1-Frit-GS	0.81	0.20	0.38	0.52
B1-Glass	1.30	0.23	0.43	0.54
B1-Glass-GS	1.94	0.27	0.49	0.55
B2-Frit	3.24	0.39	0.58	0.68
B2-Frit-GS	1.62	0.30	0.46	0.66
B2-Glass	1.39	0.29	0.44	0.66
B2-Glass-GS	2.43	0.35	0.53	0.67

4.3.2 Probe Test Results

Qualitative discussion

Figure 4-10 shows representative failure modes observed during probe tests with A1 and B1 gum cuds on Glass substrates.

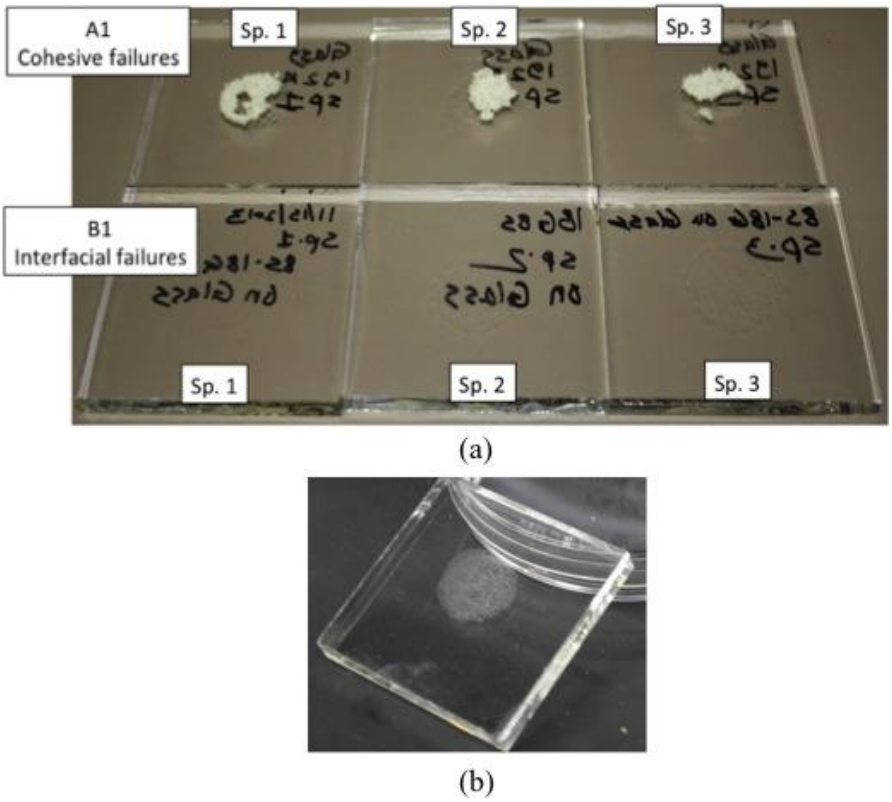

Figure 4-10: (a) Failure modes for probe test with B1 and A1 gum cuds on Glass substrates, (b) Close up of exudate left on the test substrates by B1 gum cuds when tested on Glass substrates.

It was observed that A1 gum cuds showed predominantly cohesive failures while B1 gum cud specimens showed apparent interfacial failures at the gum cud/test substrate interface. Based on visual observations both A1 and B1 gum cuds showed similar failure modes across all the substrates used in this study. Upon visual observations of failure surfaces on Glass and Glass-GS substrates, it was noted that B1 specimens left behind a thick viscous liquid exudate during the failure (Figure 4-10 (b)), this residue did not appear to be part of a bulk gum cud specimen but rather a leached out viscous liquid residue. In case of B1 specimens tested on Glass and Glass-GS substrates the failures were observed within this exudate layer. Here onwards this failure mode is mentioned as an apparent interfacial failure mode. Figure 4-11 and Figure 4-12 show comparisons of force vs. displacement curves for A1 and B1 gum cuds on Glass and Glass-GS substrates, respectively. Upon Glass and Glass-GS substrates, A1 gum cuds showed a distinct shoulder region following the peak in debonding force. Such shoulder regions were not observed for B1 specimens when tested on Glass and Glass-GS substrates. For probe tack

tests with soft materials on a smooth surface, it has been reported that an occurrence of a first peak in the debond force vs. displacement curves of probe tests is related to nucleation of cavities in either the bulk of the specimen or at the interface, while the region following the peak force is related to mechanisms such as cavity growth followed by fibrillation [7, 13-16]. As the extent of energy dissipation due to mechanisms such as cavity growth and fibrillation decreases, the shoulder region becomes less pronounced. In this case the occurrence of a pronounced shoulder following the peak in debonding force vs. displacement curves for A1 gum cuds suggests such mechanisms and is visually confirmed by observation of failure surfaces where extensive fibrillation and cavitation was clearly seen for the A1 gum cuds. For B1 specimens, an apparent interfacial failure was observed and failure surfaces did not show any signs of fibrillation upon observation with the naked eyes. It is important to note that the above observations are based on the appearance of the failure surfaces after the tests and, in the case of B1 gum cuds, possible occurrence of these mechanisms during the tests cannot be ruled out. Nevertheless, based on the distinctive shoulder regions in load vs. displacement curves for A1 gum cuds and their absence for B1 gum cuds, coupled with visual observations of failure surfaces, energy dissipation mechanisms such as fibrillations appear less extensive for B1 gum cuds than for A1 gum cuds. During the debonding stage of the probe tests, if cavities originating at the interface are able to grow along the interface and coalesce e.g. during tests on low adhesion surface coupled with a low viscoelastic dissipative material, an interfacial failure is expected. If a highly dissipative material is in contact with a good adhesion surface, cavity growth rate is higher in vertical direction with cavities culminating in the formation of fibrils as the probe is pulled away[7, 15]. In light of such reports and upon observation of failure modes, it appears that B1 might have less resistance to cavity growth along the interfacial exudate layer resulting in lower effective interfacial adhesion to the Glass and Glass-GS substrates compared to A1 specimens. Also it was observed that B1 test substrates showed a viscous residue left behind on the substrate. It would be interesting to study the role of this residue in terms of its effect on the adhesion of gum cud to the substrate.

Figure 4-13 and Figure 4-14 show force vs. displacement curves for B1 and A1 specimens when tested on Frit and Frit-GS substrates. As shown in Figure 4-2, Frit and

Frit-GS substrates had considerably higher surface roughness than Glass and Glass-GS substrates. Interestingly, when tested on these two types of substrates, A1 gum cuds did not show a pronounced shoulder region compared to those observed on Glass and Glass-GS substrates, indicating a significant reduction in energy dissipating mechanisms such as fibrillation when tested on a rough surface. This will be discussed in more detail in the quantitative analysis of the probe test results provided in next few sections.

As mentioned earlier, A2 and B2 gum cuds had similar compositions as their counterparts except that 2-type gum cuds had reduced flavor content. From Figure 4-7 it can be seen that these gum cuds had similar storage and loss moduli across the entire frequency range, while A2 gum cuds had lower tan δ values below 2 rad/sec. During probe tests, A2 specimens showed an apparent interfacial failure while as mentioned earlier A1 specimens showed a cohesive failure, with post failure observations of A1 gum cud failure surfaces showing signs of extensive fibrillation and cavitation. Figure 4-15 and Figure 4-16 show comparisons of force vs. displacement curves for A1 and A2 gum cuds on Glass and Glass-GS substrates. It can be observed that A1 gum cuds showed a distinct shoulder region while shoulder region was absent for A2 specimens. Force vs. displacement curve for B2 gum cuds and their comparisons with B1 gum cuds are included in Appendix A. Qualitatively both B1 and B2 gum cuds showed similar force vs. displacement trends with an absence of pronounced shoulder regions.

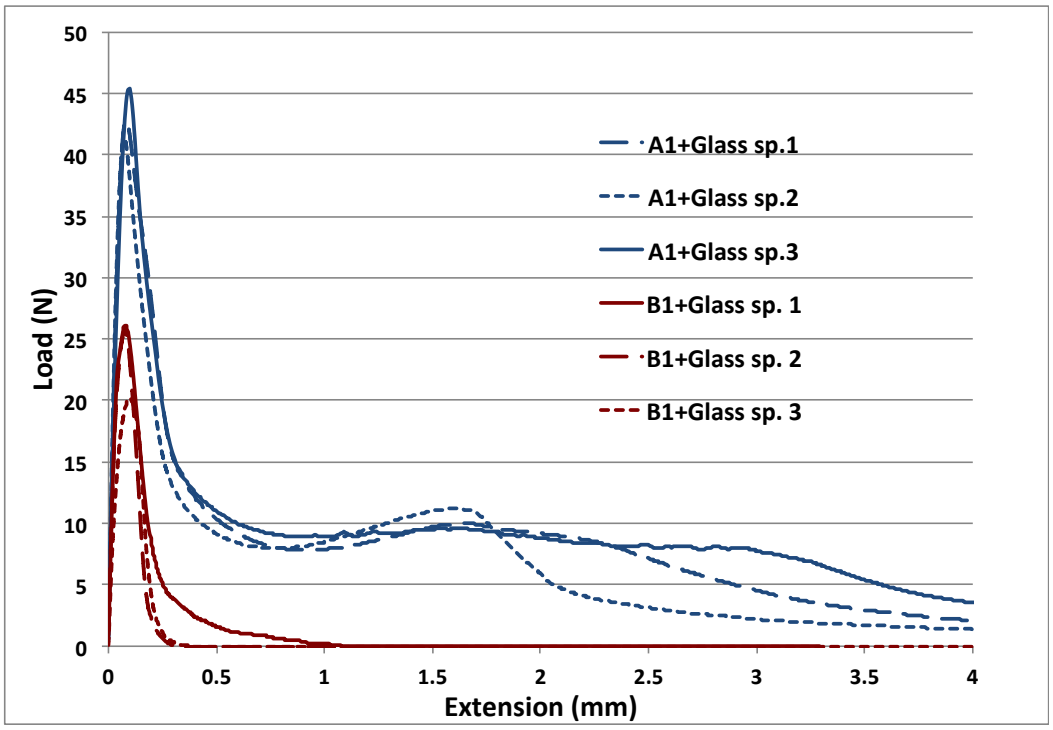

Figure 4-11: Force vs. displacement curves for probe tests on B1 and A1 gum cuds on Glass substrates

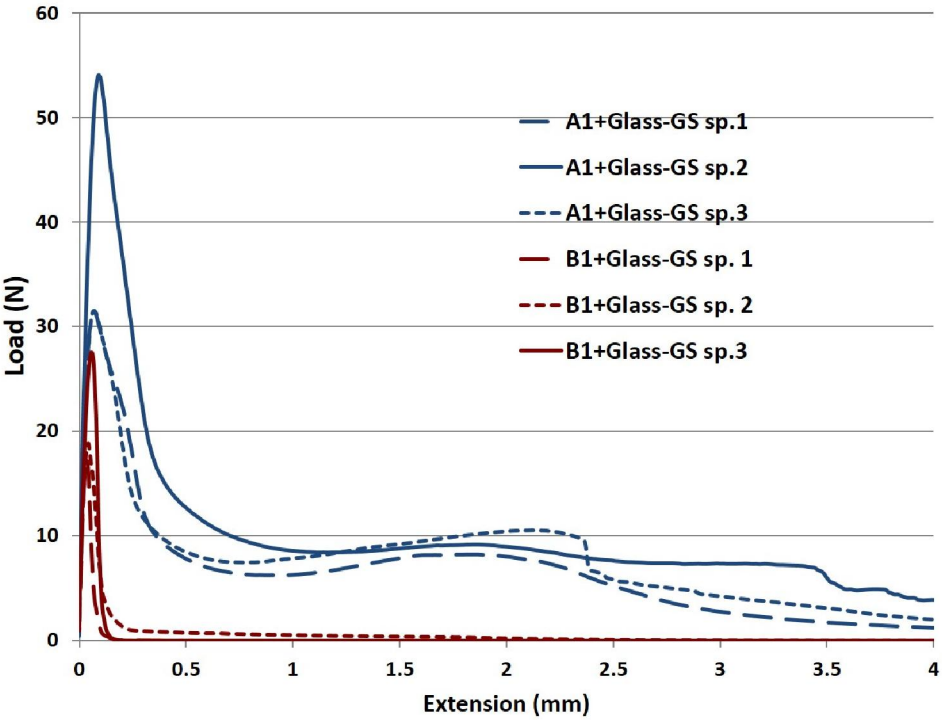

Figure 4-12: Force vs. displacement curves for probe tests on B1 and A1 gum cuds on Glass-GS substrates

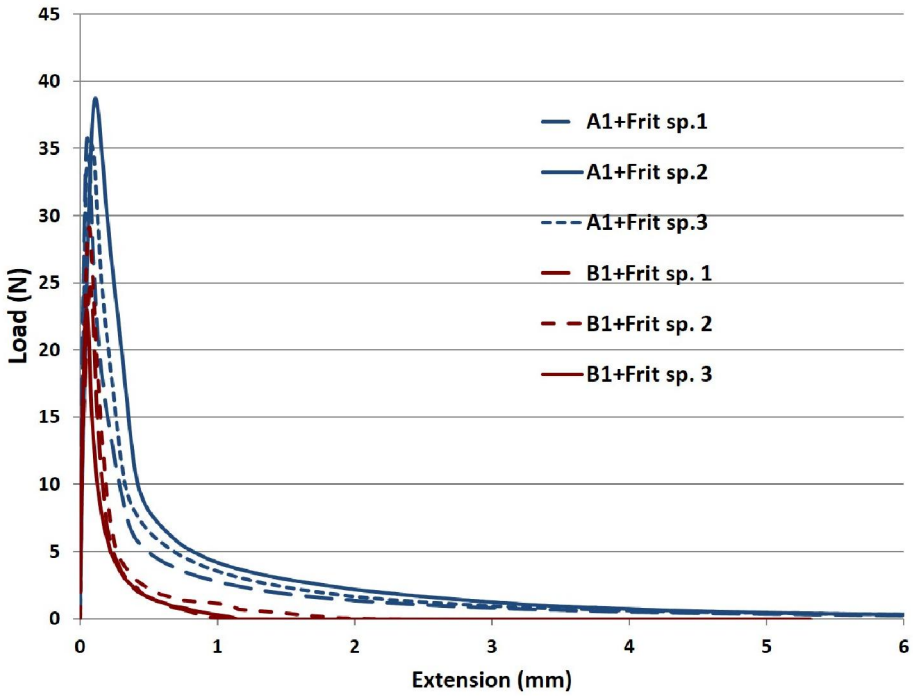

Figure 4-13: Force vs. displacement curves for probe tests on B1 and A1 gum cuds on Frit substrates

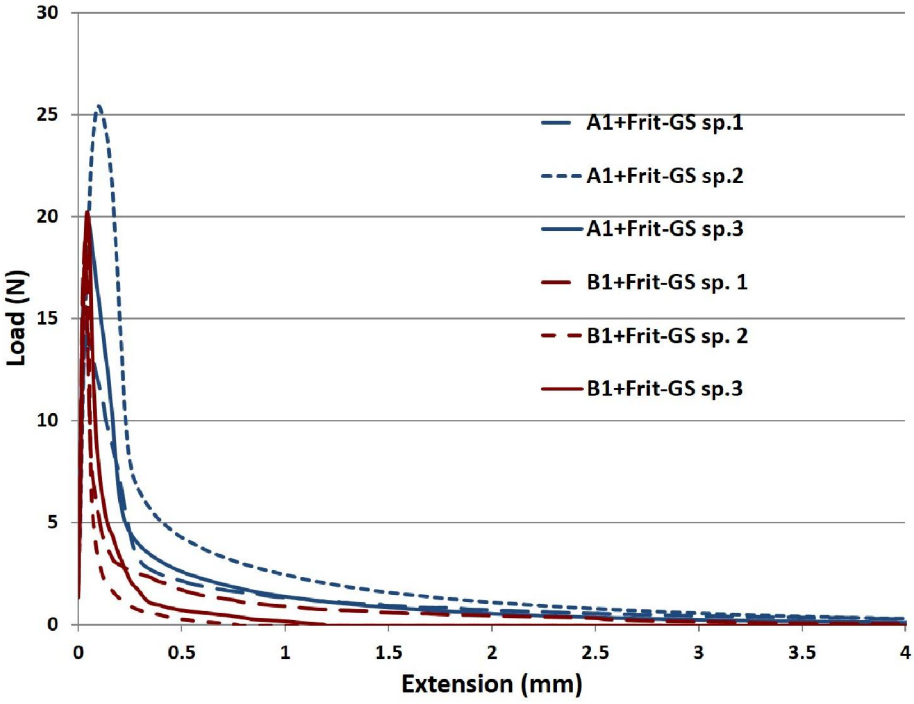

Figure 4-14: Force vs. displacement curves for probe tests on B1 and A1 gum cuds on Frit-GS substrates

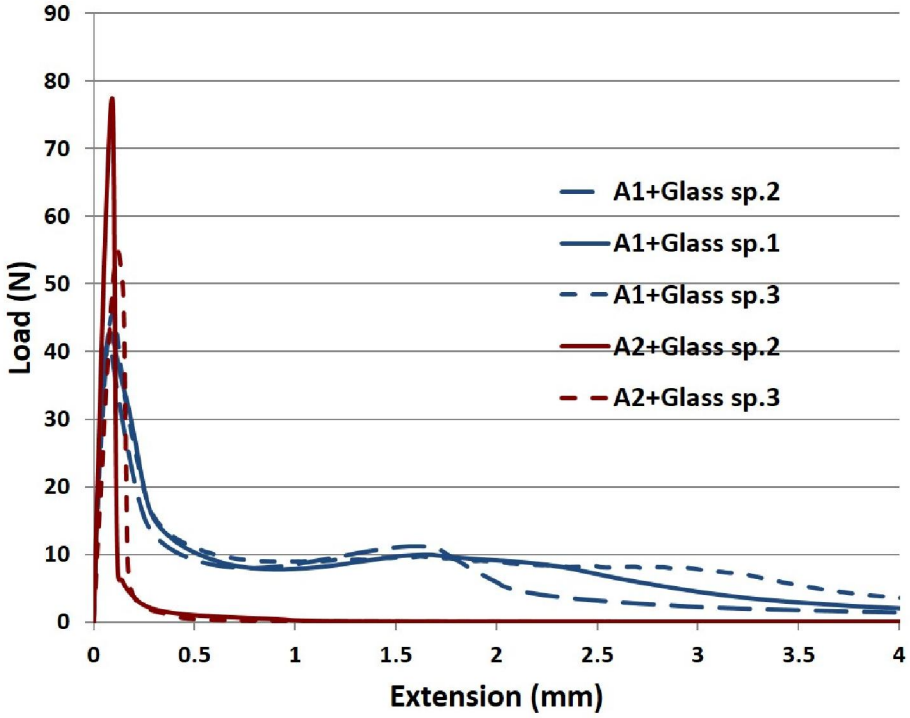

Figure 4-15: Force vs. displacement curves for probe tests on A gum cuds on Glass substrates

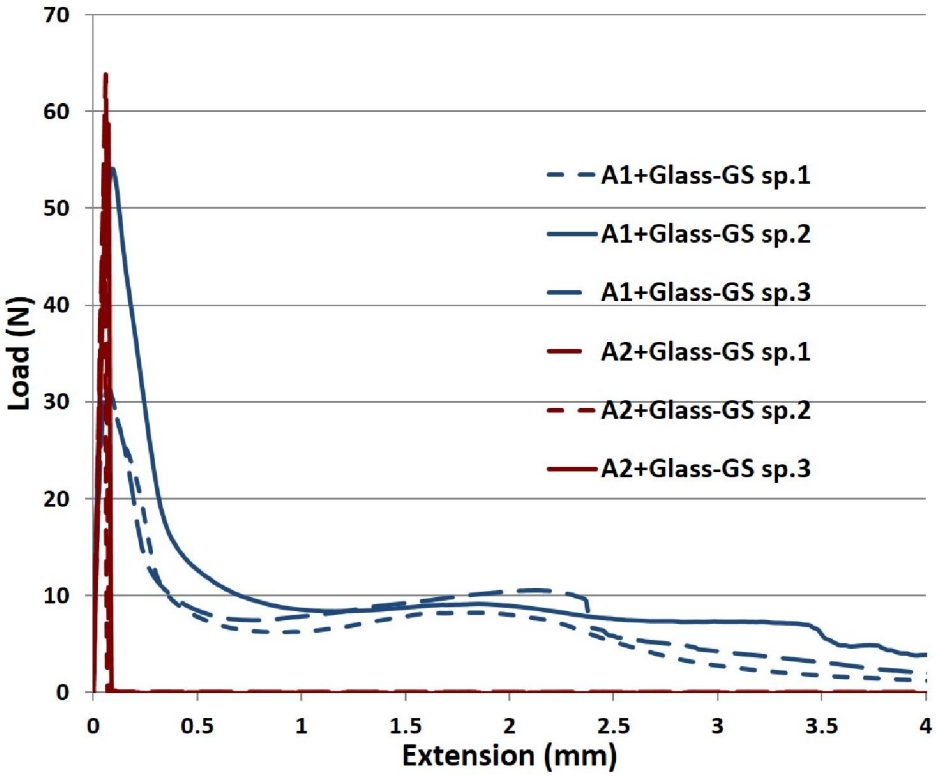

Figure 4-16: Force vs. displacement curves for probe tests on A gum cuds on Glass-GS substrates

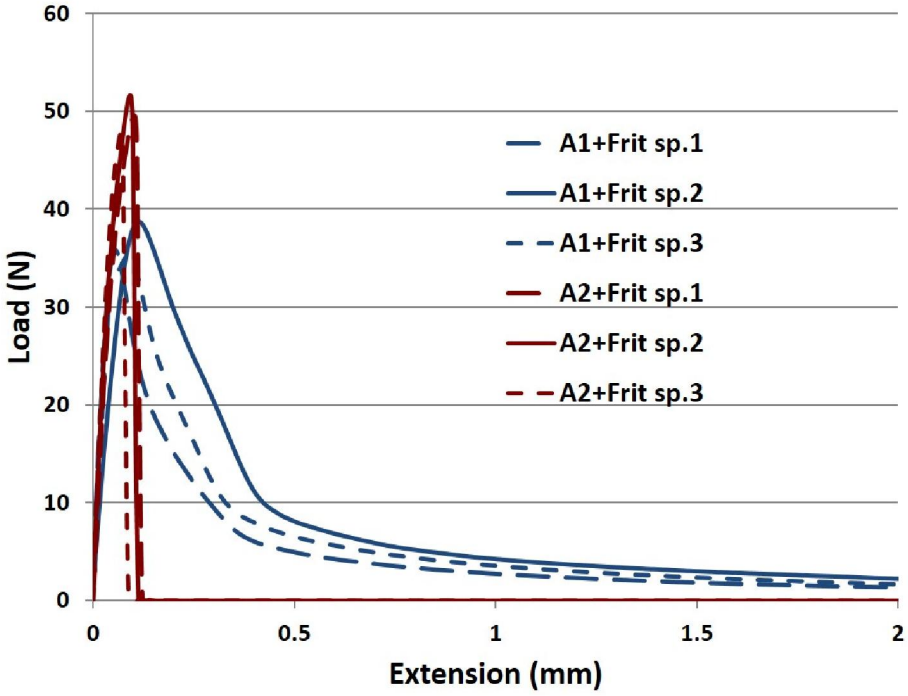

Figure 4-17: Force vs. displacement curves for probe tests on A gum cuds on Frit substrates

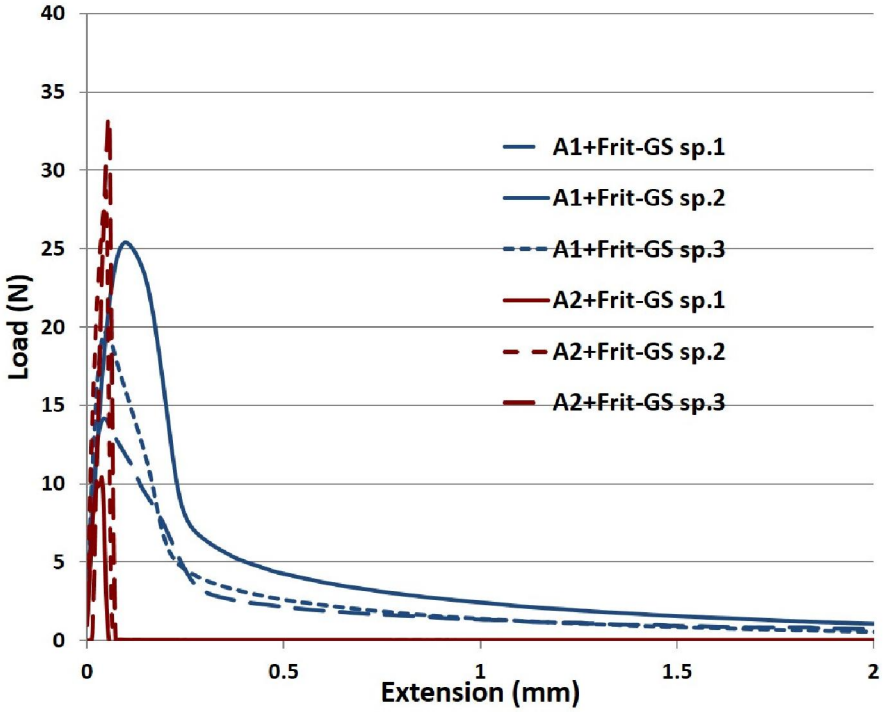

Figure 4-18: Force vs. displacement curves for probe tests on A gum cuds on Frit-GS substrates

Quantitative discussion

The area under the force vs. displacement curves during the debonding stage of the probe tack tests is often used as a metric to compare and discriminate the adhesion performance of the materials. This area is considered as debonding work required for separating the adhesive from the test substrate [11, 12, 17]. Figure 4-19 and Figure 4-20 show comparisons of area under the curves (debonding work) for probe tests conducted on all four types of substrates. Error bars represent ± one standard deviation. Mean values and standard deviations are included in Appendix B. All the following observations are based on "t-tests" at $\alpha = 0.05$. Differences in means and p-values are included in Table 4-4 through Table 4-6. From Figure 4-19 and Figure 4-20 it was observed that the B1 and A2 gum cuds showed lower debonding work compared to the A1 specimens across all the substrates tested. Also, as mentioned earlier, A1 gum cuds showed cohesive failures, while B1 and A2 gum cuds showed apparent interfacial failures. Interestingly for probe tests on similar substrates, A1 gum cuds had shown a higher tan delta value, suggesting higher dissipation compared to B1 and A2 gum cuds at relevant debonding timescales (Table 4-2). These observations are similar to observations reported for probe tests on soft materials, where it has been observed that higher debonding energies often correspond with higher tan δ values [14]. Nevertheless the interaction of other properties such as yield strength, nonlinear behavior, and complex stress state in case of rough surfaces can also play a role in the observed failure modes and corresponding areas under the curve. The focus of this initial study is to develop a test method to obtain insights into the adhesion characteristics of gum cuds, hence during this initial study only the linear viscoelastic properties of gum cuds were considered. From Figure 4-19 it was observed that when the test substrate roughness was increased (Glass vs. Frit), A1 gum cuds showed larger drop in area under the curve compared to B1 gum cuds. This was due to the absence of shoulder regions in B1 cuds when tested on Glass substrates, where shoulder regions are typically associated with energy dissipation due to fibrillation mechanisms. Interestingly, for the case of A1 gum cuds, it can be observed that the application of the GS solution did not show any significant effect on area under the curves for tests on smooth surfaces while a reduction in area under the curve was observed when a gum stopper solution was applied on rough surfaces. This indicates that

applications of GS solution might be affecting the energy dissipation mechanisms during the tests on rough surfaces while GS solution effects might not be significant when tested on smooth surfaces. These observations will be discussed in more detail in following sections. Thus, using probe test debond force vs. displacement curves were successfully quantified. The debond force vs. displacement curves offer valuable insights into adhesion performance of the gum cuds. This data now can be used to gather insights about the effect of gum cud rheology and test substrate surface properties and topology on the adhesion performance of the gum cuds. Effect of these variables on the gum cud performance will be discussed in the following section.

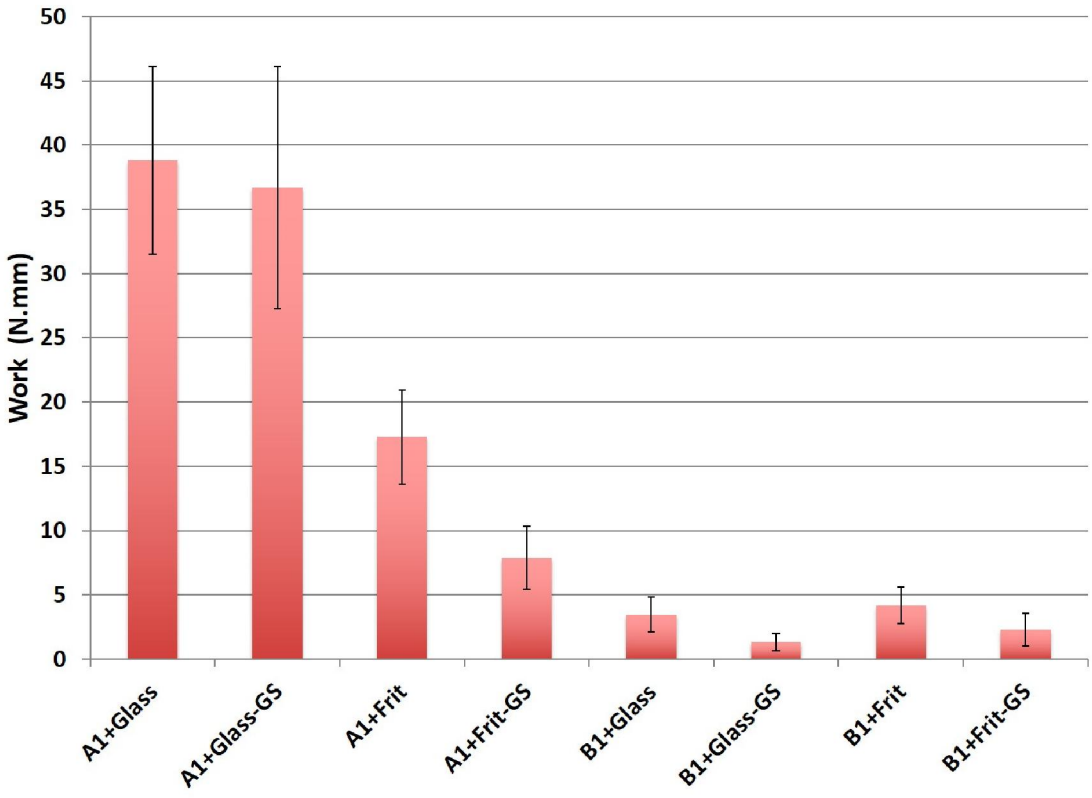

Figure 4-19: Comparison of area under the curves for B1 and A1 specimens

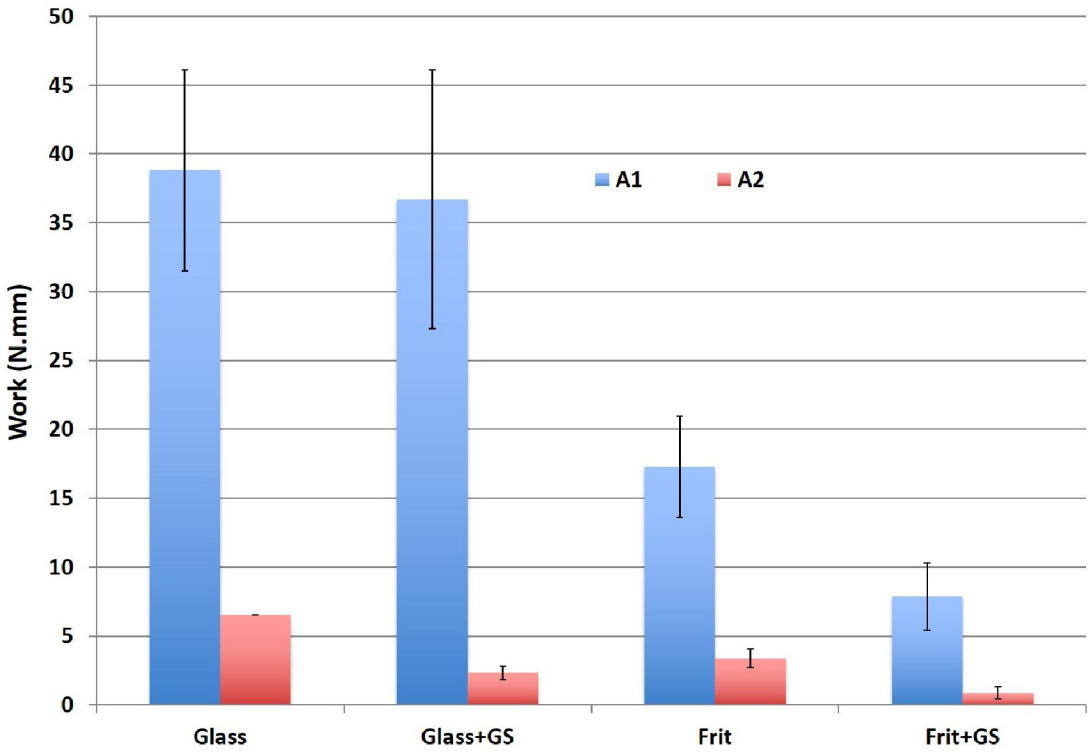

Figure 4-20: Comparison of area under force vs. displacement curves for A type specimens

4.3.3 Effect of substrate surface and gum rheological properties on gum adhesion

4.3.3.1 Effect of Surface Energy

As mentioned earlier application of gum stopper solution on the given substrate reduces the surface energy of the substrate. This effect is reflected in estimated thermodynamic work of adhesion (estimated using substrate surface energies and Fowke's approximation of interfacial surface energy, Appendix E) between gum cuds and the substrate. Table 4-3 shows an estimated thermodynamic work of adhesion for all the substrate-gum cud combinations used in the probe tests. As seen in Table 4-3 thermodynamic work of adhesion between a gum cud and the substrate was lower for substrates having a gum stopper solution coating.

Table 4-3: Thermodynamic work of adhesion

Gum cud-Substrate	mJ/m^2	Standard deviation
A2 on Glass	92.62	15.12
B2 on Glass	82.80	16.96
B1 on Glass	83.27	13.33
A1 on Glass	83.27	12.44
A2 on Glass-GS	46.91	11.70
B2 on Glass-GS	42.30	9.31
B1 on Glass-GS	46.71	7.77
A1 on Glass-GS	42.72	7.18

Application of GS solution on the substrate and its effect on gum cud adhesion performance is summarized in Table 4-4. In Table 4-4 to Table 4-6, an upward or a downward arrow indicates an increase or a decrease in the area under the curve respectively. The changes in the areas are reported if a statistically significant difference is observed based on "t- test" at $\alpha = 0.05$. A '*' indicates the cohesive failure mode or a change in the failure mode. From Table 4-4 it can be observed that the decrease in the thermodynamic work of adhesion for a given substrate correlated with the decrease in the area under the curve. This was probably due to reduced access to energy dissipation mechanisms with decrease in the thermodynamic work of adhesion [7]. For some substrates, it was difficult to assign trends due to scatter in the data.

Table 4-4: Effect of application of GS solution and resulting decrease in thermodynamic work of adhesion on the gum cud debonding work for a given substrate

	A1*		A2		B1		B2	
	Smooth	Rough	Smooth	Rough	Smooth	Rough	Smooth	Rough
Increase/ Decrease/ No change	--	↓	↓	↓	↓	--	↓	--
% Change	--	54.3	62.5	74.4	62.1	--	40.43	--
p-value	0.38	0.010	0.0023	0.0028	0.03	0.08	0.03	0.07

4.3.3.2 Effect of Surface Roughness

From Figure 4-19 and Figure 4-20 it was observed that for all gum cuds except B1 and for a substrate having a given surface energy (with or without GS treatment), the area under the curve decreases when the roughness of the substrate is increased. For B1 specimens it was difficult to assign trends due to the presence of overlapping error bars. Table 4-5 summarizes the effect of surface roughness (comparing smooth glass vs. frit) on gum adhesion (area under the curve) for all the gum cuds. It can be seen that increasing the roughness of the substrates lead to decrease in the area under the curves. For some substrates the average area under the curve showed a decrease though the decrease in the area was not statistically significant (represented by a dash).

Table 4-5: Effect of changing the surface roughness (going from Glass to Frit substrates) for a given surface energy on gum cud debonding work

	A1*		A2		B1		B2	
	No GS	GS	No GS	GS	No GS	GS	No GS	GS
Increase/ Decrease/ No change	↓	↓	↓	↓	--	--	↓	↓
% Change	55.57	78.55	48.6	62.9	--	--	77.5	87.5
p-value	0.0051	0.0034	0.007	0.009	0.28	0.15	0.007	0.0026

Similar observations have been reported in the literature for a soft material coming into contact with a rough substrate [17-20]. It has been suggested that when the test substrate is rough, the soft material has to deform according to the topology of a given rough substrate leading to stored elastic energy due to elastic modulus component of the material. At the same time there is a gain in thermodynamic work of adhesion as the soft material comes into contact with the surfaces of asperities and hills of rough surface. Thus, the elastic energy stored while deforming the gum cud along the surface topology is competing against the energy gained due to thermodynamic work of adhesion. Thus, minimization of total energy of the system leads to a loss in contact area, resulting in decreased adhesion [17-23]. As shown in Figure 4-19, at the bonding time scales the storage modulus of A1 gum cuds was higher than the storage modulus of B1 gum cuds. A similar trend was observed for the magnitude of complex moduli calculated

using storage and loss components. Thus the elastic penalty for A1 gum cuds to deform according to the topology of the substrates would be higher compared to B1 gum cuds. Interestingly, as mentioned earlier, it was observed that when the test substrate roughness was increased (Glass to Frit), A1 gum cuds showed a larger drop in area under the curve compared to that for the B1 gum cuds (Figure 4-19). Even though these results seem to agree with the proposed theory on decrease in adhesion of soft materials with an increase in the roughness, it must be noted that the proposed theory is based on the probe tests on the partially or fully cross-linked soft materials while the gum cud formulations are un-crosslinked materials. As mentioned earlier application of GS solution leads to decrease in thermodynamic work of adhesion. An interesting observation from Table 4-5 is the higher drop in area for a given gum cud when tested on GS-Frit surfaces compared to Frit surfaces. This indicates an interaction between thermodynamic work of adhesion and roughness of the substrate. In the absence of GS layer, thermodynamic work of adhesion would be higher along the asperities of the Frit surface, and lower thermodynamic work values are expected in presence of GS solution. In light of differences in thermodynamic work of adhesion, the wetting and penetration of gum cuds for GS coated and uncoated Frits would be different. Also, due to reduced thermodynamic work of adhesion for GS-Frit substrates, access to energy dissipation mechanism might be restricted as compared with Frit substrates. However, it should be noted that other properties such as yield strength, non-linear behavior as well as stress state at the gum cud-substrate interface can also play a role in determining debonding work.

4.3.3.3 Effect of Changes in Tan δ

In order to study the effect of tan δ on the gum adhesion, tan δ values at approximate debonding timescales were considered. Tan δ values at debonding timescales are listed in Table 4-2. As mentioned earlier reducing the flavoring agent in each gum type led to changes in tan δ values. For A type gum cuds, reducing the flavoring agent led to a decrease in tan delta while the opposite effect was observed for B type of gum cuds. Thus for a given type of gum cud, adhesion performance can be studied as a function of an increase in tan δ values at debonding timescales. From Table 4-2 it can observed that for B type gum cuds, tan δ increased in going from B1 to B2. Table 6 summarizes the effect of increasing tan δ on the debonding work of the gum

cuds. For B type gum cuds it was observed that for an increase in tan δ, gum adhesion increases on smooth surfaces but decreases on rough surfaces. An increase in tan δ resulted when going from A2 to A1 type gum cuds, which showed a significant increase in adhesion with increase in tan δ, though it must be emphasized that the failure modes were different for A1 and A2 gum cuds.

Table 4-6: Effect of increase in tan δ on area under the curves

	B				A*			
	Glass	Glass-GS	Frit	Frit-GS	Glass	Glass-GS	Frit	Frit-GS
Increase/ Decrease/ No change	↑	↑	↓	--	↑	↑	↑	↑
% Change	71.1	168.7	68.10	--	493.7	1481.8	413.4	815.1
p-value	0.03	0.02	0.04	0.06	0.008	0.01	0.001	0.004

4.3.4 Correlating Viscoelastic Properties with Gum Adhesion

Based on the theoretical works by Kinloch et al. [24-26], the Dahlquist criterion, and proposed bonding and debonding mechanisms in PSAs, Tse et al. [27] proposed that PSA performance can be expressed as

$$T \sim P_0 BD \tag{4.1}$$

where P_0 is an intrinsic interfacial failure energy (either the energy required to open up a unit area of PSA-substrate interface in the absence of viscoelastic energy loss or the thermodynamic work of adhesion which is substrate dependent). B and D are functions corresponding to bonding and debonding contributions, respectively. A bonding function is related to the compliance of an adhesive while debonding function is related to the viscoelastic loss modulus of an adhesive at relevant time scales, respectively [28]. Table 4-3 shows an estimated thermodynamic work of adhesion for all the substrate-gum cud combinations used in the probe tests. As mentioned earlier, the bonding term is related to the compliance of an adhesive at relevant time scales. In our case, approximate bonding time scales correspond to about 0.01 rad/sec. Unfortunately, the rheological properties were not available at 0.01 rad/sec, thus storage modulus at 0.1 rad/sec was used to

estimate a compliance-like bonding function by

$$B = \frac{1}{E'\left(\omega_{bonding}\right)}$$

The debonding term in equation 4.1 is related to the loss modulus at debonding time scales. Loss moduli corresponding to these time scales were then used to estimate the debonding function as

$$D = E''\left(\omega_{debonding}\right)$$

In order to account for the effect of substrate roughness on debonding work, a roughness function was introduced in the Equation 4.1 leading to

$$Work \sim W_{adhesion} \cdot B \cdot D \cdot \Re \tag{4.2}$$

$$\Re = 1 - \left| \frac{\xi \cdot z_{rms}}{h} \right| \tag{4.3}$$

Here h is the adhesive thickness, z_{rms} is the root mean square roughness of the substrates and ξ is a constant. For smooth surfaces, z_{rms} is nearly zero and the roughness function reduces to one. In light of trends observed in Figure 4-19, a negative sign was introduced in Equation 4.3 that leads to a reduction in overall area under the curve in Equation 4.2 with increasing z_{rms} or roughness of the substrate. In the current form, Equation 4.2 is an approximate relationship thus a constant φ was introduced leading to

$$Work = \varphi \cdot W_{adhesion} \cdot B \cdot D \cdot \Re \tag{4.4}$$

In Equation 4.4, all quantities except φ and ξ were experimentally measured. Figure 4-21 compares the debonding work predicted using Equation 4.4 *(φ =0.077 and ξ = 29.07)* with experimentally measured debonding work (area under the curves) during

the probe tests. φ and ξ were determined through least square fitting of equation 4.4 such that R^2 was maximum.

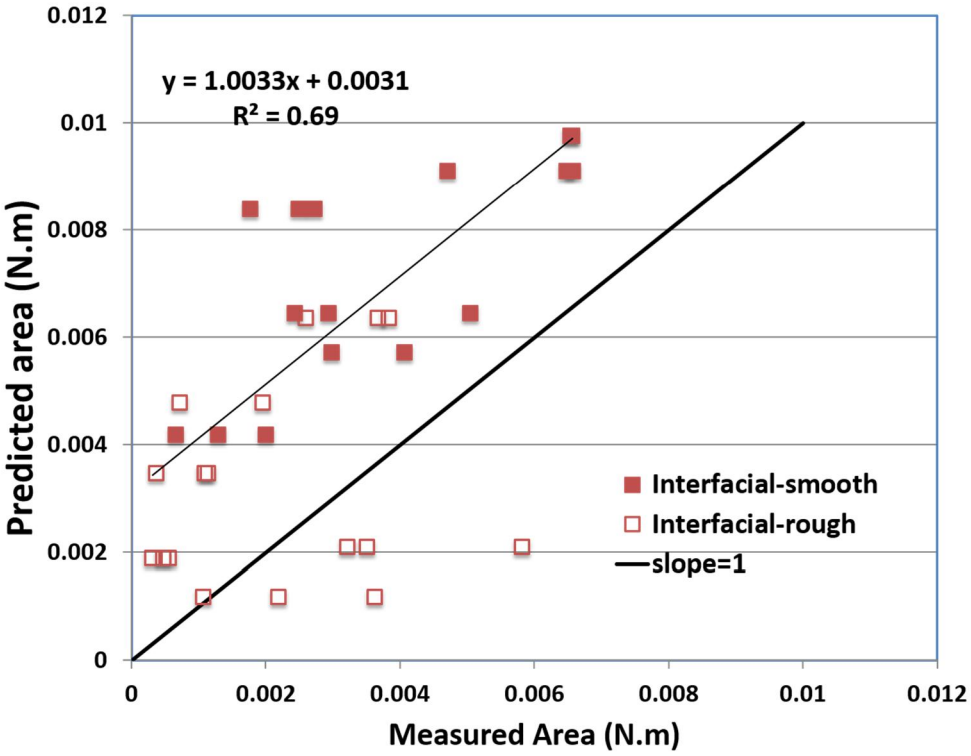

Figure 4-21: Comparison of predicted areas using equation 4.4 with measured areas, R^2 values do not include B1 specimens tested on rough substrates

Data from the probe tests resulting in cohesive failure modes were not included in this analysis. Except for B1 specimens tested on rough substrates (highlighted using ellipse), a good correlation between the predicted and measured data was observed with a R^2 value of 0.69 when B1 data was not included, though including B1, R^2 value becomes 0.34. Also, except for B1 gum cuds tested on rough substrates, areas predicted using equation 4.4 were consistently higher than the experimentally measured areas. At this point sources of higher predicted areas compared to measured areas are unknown. Even though rheological measurements involve small strains and probe tests involve large strains, slope from Equation 4.4 shows a reasonable correlation between viscoelastic properties and thermodynamic work of adhesion with probe tests results. It was

interesting to note that an approximate relationship such as Equation 4.1 showed a reasonable correlation (R^2 = 0.69) with probe tests trends. Nevertheless Equation 4.1 provides valuable insights into the effects of rheological properties and surface energies of the gum cuds on adhesion performance that could be insightful towards formulating gum formulations with less adhesion.

4.4 Conclusions

In this study a probe test based approach was developed to obtain insights into the effect of surface energy and surface roughness on gum cud adhesion. This approach enabled the introduction of substrates having well defined surface energies and surface topologies to elucidate the effect of these parameters on gum cud adhesion. A gum cud processing technique was introduced to easily and reproducibly process gum cuds in a way that mimics a chewing process, which facilitated the preparation of gum cuds samples with consistent properties. Rheological properties of gum cuds, surface properties of gum cuds as well as test substrates were successfully quantified. Using probe test based approach adhesion performance (debonding work) of gum cuds on substrates having well defined topology and surface chemistry was successfully quantified. Four different types of gum cuds, B1, B2, A1 and A2 were tested during this study. It was observed that A type and B2 gum cuds showed a decrease in debond energy when the roughness of the substrate was increased. B1 type gum cuds did not show a significant change in debond energy upon changing the roughness of the substrate. For all the gum cuds tested in this study decreasing the surface energy of substrates led to a decrease in debond energy except for A1 gum cuds when tested on smooth surfaces and B1 gum cuds when tested on rough surfaces, where no significant reduction in debond energy was observed. An approximate equation was proposed that correlated the effects of surface energies, substrate roughness and gum cud rheology with the gum cud adhesion performance observed in probe tests.

4.5 References

[1] L. F. Research. (2012). *Innovations in the Global Confectionary Market*. Available: http://www.leatherheadfood.com/index.php?page=global-confectionery-market&action=updateCurrency&currentCurrency=USD

[2] M. M. Abdel-Malik, A. Vishwanathan, and A. M. Orama, "Non-Stick Chewing

Gum Base," ed: U.S. Patent 6,599,542, 2003.
[3] K. S. Lin, "Non-Stick Chewing Gum," ed: U. S. Patent 20140087022, 2014.
[4] G. Mansukhani, J. J. Kiefer, and N. D'Ottavio, "Non-Stick Chewing Gum," ed: U. S. Patent 5,601,858, 1997.
[5] A. J. Comollo, "Non-tack chewing gum composition," ed: U. S. Patent 3,984,574, 1976.
[6] D. Satas, *Handbook of Pressure Sensitive Adhesive Technology*: Van Nostrand Reinhold, 1989.
[7] C. Creton, "Pressure-Sensitive Adhesives: An Introductory Course," *MRS Bulletin,* **28**, 434-439, 2003.
[8] L. Li, M. Tirrell, G. A. Korba, and A. V. Pocius, "Surface Energy and Adhesion Studies on Acrylic Pressure Sensitive Adhesives," *The Journal of Adhesion,* **76**, 307-334, 2001.
[9] C. Creton, J. Hooker, and K. R. Shull, "Bulk and Interfacial Contributions to the Debonding Mechanisms of Soft Adhesives: Extension to Large Strains," *Langmuir,* **17**, 4948-4954, 2001.
[10] E. M. Petrie, *Handbook of Adhesives and Sealants*: McGraw-Hill New York, 2000.
[11] A. Zosel, "Adhesion and Tack of Polymers: Influence of Mechanical Properties and Surface Tensions," *Colloid and Polymer Science,* **263**, 541-553, 1985.
[12] A. Zosel, "Adhesive Failure and Deformation Behaviour of Polymers," *The journal of adhesion,* **30**, 135-149, 1989.
[13] C. Gay and L. Leibler, "Theory of Tackiness," *Physical Review Letters,* **82**, 936-939, 1999.
[14] K. Brown, J. C. Hooker, and C. Creton, "Micromechanisms of Tack of Soft Adhesives Based on Styrenic Block Copolymers," *Macromolecular Materials and Engineering,* **287**, 163-179, 2002.
[15] A. J. Crosby, K. R. Shull, H. Lakrout, and C. Creton, "Deformation and Failure Modes of Adhesively Bonded Elastic Layers," *Journal of Applied Physics,* **88**, 2956-2966, 2000.
[16] I. Chikina and C. Gay, "Cavitation in Adhesives," *Physical Review Letters,* **85**, 4546-4549, 2000.
[17] D. Martina, C. Creton, P. Damman, M. Jeusette, and A. Lindner, "Adhesion of Soft Viscoelastic Adhesives on Periodic Rough Surfaces," *Soft Matter,* **8**, 5350-5357, 2012.
[18] A. Chiche, P. Pareige, and C. Creton, "Role of Surface Roughness in Controlling the Adhesion of a Soft Adhesive on a Hard Surface," *Comptes Rendus de l'Académie des Sciences - Series IV - Physics,* **1**, 1197-1204, 2000.
[19] K. N. G. Fuller and D. Tabor, "The Effect of Surface Roughness on the Adhesion of Elastic Solids," *Proceedings of the Royal Society of London. A. Mathematical and Physical Sciences,* **345**, 327-342, 1975.
[20] Y. Peykova, S. Guriyanova, O. V. Lebedeva, A. Diethert, P. Müller-Buschbaum, and N. Willenbacher, "The Effect of Surface Roughness on Adhesive Properties of Acrylate Copolymers," *International Journal of Adhesion and Adhesives,* **30**, 245-254, 2010.
[21] J. A. Greenwood and J. B. P. Williamson, "Contact of Nominally Flat Surfaces,"

Proceedings of the Royal Society of London. Series A. Mathematical and Physical Sciences, **295**, 300-319, 1966.

[22] K. N. G. Fuller and A. D. Roberts, "Rubber Rolling on Rough Surfaces," *Journal of Physics D: Applied Physics,* **14**, 221, 1981.

[23] C. Y. Hui, Y. Y. Lin, and C. Creton, "Bonding of a Viscoelastic Periodic Rough Surface to a Rigid Layer," *Journal of Polymer Science Part B: Polymer Physics,* **40**, 545-561, 2002.

[24] A. N. Gent and A. J. Kinloch, "Adhesion of Viscoelastic Materials to Rigid Substrates. Iii. Energy Criterion For Failure," *Journal of Polymer Science Part A-2: Polymer Physics,* **9**, 659-668, 1971.

[25] E. H. Andrews and A. J. Kinloch, "Mechanics of Adhesive Failure. I," *Proceedings of the Royal Society of London. A. Mathematical and Physical Sciences,* **332**, 385-399, 1973.

[26] E. H. Andrews and A. J. Kinloch, "Mechanics of Adhesive Failure II," *Proceedings of the Royal Society of London. A. Mathematical and Physical Sciences,* **332**, 401-414, 1973.

[27] T. Mun Fu, "Studies of Triblock Copolymer-Tackifying Resin Interactions by Viscoelasticity and Adhesive Performance," *Journal of Adhesion Science and Technology,* **3**, 551-570, 1989.

5 Creep Rupture Performance of Silicone Sealants for Solar Panel Support Applications

5.1 Introduction

Sealants are traditionally used in building and engineering structures to seal the gaps between similar or dissimilar materials, act as a barrier against environmental factors, and offer waterproofing capabilities [1]. Sealants are designed such that, at service temperatures, they typically have low modulus and are capable of withstanding large deformations before failure occurs [1]. These properties are required where a joint to be sealed will undergo considerable expansion or contraction throughout the service life. Several chemical families of sealants are available in the market including acrylics, polyurethanes, and silicones, to name a few. Amongst these families, silicone-based sealants are known for their high UV, chemical and thermal resistance [2]. Crosslinked silicones have a low glass transition temperature (about -120°C for polydimethylsiloxanes) and satisfactorily maintain elongational properties till around -40°C at which crystallization is observed for polydimethylsiloxane-based silicone sealants [2]. In addition, due to their high thermal decomposition temperatures, silicones can function in a wide range of temperatures [3]. Silicones typically have low surface energy (e.g. 20.4 mJ/m^2 for polydimethylsiloxanes), thus they are capable of wetting most of the surfaces [4]. Due to these properties, combined with their excellent weatherability, silicone-based sealants are used extensively in many outdoor applications [5]. Apart from traditional applications as sealants, recent advances in silicone sealant formulations have rendered them useful in load-bearing applications such as structural glazing to adhere glass, metal or other façade panels to the supporting structure of a building [5, 6], where loads are transferred through silicone sealants.

One of the emerging load-bearing applications of silicone sealants is in the field of bonding solar modules to the supporting rail structures. The use of sealants offers convenience and a potential reduction in mounting times compared to using mechanical fasteners. Apart from savings in cost, time and number of components, use of sealants instead of mechanical fasteners may avoid the stress concentrations arising due to use of

mechanical fasteners. Unlike applications such as structural glazing, where sealants have been used for many years and for which long-term performance data is available, new silicone sealant formulations for solar panel support applications or for other emerging load bearing applications do not have a well-established performance history. Generating accurate and a reliable long-term performance history for a new sealant and application typically requires extensive outdoor and in service testing. In light of ever shortening product development cycles, accelerated laboratory testing can offer valuable insights into the long-term performance of the product [5]. Sandburg et al. reported one such study, where silicone sealants designed for structural glazing applications were subjected to different levels of constant stress, and time to failure was noted. Based on the gathered data, stress vs. life relationships were proposed using applied stress levels as the sole accelerating factor [7]. Sugiyama el al. conducted a similar study on seven different silicone sealants designed for structural glazing applications, where tests were carried out using shear and tensile loading configurations [8]. Townsend et al. reported a study aimed at characterizing and evaluating acrylic foam PSA tapes for structural glazing applications. In this study stress as well as temperature was used as the accelerating factors allowing tests performed under practical time constraints to simulate creep rupture failure times as long as one year [9, 10]. Stögbauer et al. studied the effect of heat aging on elongation and ultimate tensile strength of commercially available construction silicone sealants. The sealants were aged at elevated temperatures for prescribed lengths of time and mechanical properties were recorded upon cooling. Here, elevated temperatures were used to gather insights in to long-term thermal degradation effects [11]. Similar studies have been carried out to study long-term exposure effects of factors such as UV radiation, moisture and other outdoor weathering variables [5, 8, 12, 13]. It should be noted, however, that even if accelerated laboratory testing can be useful in discriminating long term performance of the products, the predictions from accelerated testing still need to be validated in order to be considered reliable for design purposes.

This study highlights a procedure to obtain insights into and compare the long-term performance of three different silicone sealants designed for load-bearing applications for solar panel support sealants, though the techniques and materials may also be relevant in other engineering and building structures. Creep rupture tests were

carried out with a 72-station creep frame at three different load levels and at three different humidity and temperature combinations. Using the time temperature superposition principle (TTSP), thermal shift factors were obtained from dynamic mechanical analysis (DMA). These thermal shift factors obtained at small cyclic strain levels were used to form reasonably smooth master curves for the data from ramp to fail tests. This provided a phenomenological viscoelastic framework for application of DMA-generated TTSP shift factors to large strain failure data. Thus, data from creep rupture tests were shifted using shift factors from DMA tests to form creep rupture master curves as well. The creep rupture master curves, coupled with proposed stress vs. life relationships, provide insights into the long-term creep rupture performance of silicone sealants. For a given joint configuration and sealant type, the use of both temperature and stress as accelerating factors and TTSP allowed estimation of delayed failures corresponding to three years through experiments carried out in one month.

5.2 Experimental

5.2.1 Materials

Though specific formulations are not reported, a typical silicone sealant formulation consists of silicone-based resin, a crosslinking agent, catalyst, coupling agents, surfactants, and fillers such as silica or carbon black, etc. Catalyst is added to increase the rate of crosslinking while fillers are added for rheological control and cost purposes. Coupling agents are added to improve the adhesion to a range of substrates, while surfactants are added to enhance wettability [14]. Three silicone sealants A, B, C were used during this study. The materials were prepared and supplied by sponsors. As reported by sponsors, sealants A and B contained carbon black while sealant C contained titanium dioxide as one of the filler material. All three sealants were moisture cured under controlled humidity and temperature conditions.

5.2.2 Test specimens

All specimens were prepared by sponsors and allowed to cure for at least 60 days before testing. As per sponsors, sealant B was reported to be representative amongst the three sealants, and was used to conduct constitutive tests. Cylindrical disk specimens having dimensions of 9.5 x 2.05 mm (diameter x thickness) were punched from the cured

sheets (2.05 mm thickness) and used for shear testing of constitutive properties in DMA tests. Apart from bulk sealant materials, two types of bonded joint specimens were used during this study. One set of specimens (referred here on as "Al-Al" specimens) had anodized aluminum as adherends. Anodized aluminum is commonly used material during rail bonding application of silicone sealants. It has been observed that bonds made with anodized aluminum adherends exhibit excellent inherent durability due to both the hydration resistance of anodized aluminum surfaces and the imparted roughness leading to subsequent interlocking that occurs between the oxide and the adhesive [15]. Figure 5-1 shows the geometry of the Al-Al specimens. Holes were drilled at each end of the specimen to accommodate loading pins. The other set of specimens had a polyvinyl acetate (PVA) backsheet (0.17 mm thickness) as one adherend and anodized aluminum as the other adherend. These specimens are referred here on as "Al-BS" specimens. PVA is one of the commonly used supporting materials in solar cell modules, so tests including this material provide insights into the performance of sealants when attached to PVA supporting structure in the solar cell module. The Al-BS specimens had a similar geometry as the Al-Al specimens, with the PVA adherend having the same dimensions as the wider adherend used in Al-Al specimens. Similar to the Al-Al specimens, holes were drilled at each end of Al-BS specimens. PVA adherends were thin and flexible in nature, which upon loading during preliminary tests led to failures near the loading hole. In order to avoid failures within PVA adherends, and to characterize the performance of sealants when PVA was one of the adherends, steel plates were used to clamp flexible PVA adherend to the anodized aluminum plate via bolts, as shown in Figure 5-2. The supporting anodized aluminum plates had a hole concentric with the hole in PVA adherend, through which loading pins would pass through. The anodized aluminum when used as a supporting structure assisted in distributing the load at the loading holes and within PVA adherends, thus avoiding undesired failures in PVA adherends.

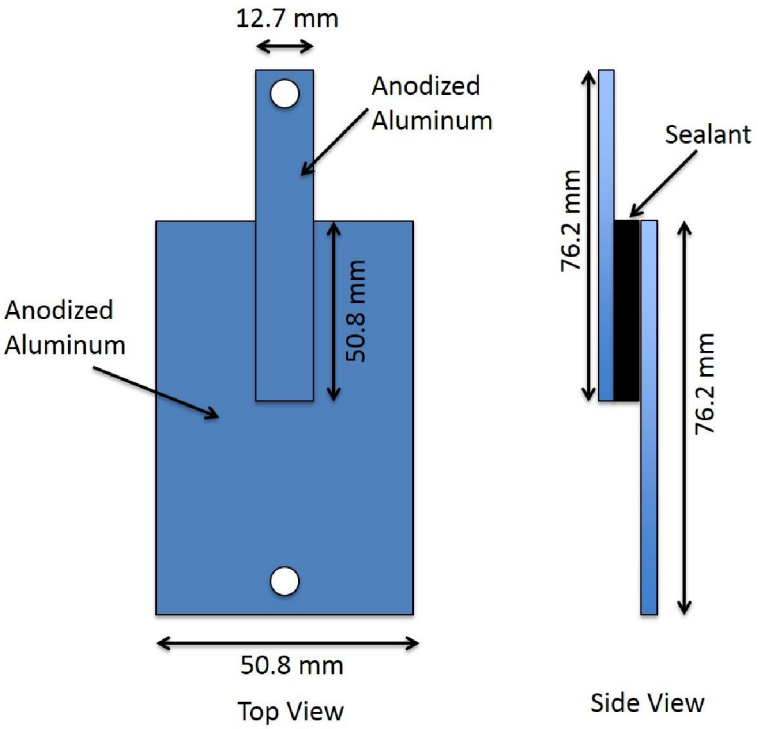

Figure 5-1: Geometry of the Al-Al specimens used for ramp to fail and creep rupture tests

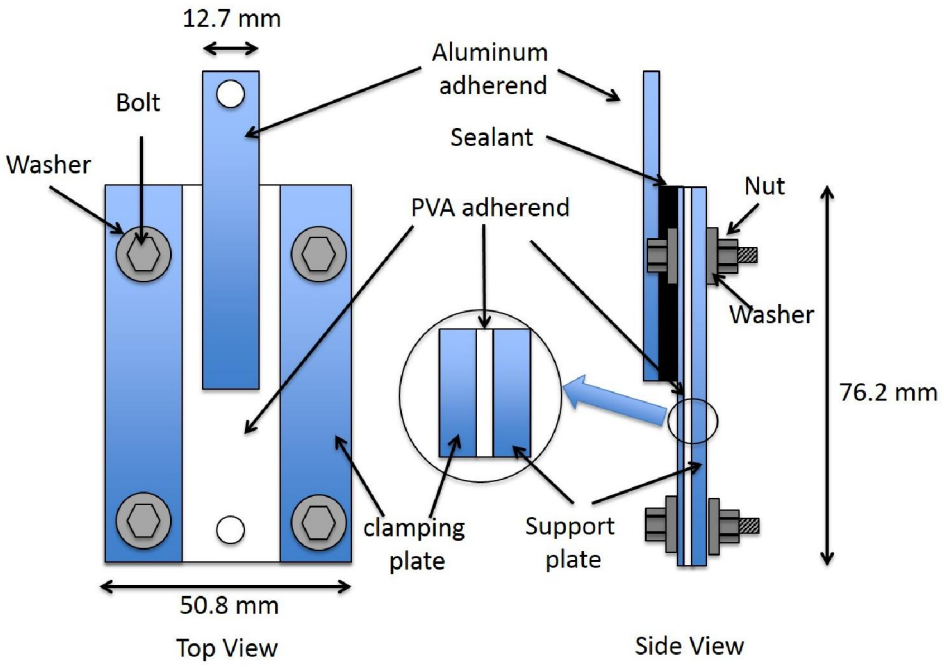

Figure 5-2: Geometry of the Al-BS specimens used for creep rupture tests

5.2.3 DMA tests

In order to obtain quality data over the required range of frequencies and temperatures, several different DMA specimen geometries such as shear sandwich mode, dual cantilever mode, and tension mode were evaluated at several strain amplitude values. Surprisingly, even if these sealants typically have high strain at break values, for tests in the dual cantilever beam geometry and tension mode geometry, specimens failed at grips during the tests, possibly due to stress concentrations at grip edges. Hence these test geometries were abandoned in favor of shear sandwich mode test geometry, which proved to be the most convenient for these materials. As reported by sponsors all three sealants had similar constitutive properties, thus DMA tests were carried out on silicone B sealant using a TA Instruments Q800 Dynamic Mechanical Analyzer.

A dynamic strain sweep test was performed to obtain information about the linear viscoelastic range of sealant B at a given frequency and temperature. This test involved characterizing dynamic mechanical properties of the material through a range of strain values from 0.002 to 10.53 % strain. These tests were performed at 30°C and at 1 Hz frequency. Based on the results obtained during the dynamic strain sweep experiments, the dynamic % strain value within the linear viscoelastic region was chosen such that load levels did not exceed or fall below instrument sensitivity limits.

The tests performed to obtain thermal shift factors at desired temperatures involved multi-frequency tests as the temperature was stepped over the range of interest. Data was recorded at frequencies of 100, 80, 30, 10, 3, 1, 0.3, 0.1 Hz at temperatures from -50°C to 150°C in 10°C increments and at 85°C temperature. The shift factors obtained at relevant temperatures were then used to form master curves for ramp to fail and creep rupture data. The sample dimensions were 10 x 10 x 1.2 mm (length x width x thickness). The data obtained at each temperature increment at the various listed frequencies allowed us to generate master curves using the TTSP, which can be used in predicting long term properties of the material as well as stiffness and damping characteristics as a function of temperature over very broad time scales. At each temperature increment, the specimen was held for 10 minutes before the test started in order to thermally equilibrate. Utilizing the TTSP, data obtained from the multifrequency

tests were shifted horizontally and vertically to generate master curves. The vertical shifts were as prescribed by rubber theory and the horizontal shifts were obtained from shifting the data horizontally to obtain smooth master curves at the selected reference temperature. The resulting master curves could then be appropriately shifted to other desired reference temperatures. In this study, master curves were generated at a reference temperature of 30°C.

5.2.4 Ramp to fail tests

Ramp to fail tests were carried out to explore the applicability of shift factors from small strain DMA constitutive tests to large strain failure tests such as creep rupture. Also, using the constant strain to failure criteria, the failure loads during ramp to fail tests could be potentially useful in determination of approximate creep rupture stress levels that would induce delayed failures in reasonable timeframes. Constant strain rate, ramp to fail tests were performed on silicone C, though based on sponsors input, results for other sealants were expected to be typical for ramp to fail tests compared to creep rupture tests. The geometry of the specimens used for the ramp to fail tests is shown n Figure 5-3. The tests were carried out using an Instron 5800R load frame fitted with a Thermotron temperature control chamber, a convection oven with openings in the top and bottom for the grips and pull rods to pass through. The specimens were tested at -10°C, 30°C and 70°C. Based on shift factors and slopes obtained through DMA master curves, temperatures for ramp to fail tests were chosen such that thermal shifting would lead to sufficient overlap and resulting master curves would cover wide range of timescales in terms of ramp loadings. Temperature was measured using a thermocouple suspended inside the chamber. The specimens were allowed to equilibrate at a desired temperature for 1 to 2 hours prior to testing. Four nominal strain rates were used at each test temperature: 0.0032 s^{-1}, 0.032 s^{-1}, 0.32 s^{-1}, 3.2 s^{-1}. Each set of conditions was replicated with three specimens.

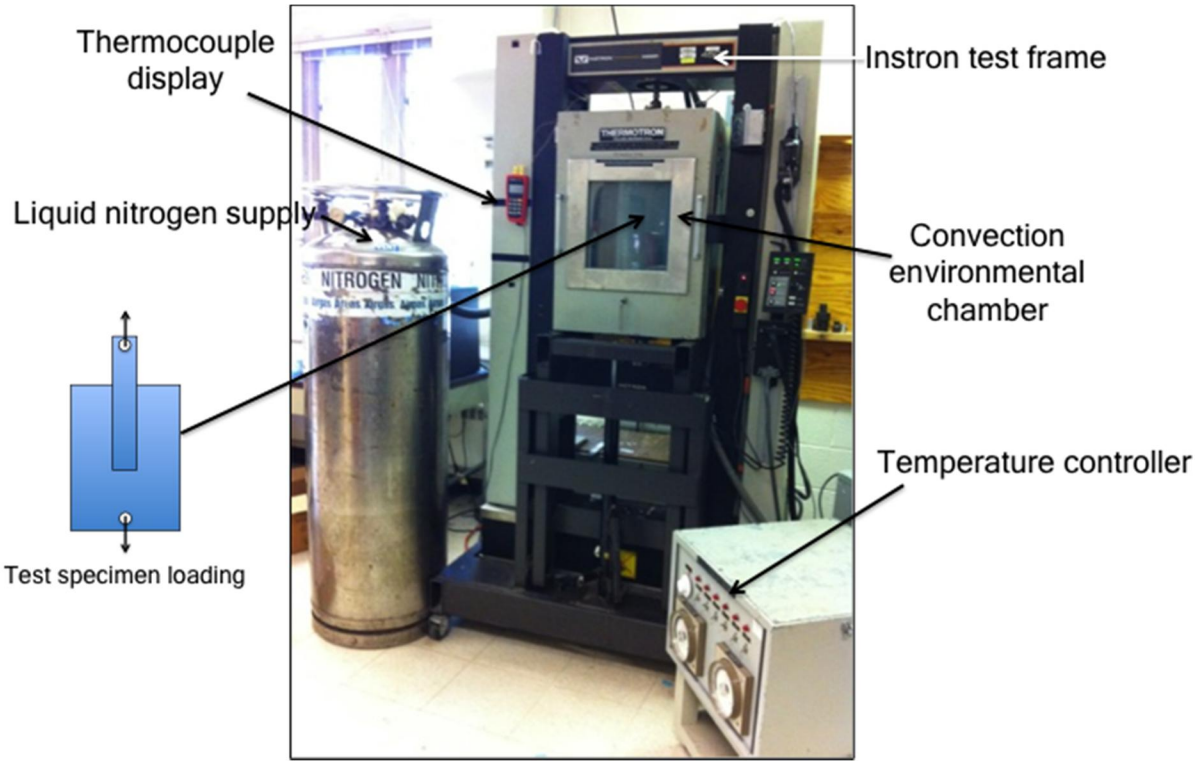

Figure 5-3: Ramp to fail test setup

5.2.5 Creep rupture tests

Figure 5-4 shows the test setup used for creep rupture tests. The creep rupture data was gathered on a pneumatic test frame equipped with 74 Clippard Minimatic COR-24-2 (Cincinnati, OH) double-action air cylinders. The cylinders are capable of applying as much as 534 N (120 lbs.) load when shop air pressure is applied, and could consistently and reliably apply loads as low as 68 N (15 lbs.) [16]. The cylinders are divided into two separate banks with each bank having a pressure regulator so that the pressure in each bank can be controlled independently. In order to record the force applied to the specimens, each bank has an extra cylinder that is mounted outside the test chamber but connected to a common pressure manifold. These two indicator cylinders were attached to separate load cell transducers, and these readings represented the load applied to the specimens. Manually operated open loop pressure regulators were used to control the air pressure within the cylinders thus maintaining a nominally constant force on the test specimens throughout the test. Both banks of cylinders are mounted on top of

a temperature controlled chamber wherein the test specimens are placed. The pneumatic cylinders are attached to the specimens with pull rods, which pass through loose, low friction rubber seals. Failure was recorded when the specimen pulled apart, and the cylinder rod attached to the specimen retracted fully, engaging a switch and disrupting the individual specimen's circuit. The time to failure of each specimen was logged with a LabVIEW™ (National Instruments, Austin, TX, USA) program running on a dedicated laptop computer. The temperature inside the specimen chamber could be maintained from ambient to 85°C using heater coils attached to a feedback loop temperature controller. Circulating air having a desired humidity level was used to control the humidity inside the chambers. In order to generate an air stream with a desired humidity level, compressed dry shop air was preheated to the temperature of the chamber by passing it through copper coils located outside the chambers but maintained at the chamber temperature using the same controller used for maintaining the chamber temperature. The preheated air was then bubbled through a water column kept at chamber temperature. Wet air exiting the water column was then mixed with preheated dry air at the desired ratio in order to obtain humid air with the desired humidity, which was then circulated continuously through the chamber. The desired humidity levels were achieved by manually adjusting the air flow rates of wet and dry air streams till the desired humidity levels were reached. The humidity inside the chamber was monitored using a pre-calibrated Omega RH32P-C2 unit equipped with a RH32P-RP probe type sensor (Omega Engineering Inc., Stamford, CT, USA). Humidity and temperatures in the chambers were monitored and recorded continuously, the temperature variations inside the chamber were within 1°C of the set value and humidity variation was ±2% RH of the set relative humidity level. Figure 5-5 shows a schematic of the humidity control setup. Table 5-1 and Table 5-2 show the test matrix used for the creep rupture tests. The stress levels were chosen such that the time to failures at lowest stress level at all test temperatures would be less than three weeks. In order to determine appropriate stress levels, previously reported creep rupture data of silicone sealants used for solar cell applications was used as a reference [16].

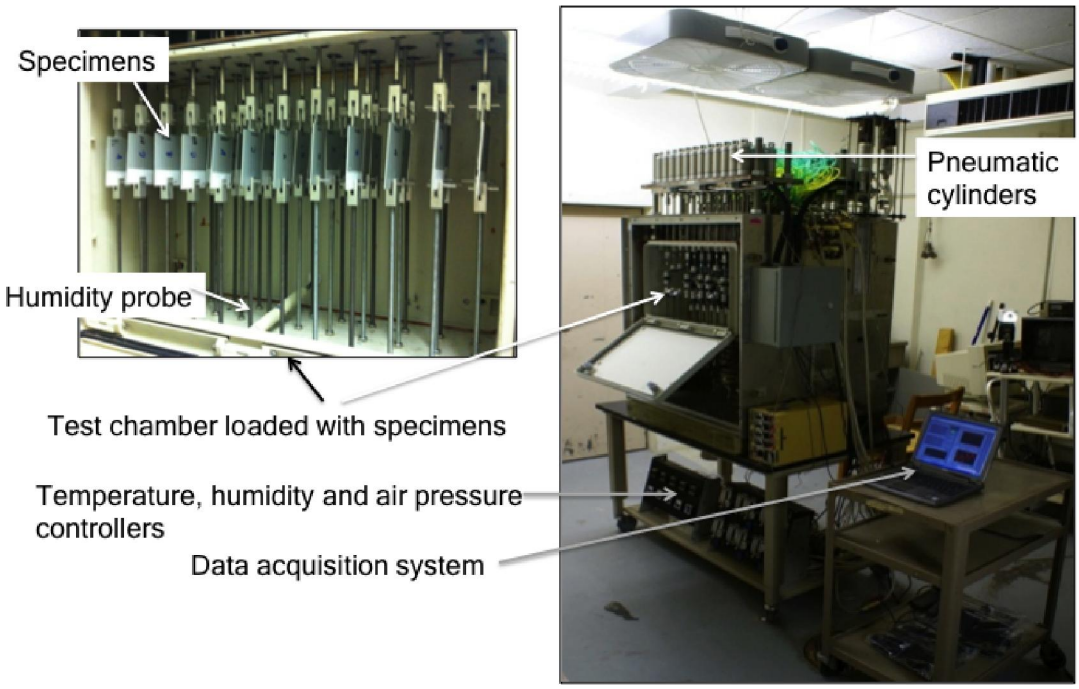

Figure 5-4: Test setup used for creep rupture tests

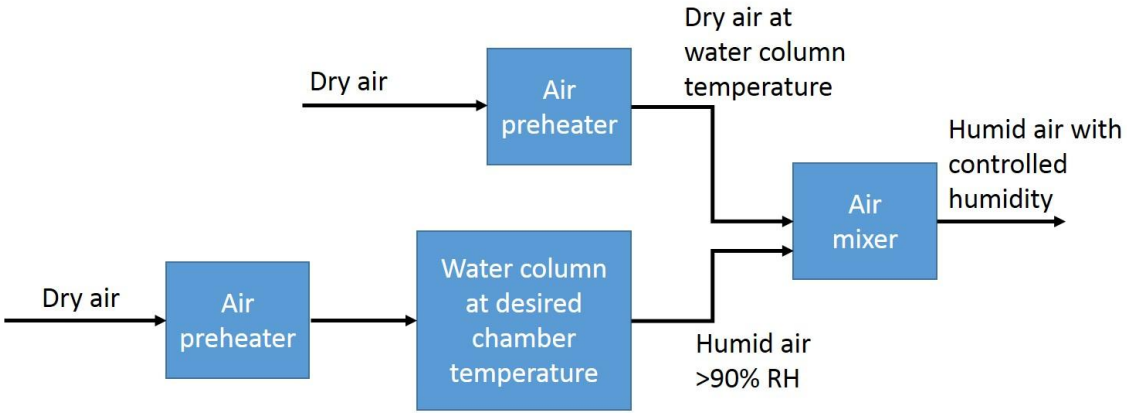

Figure 5-5: Schematic diagram of the humidity control setup

Table 5-1: Test matrix for creep rupture tests on Al-Al specimens

Temperature (°C)	Nominal humidity (%RH)	Nominal shear stress (MPa)	Number of replicates
30	75	0.71	6
		0.61	6
		0.52	6
50	25	0.64	6
		0.53	12
		0.42	12
86	6	0.47	12
		0.37	10
		0.32	10

Table 5-2: Test matrix for creep rupture tests on Al-BS specimens

Temperature (°C)	Nominal humidity (%RH)	Nominal shear stress (MPa)	Number of replicates
30	75	0.71	6
		0.61	6
		0.52	6
50	25	0.64	6
		0.53	6
		0.41	6
86	6	0.47	6
		0.41	6
		0.32	6

5.3 Results and Discussion

5.3.1 DMA tests

Initially, in order to determine the linear viscoelastic region of the sealants used in this study, dynamic mechanical properties were characterized as a function of applied dynamic strain at 1Hz and 30°C. Figure 5-6 shows the variation of dynamic mechanical properties as a function of dynamic strain for loading part of the three successive strain sweeps for sealant B.

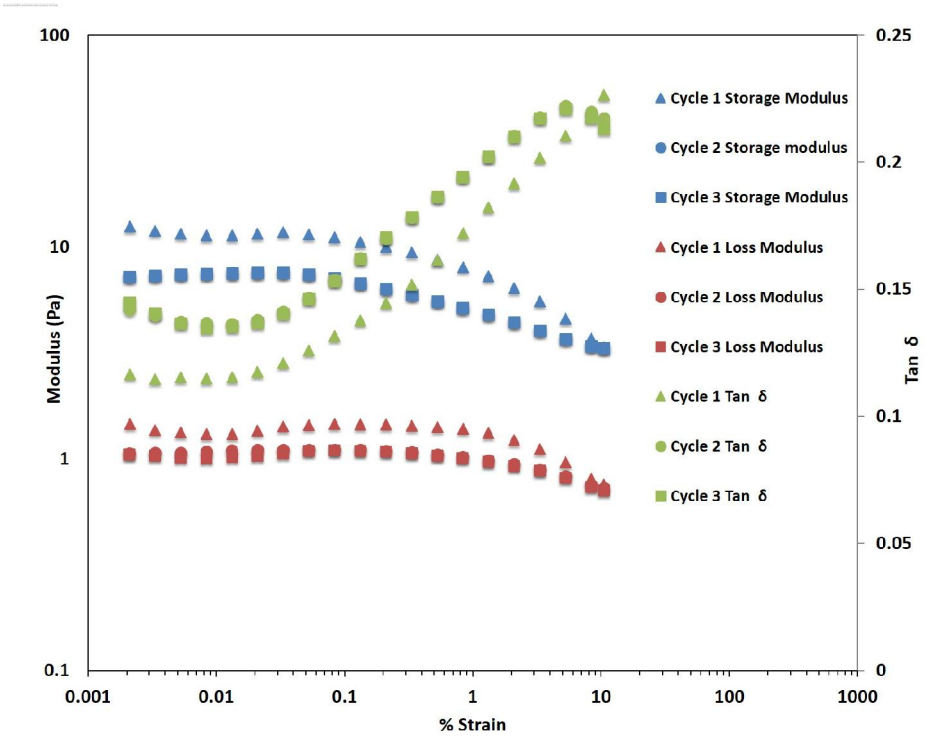

Figure 5-6: Variation of dynamic mechanical properties of sealant B as a function of % strain for 3 successive strain sweeps

It was observed that for all strain sweeps, storage and loss moduli remained reasonably constant up to about 0.1% strain. For strains greater than about 0.1%, moduli decreased with increasing strain up to 10%. Moduli values for the second strain sweep were lower than moduli obtained during first strain sweep at corresponding strains. No further drop was observed for the third strain sweep. In light of trends observed during dynamic strain sweeps, 0.05 % strain was chosen as the amplitude for conducting DMA tests involving frequency sweeps at various temperatures. A decrease in modulus over

successive strain sweeps for filled silicone sealants and other elastomeric polymers has been reported previously. This phenomenon is commonly referred to as Payne's effect [17]. Similar trends were observed during ramp loading studies on these materials, where the onset of decreasing modulus during successive ramps was observed at strains less than 1%. These trends during ramp loading are commonly referred as the Mullin's effect [18]. Nonetheless, such trends are typically observed at much higher strains than at strains observed for sealants in this study [19-21].

DMA tests were carried out to generate master curves of storage and loss moduli. These tests involved frequency sweeps at several successive temperatures 10°C apart starting at a low temperature. These master curves and associated thermal shift factors based on constitutive properties will be used in the generation of creep rupture master curves from creep rupture data. In a similar study on acrylic and silicone based sealants for structural glazing applications, it was observed that creep rupture data for several silicone sealants at given applied stress levels showed significant scatter and spread on log(time to fail) axis [10]. Due to suspected scatter in the creep rupture test data, thermal shift factors obtained from small strain DMA studies might provide a relevant basis to shift creep rupture data and to generate master curves, once the applicability of small strain test shift factors to generate master curves for data from large strain tests is verified [9, 10].

In order to obtain thermal shift factors at desired temperatures, master curves were generated using TTSP [22] and the data obtained from the multifrequency/temperature step DMA tests for sealant B specimens. Master curves were generated at 30°C as a reference temperature. The basic principle behind time temperature superposition is the direct equivalency between time (the time-scale of measurement) and temperature for polymeric and other amorphous materials. In other words, changes in temperatures are equivalent to shifts along logarithmic frequency or time-scales. Thus experiments can be conducted at higher and lower temperatures at experimentally accessible time-scales and data can then be shifted horizontally along the frequency or time axis to obtain material properties over very large time scales or very short time scales, respectively. The data was also shifted vertically according to the

following equation [22]

$$b_T = \frac{\rho T}{\rho_0 T_0}$$

where ρ is the density of material at absolute temperature T (Kelvin scale) and ρ_0 is the density of the material at the reference temperature T_0 (K). The density ratio was assumed to be unity since specimen dimensions were always recorded at room temperature prior to testing and relative contributions by thermal expansion would relatively smaller compared to entropic contributions. Based on the theory of rubber elasticity, which states that the modulus is proportional to the absolute temperature at which the elastomer is tested, the above vertical shift factor serves as a correction factor for the modulus [22-24].

The first step during generation of master curves for constitutive data from small strain DMA tests was to plot the raw data consisting of a series of frequency sweeps performed at various temperatures. This data was then shifted manually by adding or subtracting a shift factor from log (frequency) values to align all the frequency sweeps in a single smooth master curve. Lower temperature data was shifted to simulate high frequency tests while higher temperature data was shifted to simulate low frequency tests. The reference temperature was set to 30°C. The resulting storage and loss moduli and tan δ master curves are shown in Figure 5-7, Figure 5-8 and Figure 5-9, respectively.

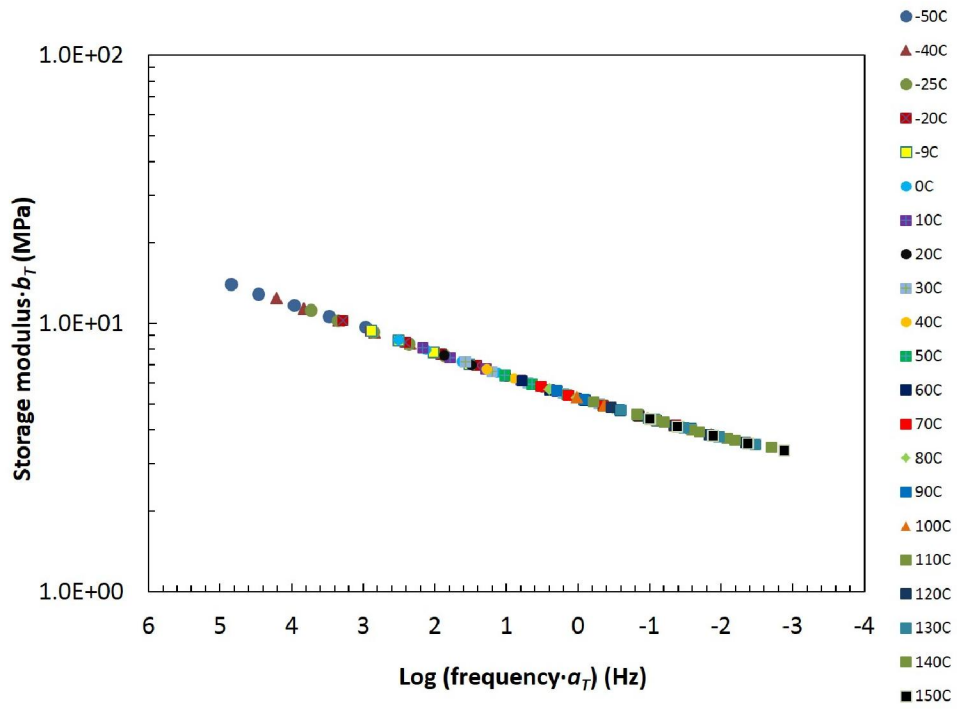

Figure 5-7: Storage modulus master curves for sealant B obtained via manual shifting with 30°C as the reference temperature

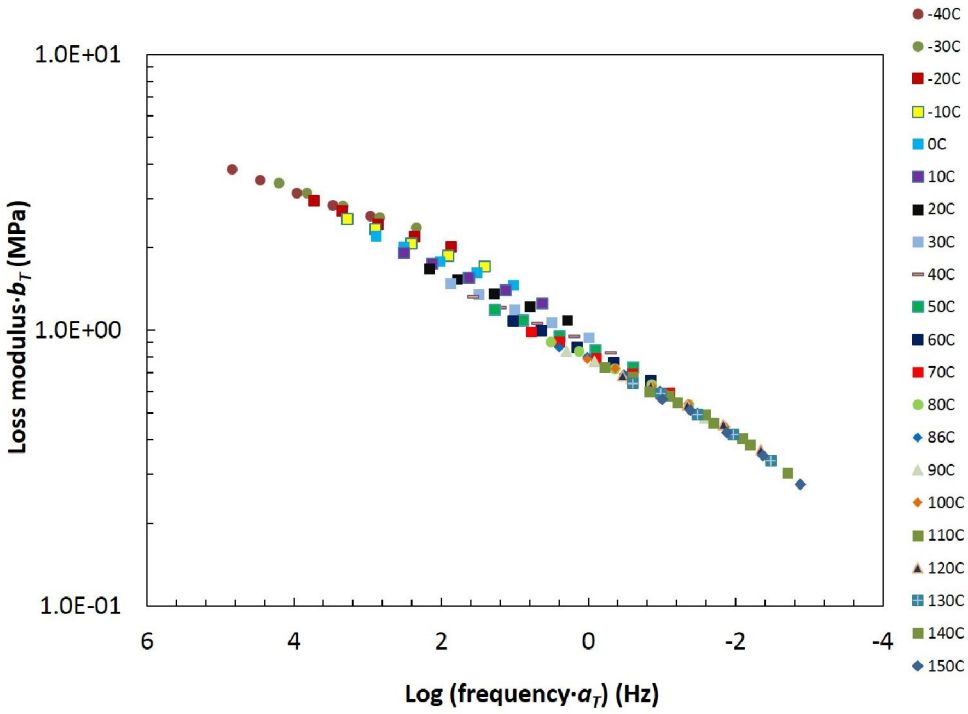

Figure 5-8: Loss modulus master curve for sealant B at 30°C as the reference temperature obtained using shift factors from manually shifted storage modulus master curve in Figure 5-7

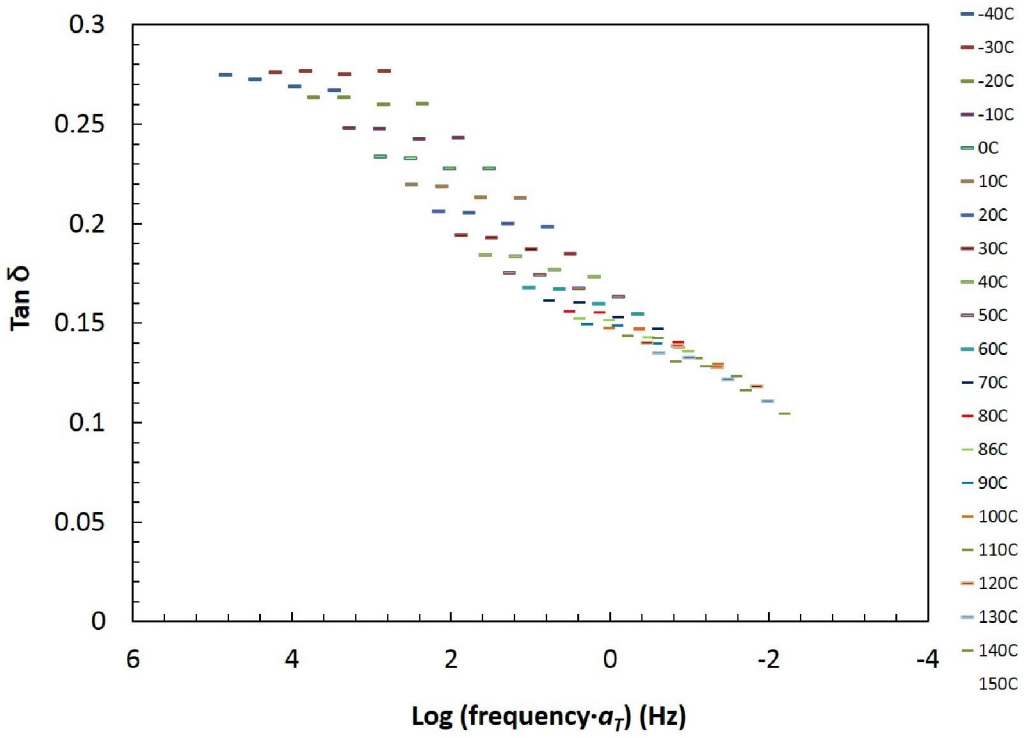

Figure 5-9: Tan δ master curve for sealant B at 30°C as the reference temperature obtained using shift factors from manually shifted storage modulus master curve in Figure 5-7

By applying manual shifts, a smooth storage modulus master curve was obtained but use of the same shift factors did not lead to smooth loss modulus and tan delta master curves. For loss modulus master curves slight deviation was observed in the range of -10°C to 40°C.The glass transition temperature for the sealants used in this study was around -120°C. The DMA data was collected from -50°C to 150°C, while temperatures used in creep rupture tests (30°C, 50°C and 86°C) at which relevant shift factors were desired were at least 100°C above the glass transition temperature (T_g) thus shift factors obtained from manually shifted storage modulus master curves were fit using the Arrhenius equation as Williams-Landel-Ferry (WLF) equation is typically valid for temperature range of 100°C above the T_g [22].

$$\log a_T = \frac{E_a}{R}\left(\frac{1}{T} - \frac{1}{T_{ref}}\right)$$

where E_a is the activation energy, R is the universal gas constant, T is an absolute

temperature and T_{ref} is the reference temperature. Figure 5-10 shows both the manual shift factors and the resulting Arrhenius best-fit curve at reference temperature of 30°C. Figure 5-10 reveals that shift factors obtained using manual shifts follow an Arrhenius type behavior with temperature. The slope of the straight line fit allows us to estimate the activation energy, which was calculated as 56.66 KJ/mol.

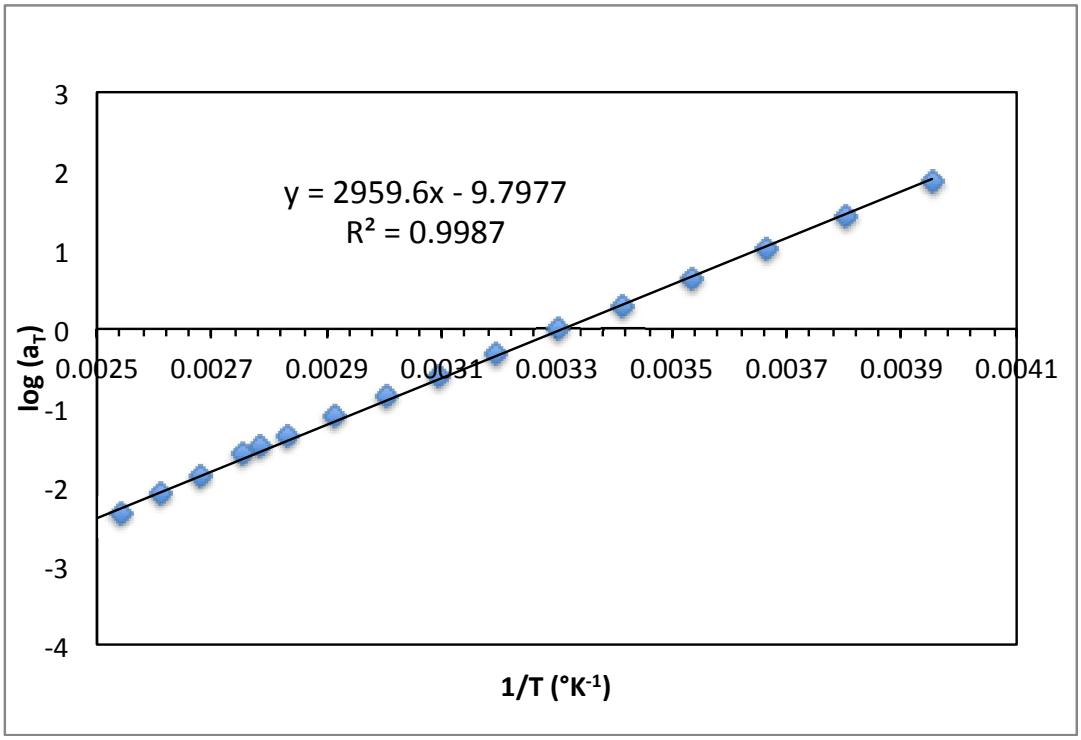

Figure 5-10: Sealant B shift factors from manually shifted storage modulus using 30°C as the reference temperature and least square fit using Arrhenious equation

5.3.2 Ramp to fail tests

Representative plots of nominal stress vs. crosshead displacement data from ramp to fail tests are included in Figure 5-11. From Figure 5-11 it was observed that except for the set of specimens tested at -10°C and at 0.00328 sec^{-1} strain rate, all other specimens showed a sudden drop in stress upon reaching the maximum stress. At -10°C and at 0.00328 sec^{-1} strain rate, after the maximum stress was reached, specimens continued to provide a lesser degree of load resistance until the complete failure occurred. At -10°C, such behavior was not observed for tests carried out at other strain rates and a sudden drop in stress was observed after reaching the maximum stress.

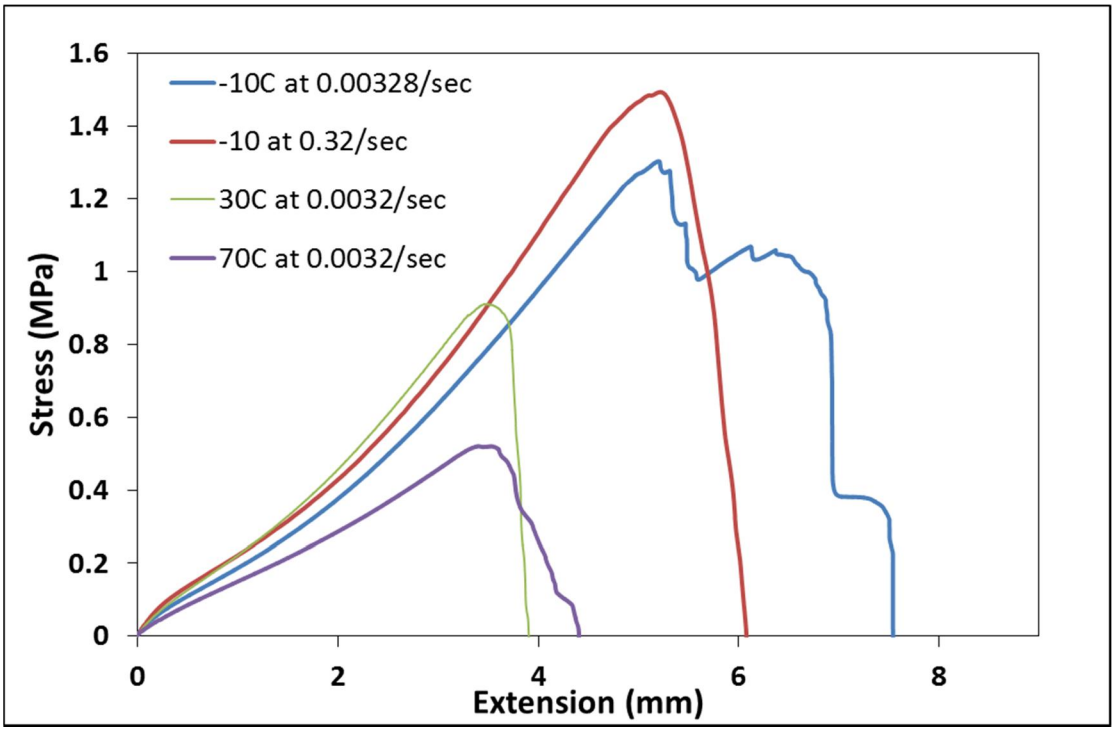

Figure 5-11: Representative sealant C nominal stress vs. extension data from ramp to fail tests

Figure 5-12 shows failure surfaces of representative specimens tested at 70°C at all four strain rates. All specimens exhibited cohesive failures within the sealants with a post failure analysis showing combination of failure striations across the width of the specimen and bulk tearing failure modes.

Figure 5-12: Representative failure surfaces of specimens from ramp to fail tests at 70°C and 3.2 s^{-1}, 0.32 s^{-1}, 0.032 s^{-1}, 0.0032 s^{-1} strain rates (from left to right) on sealant C

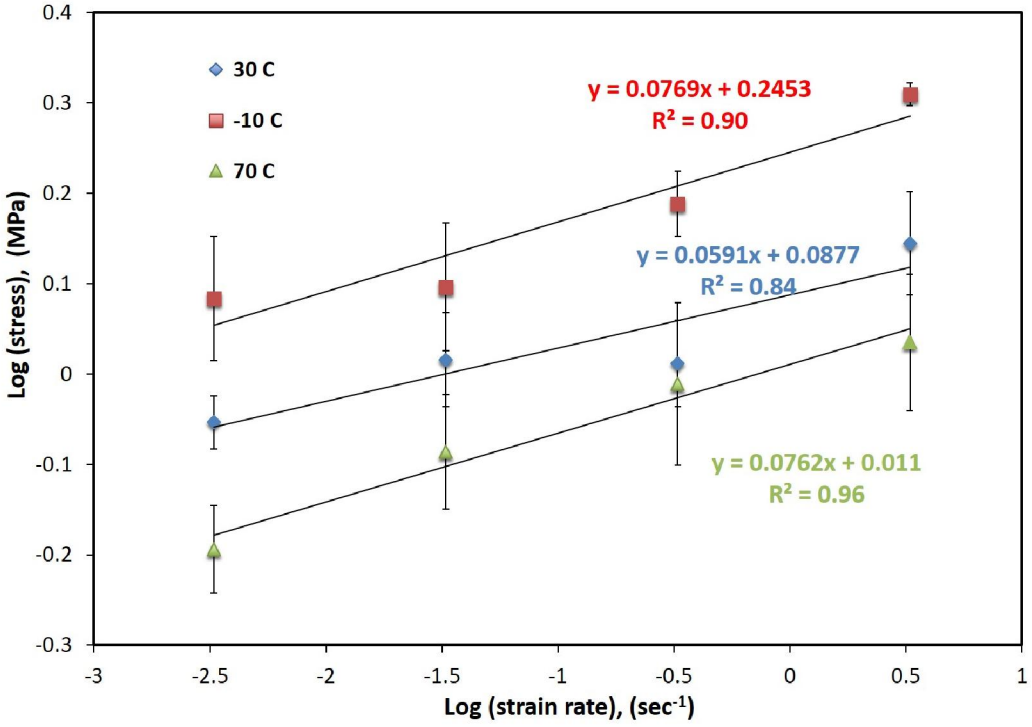

Figure 5-13: Ultimate nominal shear strength of sealant C as a function of strain rates at various temperature

Figure 5-13 shows the ultimate nominal shear strength of silicone C sealant as a function of strain rate at various temperatures plotted on a log-log scale. Each data point on the graph represents an average value obtained from 3 replicate specimens. Error bars represent +/- one standard deviation. It was observed that the ultimate shear strength increased with increasing strain rate. On the log-log scale the data suggested a linear relationship between ultimate shear strength and strain rate. This linear relationship on the log-log scale corresponds to a power law relation of the form

$$\sigma_u = A \cdot \dot{\gamma}^n$$

where, σ_u is ultimate nominal shear strength and $\dot{\gamma}$ is nominal axial strain rate [9, 10]. The TTSP thermal shift factors generated from DMA tests were then applied to the ramp fail data gathered at various temperatures, leading to a ramp to fail master curve shown in Figure 5-14.

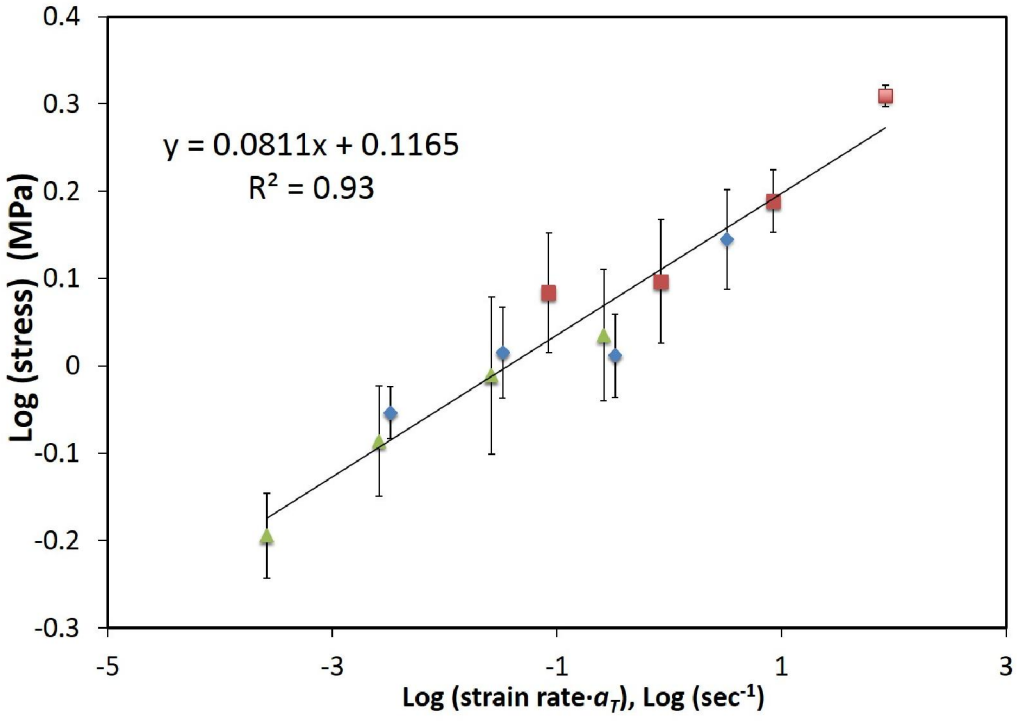

Figure 5-14: Ramp to fail master curve at 30°C as the reference temperature generated using shift factors obtained using DMA tests data

The shifted ramp to fail data was fitted with a least square regression line resulting in a power law relationship at 30°C as a reference temperature with stress in MPa and strain rate in s^{-1}[9]

$$\sigma_u = 0.1165 \cdot \dot{\gamma}^{0.0811}$$

A regression fit of the above equation to the shifted log (strain rate) data resulted in an R^2 value of 0.93. Ramp to fail data was then shifted manually with 30°C as the reference temperature to generate a smooth master curve such that manual shifting maximized the R^2 value. Shift factors obtained from manual shifts will then be compared with shift factors based on DMA tests. Figure 5-15 shows the manually shifted ramp to fail master curve. The manually shifted ramp to fail data was fit with a least square regression line resulting in a relationship at 30°C between stress in MPa and strain rate in s^{-1}

$$\sigma_u = 0.0992 \cdot \dot{\gamma}^{0.0707}$$

The regression fit of above equation to manually shifted log (strain rate) data resulted in R^2 value of 0.95.

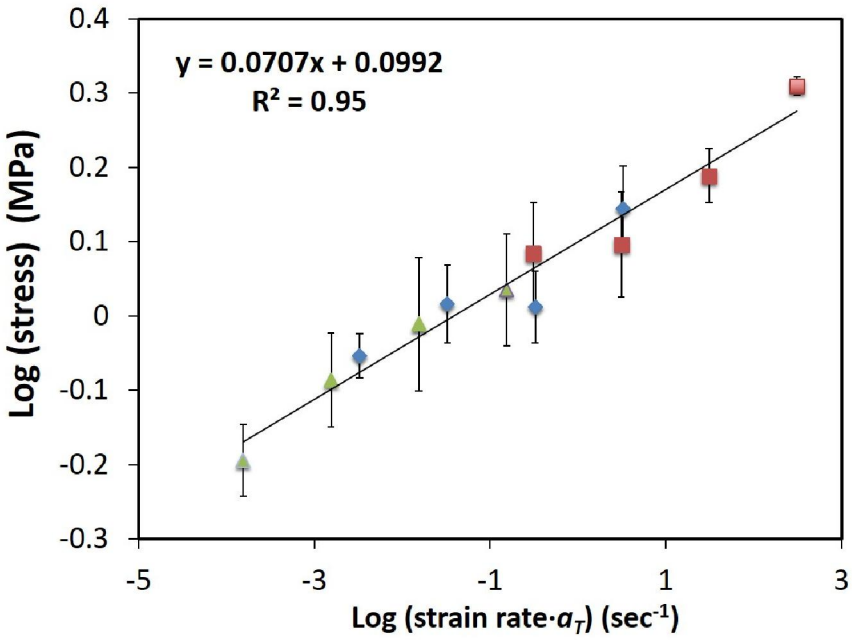

Figure 5-15: Ramp to fail master curve at 30°C as the reference temperature generated using manually generated shift factors

Table 5-3 compares shift factors obtained from DMA tests, which are small strain constitutive tests with the shift factors obtained from manual shifting of the ramp to fail data.

Table 5-3: Comparison of shift factors obtained using DMA tests and shift factors from manual shifting of ramp to fail data

Temperature (°C)	Shift Factors	
	DMA tests	Manual shifts
-10	1.41	1.97
30	0	0
70	-1.1	-1.32

Table 5-4: Comparison of power law fits to the ramp to fail master curves obtained using shift factors from DMA tests and shift factors from ramp to fail tests

	A	n	R^2
Using shift factors from DMA tests	0.1165	0.0811	0.93
Using shift factors from manual shifts	0.0992	0.0707	0.95

Table 5-4 compares power law fitting parameters for ramp to fail master curves obtained using shift factors from DMA tests and shift factors from manual shifts. It was observed that the manual shift factors, the shift factors from small strain DMA experiments, and slopes of regression line fit values were in reasonable agreement with each other. Considering the experimental variations inherent with the large strain ramp to fail test, a close agreement between shift factors from DMA and failure tests (ramp to fail), hints towards similar underlying molecular mechanisms for small strain constitutive properties and during failures in large strain ramp to fail tests.

5.3.3 Creep rupture tests

Figure 5-16 shows creep rupture failure times for Al-Al type specimens of silicone sealants A, B, C. It was observed that for few temperature-stress combinations, some specimens failed within 4 seconds upon application of stress. During creep rupture tests, it is difficult to apply a perfect unit step stress profile. This complicates acquiring reliable creep rupture data, so failures prior to several times the rising load profile may not represent (should be considered) the valid creep rupture times, though these failures do suggest the weakness of the specimens. As the specimens were loaded by opening the pressure values, it was observed that it took about two to three seconds for pneumatic cylinders to fully pressurize and reach the applied stress level. Thus, failures prior to 10 sec were considered anomalous and were not considered during the analysis. If the shift factors obtained from DMA tests are applied to the data from creep rupture tests, the data aligns into master curves as shown in Figure 5-17 to Figure 5-22.

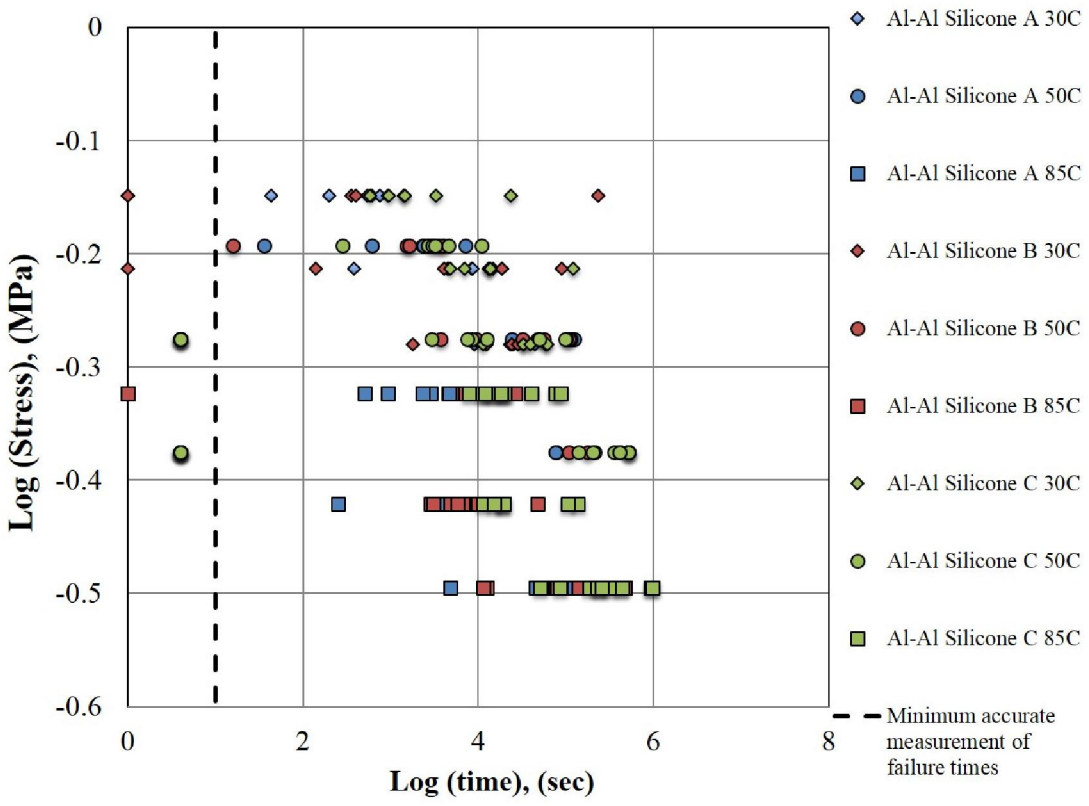

Figure 5-16: Creep rupture data obtained from Al-Al specimens

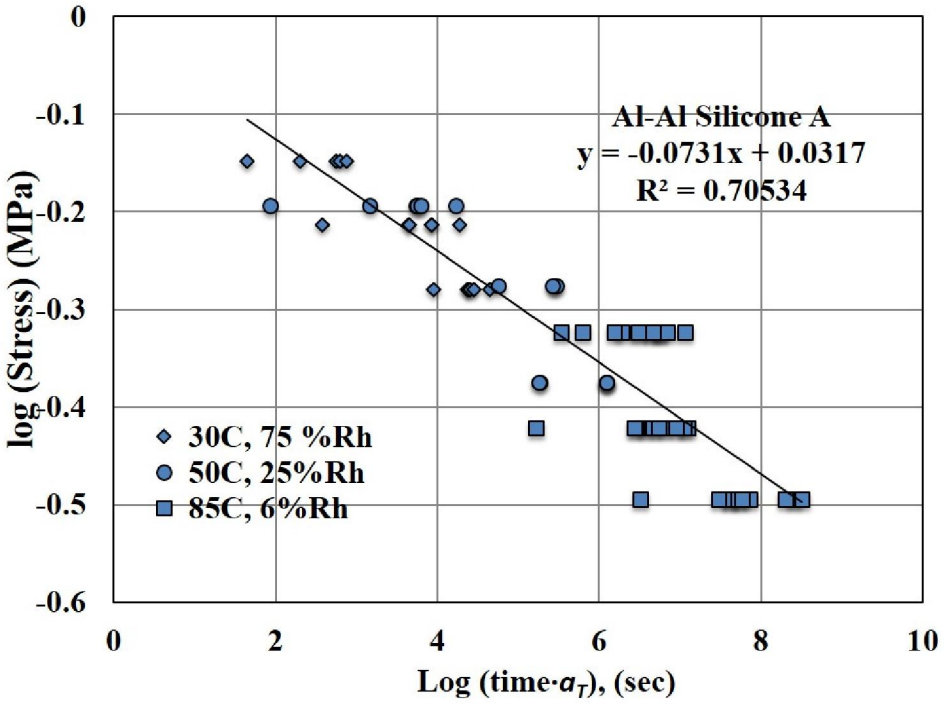

Figure 5-17: Creep rupture master curve for Al-Al silicone A specimens at 30°C as the reference temperature generated using DMA shift factors

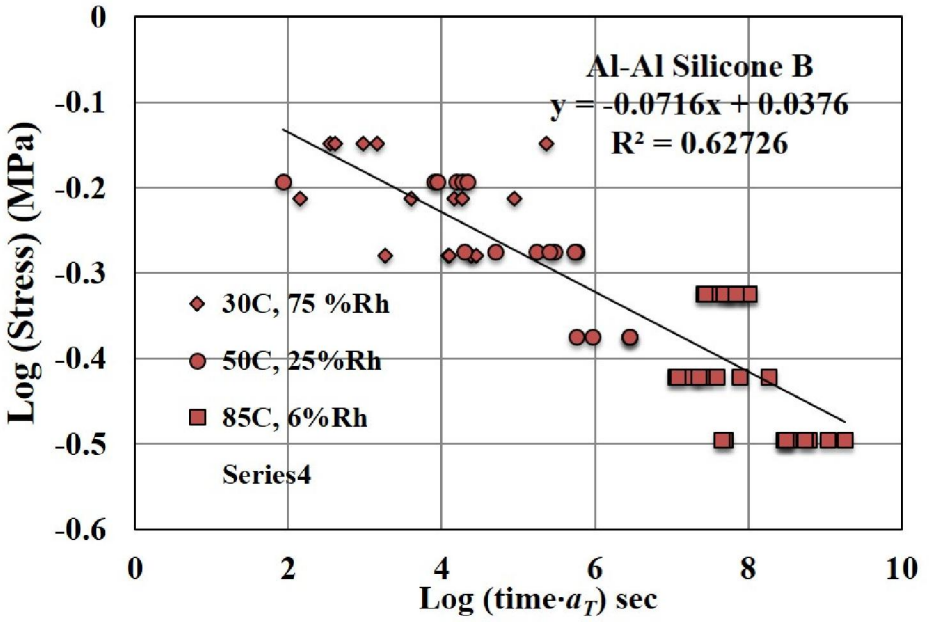

Figure 5-18: Creep rupture master curve for Al-Al silicone B specimens at 30°C as the reference temperature generated using DMA shift factors

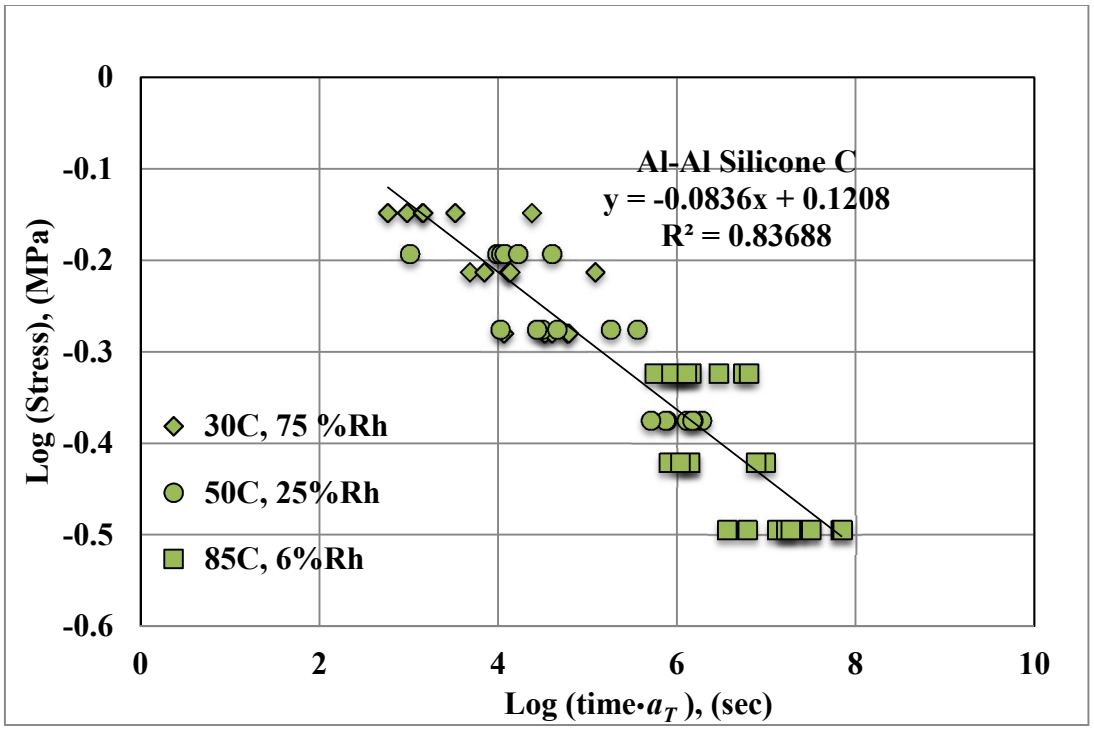

Figure 5-19: Creep rupture master curve for Al-Al silicone C specimens at 30°C as the reference temperature generated using DMA shift factors

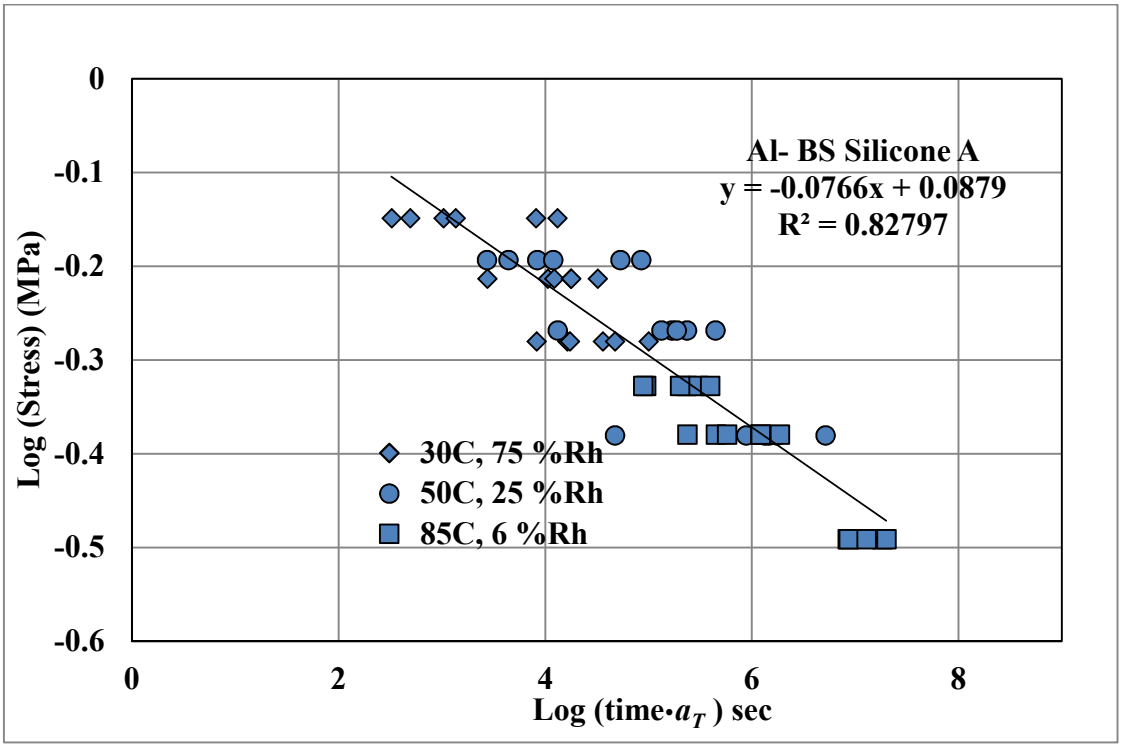

Figure 5-20: Creep rupture master curve for Al-BS silicone C specimens at 30°C as the reference temperature generated using DMA shift factors

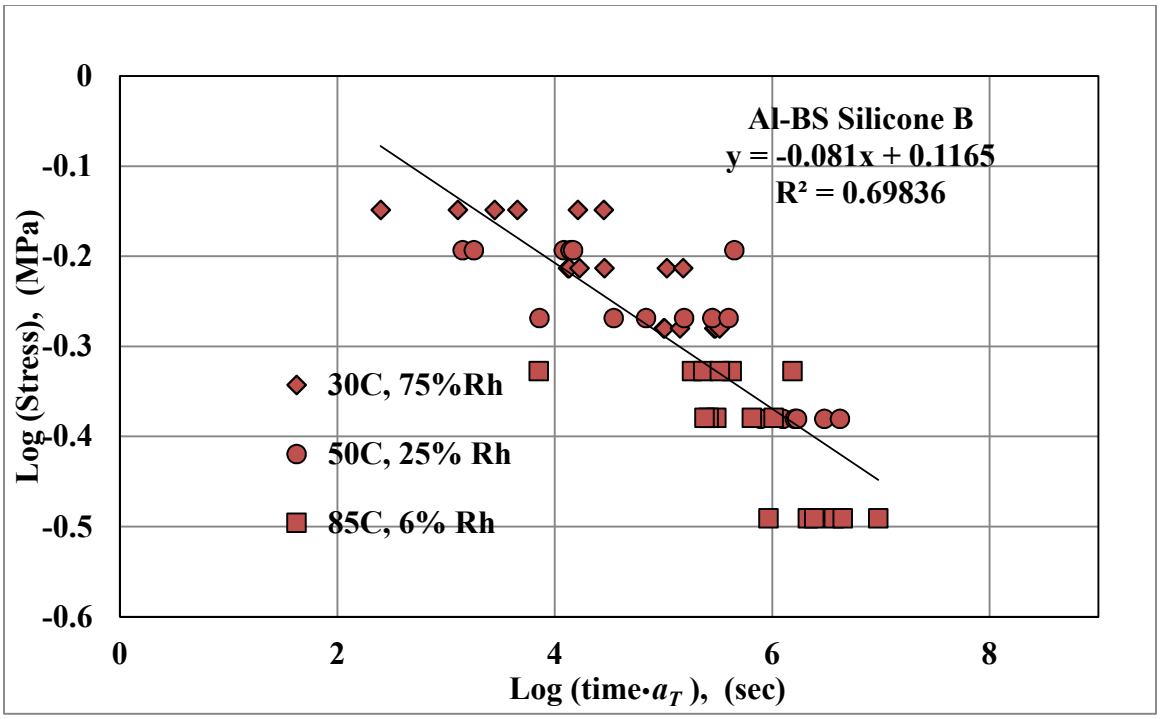

Figure 5-21: Creep rupture master curve for Al-BS silicone B specimens at 30°C as the reference temperature generated using DMA shift factors

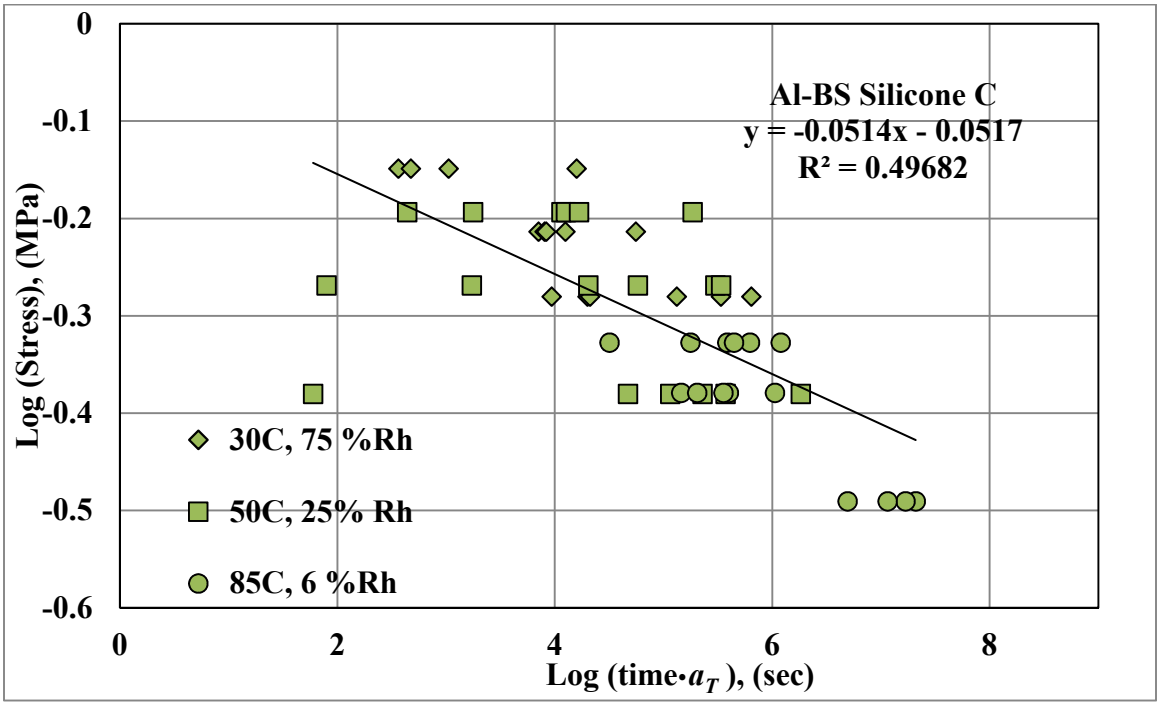

Figure 5-22: Creep rupture master curve for Al-BS silicone C specimens at 30°C as the reference temperature generated using DMA shift factors

As shown in Figure 5-17 to Figure 5-22, creep rupture data was plotted as

log(stress) vs log(failure time) and the data was fitted with a linear relationship [10]. This linear relationship on a log-log scale corresponds to the power law relationship for 30°C as the reference temperature of the form,

$$\sigma_{creep} = C \cdot t_{fail}^{\ m}$$

where σ_{creep} is applied stress and t_{fail} is failure time.

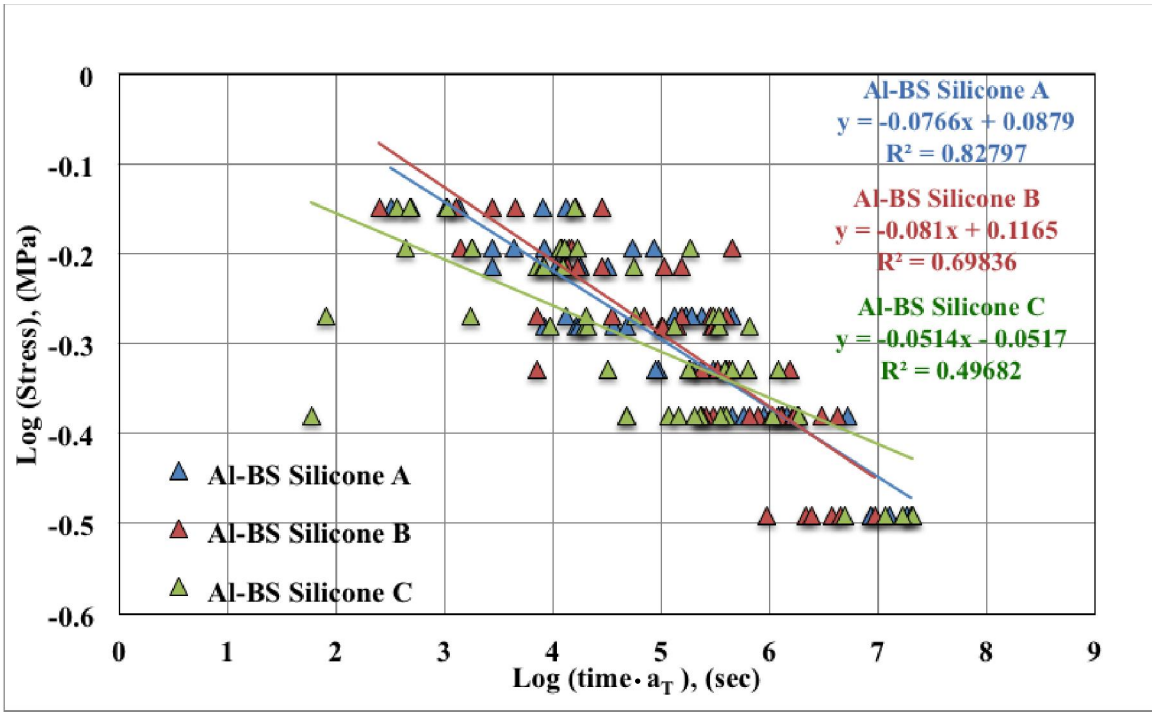

Figure 5-23: Comparison of creep rupture master curves of Al-Al specimens of silicone A, B and C at 30°C as the reference temperature.

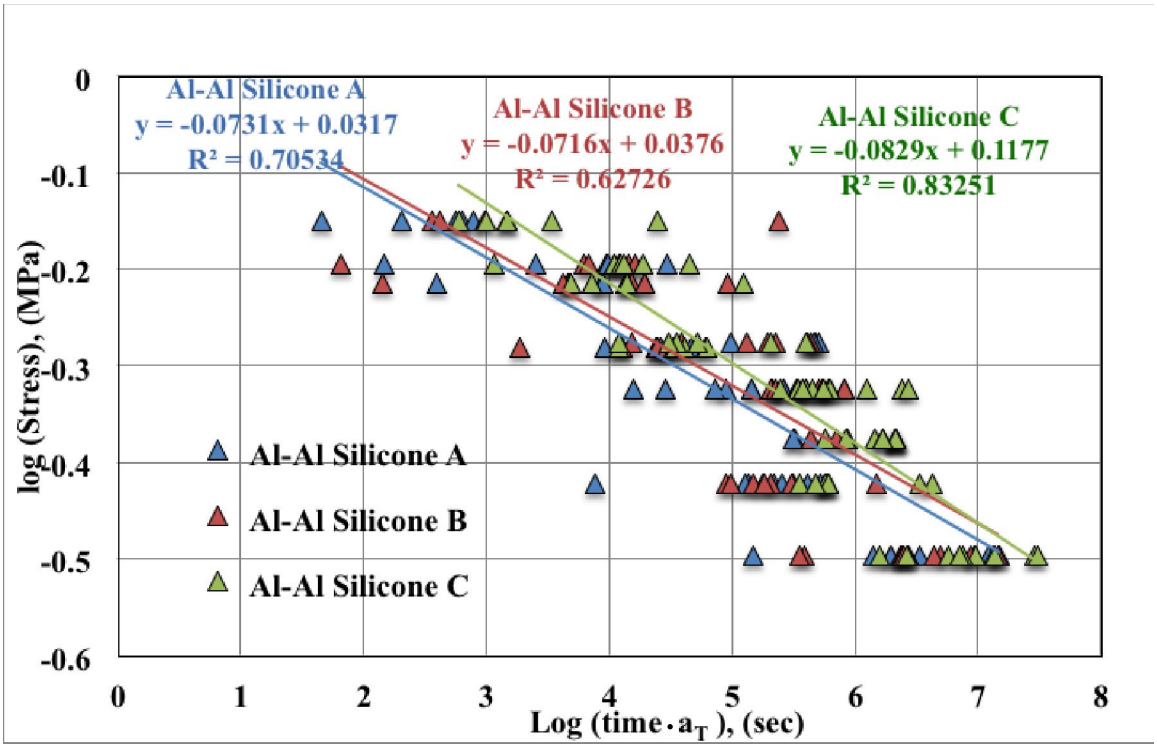

Figure 5-24: Comparison of creep rupture master curves for Al-BS specimens of silicone A, B and C at 30°C as the reference temperature

Table 5-5: Comparisons of fitting parameters of the regression fits to the three silicones creep rupture results

Silicone type	Specimen type	*m*	*C*	R^2	Predicted failure stress at 30 years, (MPa)
Silicone A	Al-Al	-0.073	0.031	0.70	1.01
	Al-BS	-0.076	0.087	0.82	1.04
Silicone B	Al-Al	-0.071	0.037	0.62	1.01
	Al-BS	-0.081	0.698	0.69	1.35
Silicone C	Al-Al	-0.082	0.117	0.83	1.05
	Al-BS	-0.05	0.496	0.49	1.50

Figure 5-23, Figure 5-24 and Table 5-5 show comparisons between creep rupture master curves for the three silicones studied using Al-Al and Al-BS type specimens and fitting parameters for the regression fits. It was observed that in light of the scatter in the data all the sealant showed similar creep rupture performance. One of the interesting aspects of creep rupture, ramp to fail and small strain DMA constitutive test data was similarity of absolute slopes of the master curves. It was observed that master curves from all these tests showed similar slopes around 0.07, suggesting a constant strain to failure criteria.

At most of the stress levels data from creep rupture tests showed about a decade and half of scatter, though in some cases larger scatter was observed. Similar scatter has been observed during creep rupture tests on silicone sealants used for structural glazing applications [7]. As mentioned previously, all the specimens prepared during this study were cured under highly controlled conditions in terms of humidity and temperatures. The test parameters such as temperature and humidity were highly controlled and measured as well. In an attempt to find a rationale behind the scatter in the creep rupture data, failure patterns of creep rupture tests specimens at all test conditions were studied. During this study specimens tested at a given condition of stress level, humidity and temperature combination were laid out in the order of increasing failure times. Failure surfaces were then observed with the aim of finding a conclusive, non-subjective correlation between failure times and a particular failure pattern that would be applicable across all the specimens. During the detailed study of the failure patterns of specimens (based on visual observations), no relevant and conclusive correlation was found between a particular failure pattern and the measured failure times. Figure 5-25 and Figure 5-26 show typical failure patterns observed during creep rupture tests. Before conducting creep rupture tests the bondline thickness of the specimens was measured for all the test specimens. Upon comparing the bondline thickness variations with failure times no correlation was observed between bondline thickness and time to failure that could lead to scatter in the time to failure data.

Figure 5-25: Representative failure surfaces of Al-Al specimens from creep rupture tests at 30°C and middle stress level (0.61 MPa)

Figure 5-26: Representative failure surfaces of Al-BS specimens from creep rupture tests at 30°C and middle stress level (0.61 MPa)

Similar scatter has been observed in the creep rupture data for silicone sealants used for structural glazing type applications [7, 16]. In a similar study reported on the creep rupture performance of acrylic foam based VHB tapes, the creep rupture slopes of acrylic foam tapes, were considerably steeper than the creep rupture slopes of silicone based sealants used in this study [9, 10]. Also it was observed that the scatter in the data from acrylic foam tapes was considerably lower than that of the silicone sealants. In light of well controlled specimen preparation procedure and test conditions, one of the possible reasons behind the observed scatter in the data might be low slope values, where small perturbations in applied stress levels can lead to large variations in failure times [25].

In light of the scatter in the creep rupture data, the slopes of the master curves for all the sealants and geometries appear to be very similar. If we consider 30 years as the design life of a structural sealant joint, the data from Table 5-5 indicates that the nominal failure stress for lap shear geometry of all sealants joints lies slightly above 1 MPa. From the creep rupture data it can be observed that several specimens failed decades before the prediction shown by power law relationships. Moreover these tests where carried out in controlled laboratory environment. Significant scatter in the data obtained in controlled laboratory conditions suggests the likelihood of even more variations in failure stress when the joints are assembled in field conditions and subjected to real service conditions. The loading conditions used in this study are representative of dead load type situation, a load that would come about due to weight of the module itself. Fatigue stresses induced due to wind loading, periodic snow loading per year basis and temperature changes during the day and throughout the year would be an important aspect to consider as well. Also in this study, tests were carried out in lap shear configuration, a placement of solar panels at an angle with overhangs about supporting rail structure would lead to high peel stresses due to wind gusts and dead load type situations. These peel stresses could significantly affect the creep rupture performance. Thus data from these tests is more relevant in terms of comparisons and discrimination between the three sealants used in this study. Nevertheless, as mentioned earlier in ever shortening product development cycles, the test approach outlined in this study could offer valuable insights in discriminating the long-term performance of the new sealant families.

5.4 Conclusions

This study was aimed at obtaining insights and comparing the long term creep rupture performance of three different silicone-based sealants for load bearing applications such as solar panel support application or structural glazing application. Using a 72-station pneumatic creep frame, a total of 134 specimens involving three different silicone sealants were tested at three temperature and humidity pairs. In addition to the creep rupture tests, ramp to fail tests were performed on specimens fabricated with one of the sealants at three rates of strain and at three temperatures, totaling 36 specimens. Using the TTSP, thermal shift factors were obtained from dynamic mechanical analysis. The thermal shift factors obtained from dynamic small strain constitutive tests were used to form reasonable master curves for the data from ramp to fail and creep rupture tests. Thermal shifting led to simulation of creep rupture failure times up to three years based on the tests performed in one month. Creep rupture and ramp to fail master curves, when plotted on log-log scales, resulted in linear relationships between time to fail or crosshead rate, respectively, and applied or breaking stress, respectively. Also, master curves from constitutive DMA, ramp to fail, and creep rupture tests showed similar slopes, thus suggesting a constant strain to failure criterion. Data obtained from creep rupture tests in particular showed significant scatter, though not unusual for creep rupture results. In light of the scatter observed in the data, the creep rupture data from three sealants appeared to be indistinguishable. Small slopes of the master curves for all the sealants indicated a very small time dependence of failure times for silicone sealants used in this study, which significantly contributes to the observed scatter in the creep rupture data. Due to the scatter observed in the creep rupture tests data, long-term verification testing is recommended for better insights into the accuracy of the predicted master curves.

5.5 References

[1] E. M. Petrie, *Handbook of Adhesives and Sealants*: McGraw-Hill New York, 2000.

[2] F. de Buyl, "Silicone Sealants and Structural Adhesives," *International Journal of Adhesion and Adhesives,* **21**, 411-422, 2001.

[3] W. Noll, *Chemistry and Technology of Silicones*: Elsevier, 1968.

[4] M. J. Owen, "The Surface Activity of Silicones: A Short Review," *Industrial &*

Engineering Chemistry Product Research and Development, **19**, 97-103, 1980.
[5] A. T. Wolf, *Durability of Building Sealants: State-of-the-art Report of RILEM Technical Committee 139-DBS, Durability of Building Sealants* vol. 21: RILEM publications, 1999.
[6] J. Iker and A. Wolf, "Secondary Stresses Induced by Shear Movement in Structural Glazing Sealants," *Materials and Structures,* **25**, 137-144, 1992.
[7] L. B. Sandberg and A. E. Rintala, "Resistance of Structural Silicones to Creep Rupture and Fatigue," *Building Sealants: Materials, Properties, and Performance,* **1069**, 7, 1990.
[8] A. T. Wolf, *3rd International Symposium on Durability of Building and Construction Sealants : Seneffe, Belgium, February 2 - 3, 2000*. Cachan, France: RILEM Publications, 2000.
[9] B. W. Townsend, D. C. Ohanehi, D. A. Dillard, S. R. Austin, F. Salmon, and D. R. Gagnon, "Characterizing Acrylic Foam Pressure Sensitive Adhesive Tapes for Structural Glazing Applications—Part I: DMA And Ramp-To-Fail Results," *International Journal of Adhesion and Adhesives,* **31**, 639-649, 2011.
[10] B. W. Townsend, D. C. Ohanehi, D. A. Dillard, S. R. Austin, F. Salmon, and D. R. Gagnon, "Characterizing Acrylic Foam Pressure Sensitive Adhesive Tapes for Structural Glazing Applications—Part Ii: Creep Rupture Results," *International Journal of Adhesion and Adhesives,* **31**, 650-659, 2011.
[11] H. Stögbauer and A. T. Wolf, "The Influence of Heat Ageing on One-Part Construction Silicone Sealants," *Construction and Building Materials,* **5**, 27-32, 1991.
[12] E. D. Bull, E. D. Bull, and G. M. Lucas, "Long-Term Outdoor Weathering Study of Construction Sealants," *Journal of ASTM International,* **1514**, 38-72, 2008.
[13] A. T. Wolf, "Effects of Water Immersion on Building and Civil Engineering Joints and the Use of the Arrhenius Method in Predicting Adhesion Lifetime of Water-Immersed Joints," *Journal of ASTM International,* **5**, 2008.
[14] B. Müller and R. Walter, *Formulating Adhesives and Sealants: Chemistry, Physics and Applications*. Hannover: Vincentz Network, 2010.
[15] A. V. Pocius, D. A. Dillard, and M. K. Chaudhury, *Adhesion Science and Engineering* vol. 2. Amsterdam; Boston: Elsevier, 2002.
[16] B. W. Townsend, "Characterization and Lifetime Performance Modeling of Acrylic Foam Tape for Structural Glazing Applications," Masters, Virginia Polytechnic Institute and State University, Blacksburg, VA, USA, 2008.
[17] L. Chazeau, J. D. Brown, L. C. Yanyo, and S. S. Sternstein, "Modulus Recovery Kinetics and Other Insights into the Payne Effect for Filled Elastomers," *Polymer Composites,* **21**, 202-222, 2000.
[18] A. Maiti, W. Small, R. H. Gee, T. H. Weisgraber, S. C. Chinn, T. S. Wilson*, et al.*, "Mullins Effect in a Filled Elastomer Under Uniaxial Tension," *Physical Review E,* **89**, 012602, 2014.
[19] L. Yan, D. A. Dillard, R. L. West, L. D. Lower, and G. V. Gordon, "Mullins effect recovery of a nanoparticle-filled polymer," *Journal of Polymer Science Part B: Polymer Physics,* **48**, 2207-2214, 2010.
[20] L. Yan, D. A. Dillard, R. L. West, K. J. Rubis, and G. V. Gordon, "Strain rate and temperature dependence of a nanoparticle-filled poly(dimethylsiloxane)

undergoing shear deformation," *Journal of Polymer Science Part B: Polymer Physics,* **50**, 929-937, 2012.
[21] J. Diani, B. Fayolle, and P. Gilormini, "A review on the Mullins effect," *European Polymer Journal,* **45**, 601-612, 3// 2009.
[22] J. D. Ferry, *Viscoelastic Properties of Polymers* vol. 3: Wiley New York, 1980.
[23] H. F. Brinson and L. C. Brinson, *Polymer Engineering Science and Viscoelasticity: An Introduction*: Springer, 2008.
[24] I. M. Ward and J. Sweeney, *An Introduction to the Mechanical Properties of Solid Polymers*: Wiley. com, 2005.
[25] W. Nelson, *Accelerated Testing: Statistical Models, Test Plans and Data Analyses*. New York: Wiley, 1990.

6 Summary and Conclusions

In this thesis four test approaches were developed to characterize the adhesion performance and durability of adhesive bonds. These approaches, which were not directly related to one another, were developed for specific applications in a broad range of adhesion science areas, spanning structural adhesive joints to confectionaries such as sticky chewed gum cuds. Apart from exposure to multiple adhesion science areas, working on these projects has given me an opportunity to interact with collaborators with a wide range of scientific expertise. During these projects, one of the valuable skills that I have gained is quickly addressing research challenges that are outside my past research experience and obtain valuable scientific insights. This skill would be highly useful as I enter the world of industrial research.

The following sections summarize the conclusions and potential future research avenues for each test approach developed during this thesis:

Chapter I: A Tapered Bondline Thickness Double Cantilever Beam (DCB) Specimen Geometry for Combinatorial Fracture Studies of Adhesive Bonds

This study proposed and demonstrated the use of a DCB specimen with a linearly varying bondline thickness as a potential combinatorial specimen for characterizing the effect of bondline thickness on fracture energy. For the adhesive system used in this study data from linearly increasing and linearly decreasing bondline thickness specimens generally showed good agreement with that from constant bondline thickness specimens. It was observed that a single DCB specimen with a linearly increasing or linearly decreasing bondline thickness could provide significant insight into the effect of the fracture energy on the bondline thickness. This will result in a decrease in the testing time and effort needed to study the effect of the bondline thickness on the fracture energy of a toughened epoxy adhesive system. Concerns would be raised, however, if the bonds exhibit a clear R-curve behavior, which could obscure the results of this combinatorial specimen configuration.

In this study the tests were performed using an epoxy-based structural adhesive,

exploring the applicability of this method for other adhesive systems, such as acrylate and urethane-based structural adhesives, would be interesting. Another future direction could be towards developing a tapered bondline joint geometry envelope that would serve as a guiding map, for applicability of tapered bondline DCB joint configurations in characterizing the effect of bondline thickness on the fracture energy of adhesive joints.

Chapter II: Fracture performance and the interaction of a propagating crack with locally weakened interfaces in an adhesive joint

In this study a technique is reported for creating well-defined and quantifiable localized weak interfaces on base-acid treated aluminum adherends using physical vapor deposition of copper. By using this technique to create several systematic patterns, the effect of the presence of localized interface defects on the performance of structural epoxy adhesive bonds was studied. Under mode I loading conditions, the presence of localized weak interfaces influenced the fracture energy of a propagating debond over a considerable distance. For a crack tip approaching a given weak interface pattern, a reverse R-curve type trend was observed, where fracture energy decreased with decrease in the distance between the crack tip and the pattern. Within the same DCB specimen, as the crack tip advanced beyond the same patterned region, a standard R-curve trend was observed, where fracture energy increased with increasing crack lengths. Furthermore, the mode I fracture energy corresponding to a pattern region, scaled with the area fraction of weak interfaces, according to the simple rule of mixtures. Interestingly, under mixed mode loading, such that crack tip is steered towards the patterned adherend surface, fracture energy does not show R-curve type trends around the patterned regions even though the crack tip detects most of the weak areas. In contrast, a crack could be made to avoid exceptionally weak interfaces, when loaded under mixed mode conditions such that crack tip is steered away from the adherend surface containing the patterned region. These are interesting outcomes when considered in terms of potential applications such as controlled disassembly of the adhesive joints. Although based on limited and preliminary results, absence of R-curves in mixed mode conditions, combined with an ability to tune fracture energies in mode I conditions, may potentially offer joint design options to allow a joint to either tolerate or be more susceptible to interfacial defects, offering the ability

to tailor joint performance for designed failure modes, or easier disassembly. Though it should be noted that under infield applications, factors such as environmental conditions or other loading conditions such as fatigue etc. that might exist simultaneously or independently might lead to changes in the trends that are observed in this study.

This study was performed using a commercial toughened structural epoxy adhesive. Though this technique led to interesting insights that were not accessible and had never been reported before, the complex stress state in the patterned regions containing discreet defects leads to difficulties in exploring the underlying failure mechanics when a crack tip approaches a weakened interface. On the future note, use of a brittle adhesive that exhibits limited plasticity, coupled with adherends containing simple continuous defects might provide valuable insights into underlying failure mechanics.

Chapter III: Developing Characterization Procedures to Assess Adhesion Fundamentals for Chewing Gum Cud

In this study a probe test based approach was developed to obtain insights into the effect of surface energy and surface roughness on the gum cud adhesion. This approach enabled the introduction of substrates having well defined surface energies and surface topologies to elucidate the effect of these parameters on gum cud adhesion. A gum cud processing technique was introduced to easily and reproducibly process gum cuds in a way that mimics a chewing process, which facilitated the preparation of gum cuds samples with consistent properties. Rheological properties of gum cuds, surface properties of gum cuds as well as test substrates were successfully quantified. Using probe test based approach adhesion performance of gum cuds on substrates having well-defined topology and surface chemistry was successfully quantified.

For conditioned gum cuds used in this study, it was observed that decreasing the thermodynamic work adhesion by coating substrates with Gum Stopper solution, led to a decrease in the debonding work or adhesion of the gum cuds. Surprisingly, for gum cuds and the substrates used in this study, increasing the roughness of the substrate led to a decrease in the gum cud adhesion in general. Based on insights obtained during this study, an approximate relationship was proposed that correlated the effects of surface

energies, substrate roughness and gum cud rheology with the gum cud adhesion performance observed in probe tests.

It is envisioned that this approach could be helpful towards quantifying gum cud adhesion, leading to chewing gum formulations, which when chewed and improperly discarded, facilitate easier removal from adhering surfaces during the cleanup process. Also, it would be interesting to study the gum cud penetration in well-defined surface asperities as a function time and applied pressure and how it relates with the constitutive and non-linear properties of the chewed gum cuds.

Chapter IV: Creep Rupture Performance of Silicone Sealants for Solar Panel Support Applications

In this chapter we aimed to highlight a procedure to obtain insights into and compare the long-term performance of three different silicone sealants designed for load-bearing applications such as solar panel support applications, though the techniques and materials may also be relevant in other engineering and building structures. Using a 72-station pneumatic creep frame, three different silicone sealants were tested at three temperature and humidity pairs. In addition to the creep rupture tests, ramp to fail tests were performed on specimens fabricated with one of the sealants at three rates of strain and at three temperatures. Using the time-temperature-superposition principle (TTSP), thermal shift factors were obtained from dynamic mechanical analysis. The thermal shift factors obtained from dynamic small strain constitutive tests were used to form reasonable master curves for the data from ramp to fail and creep rupture tests. Thermal shifting led to simulation of creep rupture failure times up to three years based on the tests performed in one month. Creep rupture and ramp to fail master curves, when plotted on log-log scales, resulted in linear relationships between time to fail or crosshead rate, respectively, and applied or breaking stress, respectively. Also, master curves from constitutive DMA, ramp to fail, and creep rupture tests showed similar slopes, thus suggesting a constant strain to failure criteria. Data obtained from creep rupture tests in particular showed significant scatter, though not unusual for creep rupture results on silicone sealants. In light of the scatter observed in the data, the creep rupture data from

three sealants appeared to be indistinguishable. Small slopes of the master curves for all the sealant indicated a very small time dependence of failure times for silicone sealants used in this study, which significantly contributes to the observed scatter in the creep rupture data. Due to the scatter observed in the creep rupture tests data, long-term verification testing are recommended for better insights into the accuracy of the predicted master curves.

Appendix A: Force vs. displacement curves for B type gum cuds

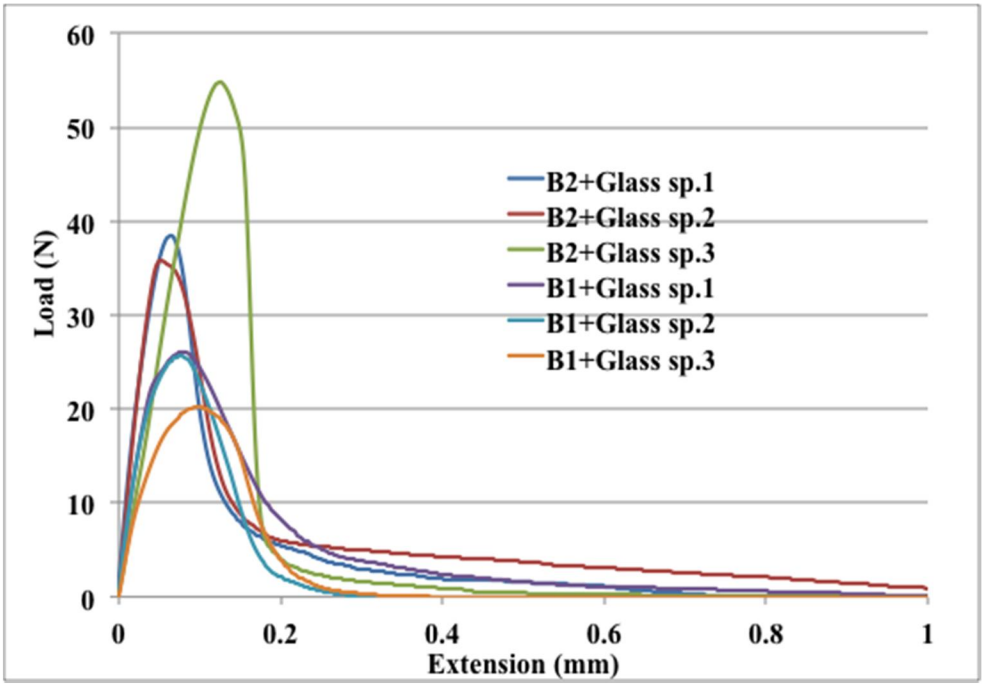

Figure A-1: Force vs. displacement curves for probe tests on B gum cuds on Glass substrates

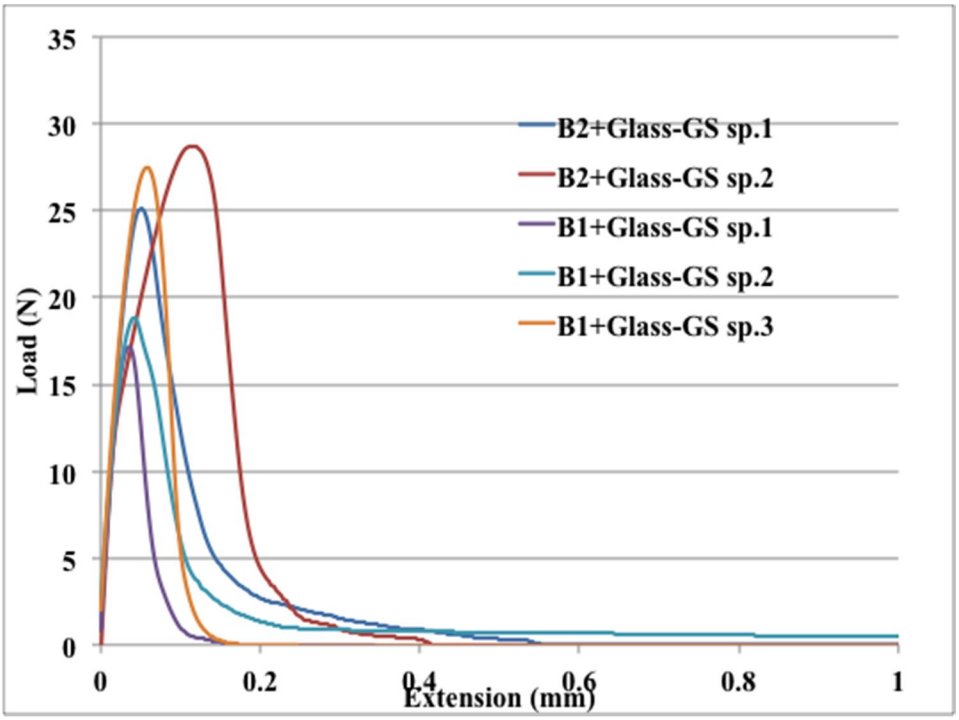

Figure A-2: Force vs. displacement curves for probe tests on B gum cuds on Glass-GS substrates

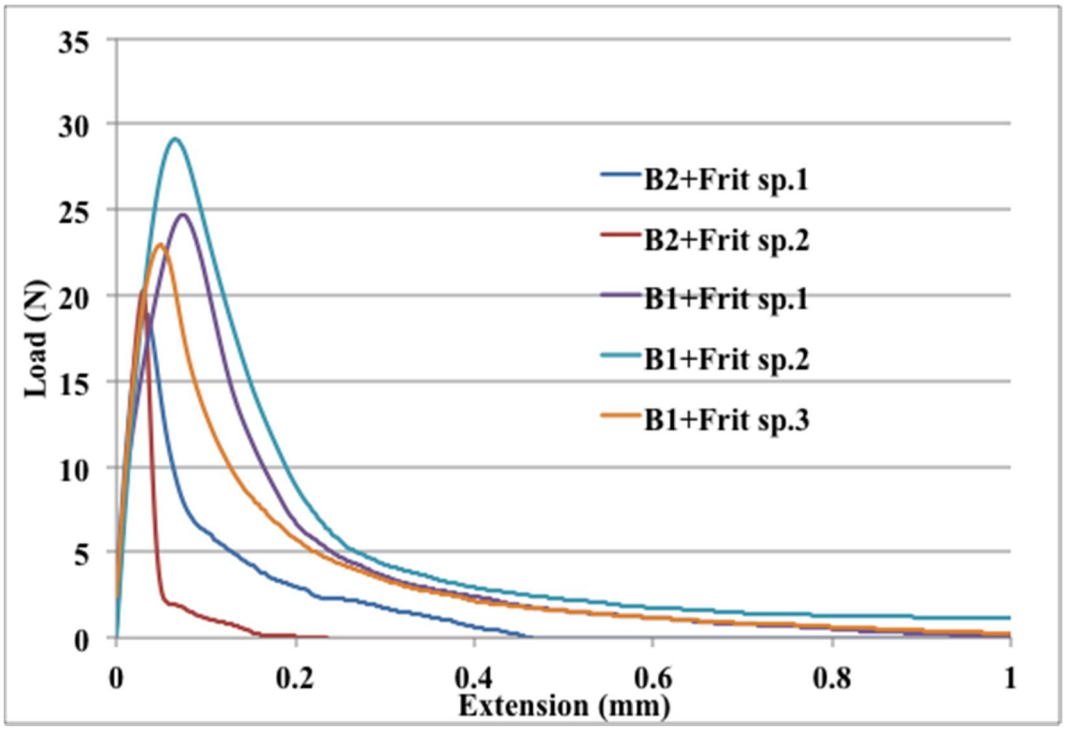

Figure A-3: Force vs. displacement curves for probe tests on B gum cuds on Frit substrates

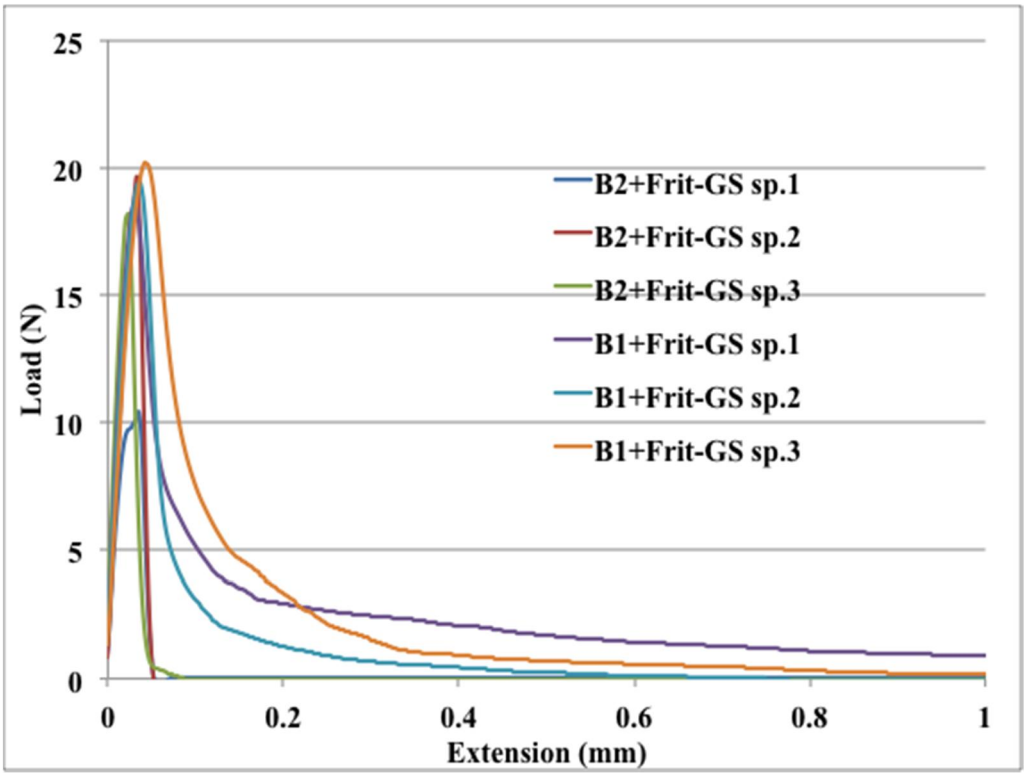

Figure A-4: Force vs. displacement curves for probe tests on B gum cuds on Frit-GS substrates

Appendix B: Statistical analysis of probe tests

Table B-1: Means and standard deviations of all combinations of substrates and gum

Level	Number	Mean	Std Dev	Std Err Mean	Lower 95%	Upper 95%
B1-Frit	3	4.1764	1.42511	0.8228	0.64	7.717
B1-Frit-GS	3	2.2915	1.27829	0.7380	-0.88	5.467
B1-Glass	3	3.4691	1.38686	0.8007	0.02395	6.914
B1-Glass-GS	3	1.3136	0.67050	0.3871	-0.35	2.979
B2-Frit	2	1.3376	0.87794	0.6208	-6.55	9.226
B2-Frit-GS	3	0.4446	0.12070	0.0697	0.14	0.744
B2-Glass	3	5.9179	1.05371	0.6084	3.30	8.535
B2-Glass-GS	2	3.5204	0.76971	0.5443	-3.40	10.436
A1-Frit	3	17.2590	3.67404	2.1212	8.13	26.386
A1-Frit-GS	3	7.8758	2.44680	1.4127	1.80	13.954
A1-Glass	3	38.8358	7.30629	4.2183	20.69	56.986
A1-Glass-GS	3	36.7020	9.41004	5.4329	13.33	60.078
A2-Frit	3	3.3656	0.67358	0.3889	1.69	5.039
A2-Frit-GS	3	0.8667	0.42836	0.2473	-0.20	1.931
A2-Glass	2	6.5412	0.01571	0.0111	6.40	6.682
A2-Glass-GS	3	2.3213	0.49608	0.2864	1.09	3.554

Appendix C: DOE inputs and interaction plots

Table C-1: DOE input parameters

Gum Type	Storage modulus (Pa)	Tan delta	Substrate roughness (microns)	Surface energy (J/m2)	Area (N.mm)	Peak force (N)
B1	234000	0.46	0	45	5.043962	26.14411
B1	234000	0.46	0	45	2.933126	25.64979
B1	234000	0.46	0	45	2.430207	20.1966
B1	234000	0.46	0	12	0.657757	17.14373
B1	234000	0.46	0	12	1.997857	18.85438
B1	234000	0.46	0	12	1.285047	27.47254
B1	234000	0.46	21.09	45	3.506962	24.6516
B1	234000	0.46	21.09	45	5.812977	29.12234
B1	234000	0.46	21.09	45	3.209266	22.94346
B1	234000	0.46	21.09	12	3.620451	18.6142
B1	234000	0.46	21.09	12	1.070752	19.40011
B1	234000	0.46	21.09	12	2.18322	20.21359
A2	522000	0.59	0	45		56.37134
A2	522000	0.59	0	45	6.55236	77.43789
A2	522000	0.59	0	45	6.530138	54.78064
A2	522000	0.59	0	12	2.480098	63.51321
A2	522000	0.59	0	12	1.765292	51.04095
A2	522000	0.59	0	12	2.718589	58.6515
A2	522000	0.59	21.09	45	3.83574	49.54282
A2	522000	0.59	21.09	45	3.667144	51.68846
A2	522000	0.59	21.09	45	2.593942	47.80723
A2	522000	0.59	21.09	12	0.372625	10.40019
A2	522000	0.59	21.09	12	1.134021	28.63079
A2	522000	0.59	21.09	12	1.093435	33.3643
B2	203000	0.58	0	45	4.702391	38.49666
B2	203000	0.58	0	45	6.479365	35.74582
B2	203000	0.58	0	45	6.572041	45.09608
B2	203000	0.58	0	12	2.976089	25.16724
B2	203000	0.58	0	12	4.064625	28.71193
B2	203000	0.58	0	12		
B2	203000	0.58	21.09	45	1.958379	18.82719
B2	203000	0.58	21.09	45	0.716788	20.23014
B2	203000	0.58	21.09	45		
B2	203000	0.58	21.09	12	0.312128	11.47398
B2	203000	0.58	21.09	12	0.548314	19.59138
B2	203000	0.58	21.09	12	0.47347	18.15046

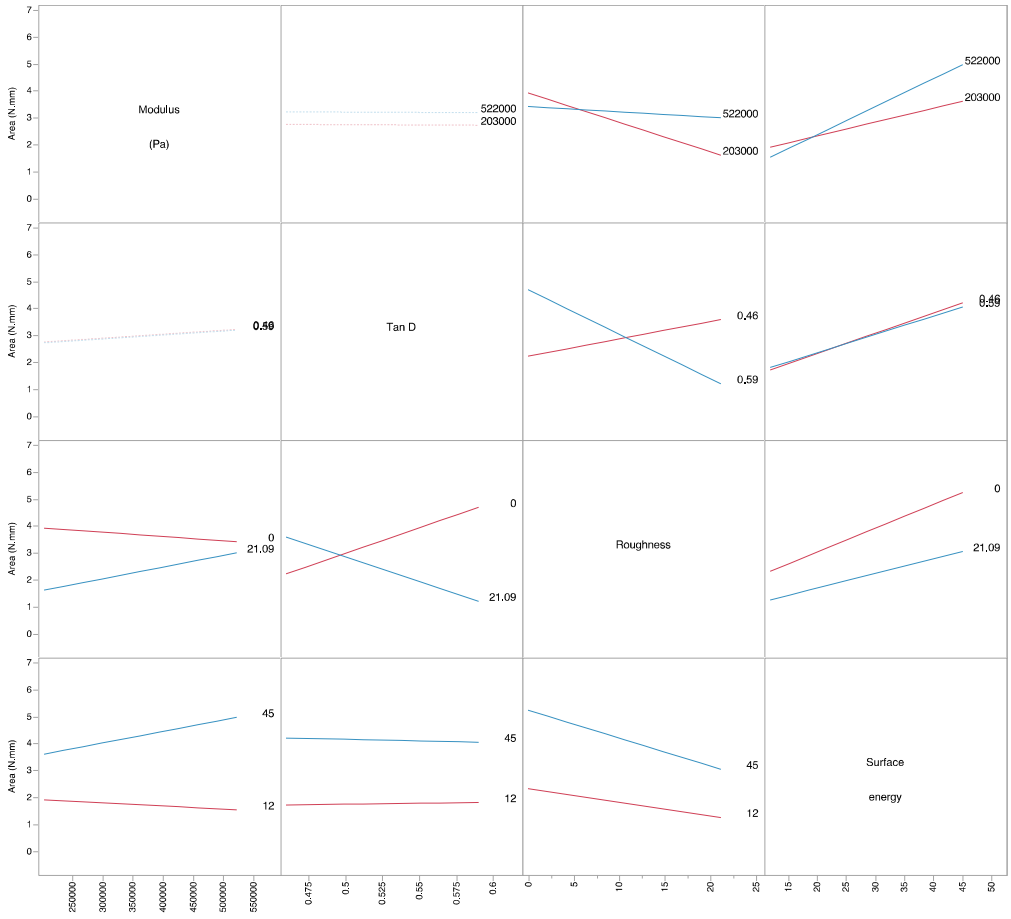

Figure C-1: Interaction plots from DOE analysis

Appendix D: Gum penetration study using EDX and SEM analysis

Test Approach

In this approach a SEM image of the gum cud/fine frit interface region was overlaid with element contour map of the same region obtained using EDX analysis. Since gum cud has relatively large carbon content, compared to the Pyrex glass frit, which contains relatively larger content of silicon atoms. Thus, it is expected that carbon atom signal from the gum cud would be stronger while it would be very weak in the region of glass frit. Similarly the silicon atom signal for gum cud would be very weak while that from the Pyrex glass would be strong. Thus if the element contour map images for these signals are overlaid with an SEM image it was expected that insights into gum penetration could be obtained on a micron scale.

Specimen Preparation

A1 gum cud specimens and a fine Pyrex glass frit was used during this study. Utilizing frit test setup A1 gum cud specimen was bonded to the fine glass frit at 300 kPa pressure for five minutes. After the application of pressure the frit was fractured at room temperature to expose the gum cud/Pyrex glass interface. The specimen was then sputtered with carbon and analyzed using a FEI Quanta 600 FEG scanning electron microscope outfitted with a Fisons-Kevex 771 energy dispersive X-ray spectroscopy (EDX) analyzer (Quantax System; Bruker AXS, Ewing, NJ).

Preliminary results

Figure D-1 shows a SEM image of a cross-section of gum cud bonded to a fine frit. The image also shows a region where SEM and EDX analysis was performed.

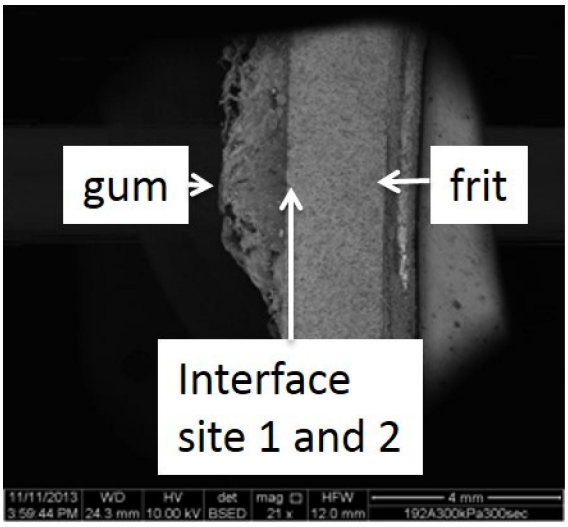

Figure D-1: Cross-section of gum cud bonded to a fine frit

Figure D-2 shows higher magnification SEM images of interface regions highlighted in Figure D-1.In each of the images the glass frit is present on the right side while the gum cud is present on the left side. Though a clear distinction between gum cud and glass frit was observed, it was difficult to quantitatively establish the gum penetration depth. Based on contrast differences, it was estimated that the gum cud penetrated about 100 microns within the glass frit.

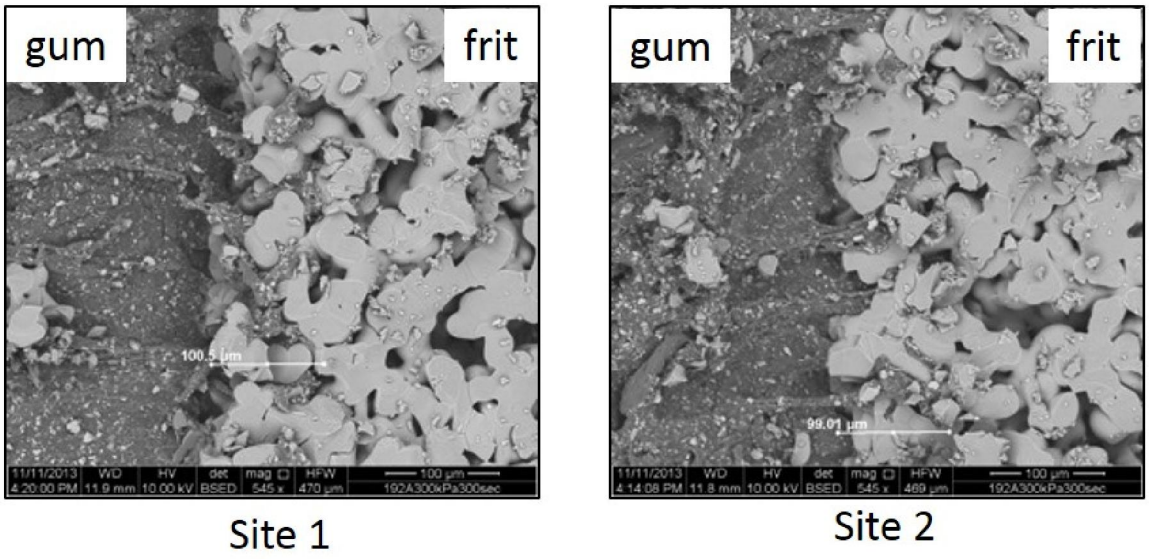

Figure D-2: SEM images showing gum cud penetration in smooth glass frit.

Figure D-3 shows the same SEM images overlaid with EDX analysis. Green represents the silicon signal while red represent the carbon signal. The regions that do not show any color are regions where no signal could be gathered, as signals from these regions did not reach the detector. Due to relative difference in carbon and silicon content in gums and frits respectively, a clear distinction was observed between the bulk of gum cud, glass frit signal leading to insights into gum cud penetration within the glass frit. Based on EDX images overlaid with SEM images it was possible to measure gum cud penetration in glass frit pores, which was about 100 microns.

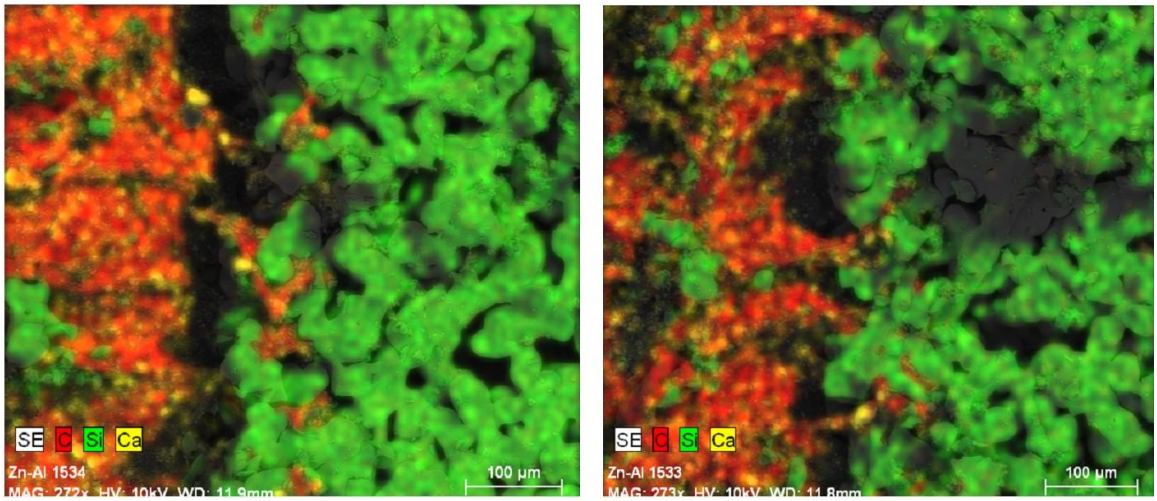

Figure D-3: EDX results overlaid on SEM images shown in Figure D-2

Appendix E: Determination of thermodynamic work of adhesion using Fowkes's approximation, Young's equation and contact angle experiments

Candace Wall, Alan Esker

Department of Chemistry

Virginia Tech
Blacksburg, VA 24061

The practical work of adhesion for a two-layer system as depicted in Figure 1, can be written as:

$$W_{AD} = W_{th} + f(W_{th})\varsigma(Rate, Temperature, ..) \quad \textbf{(E1)}$$

according to Pocius [1], where W_{th} is the thermodynamic work of adhesion and ς is a function of temperature and rate that reflects the mechanical contribution to the overall work of adhesion. Equation E1 shows that the thermodynamic work of adhesion is only part of the total and also modifies the viscoelastic contributions to the work of adhesion. In typical adhesive systems, the practical work of adhesion normally dominates the thermodynamic work of adhesion, nonetheless, the thermodynamic work of adhesion must be favorable to tap into the viscoelastic properties of the adhesives. As the adhesion of gum to concrete is expected to behave like a polymeric adhesive system governed by Equation 1, a deeper look into the thermodynamic work of adhesion is warranted.

Figure E-1: Schematic depiction of a two-layer system and the breakdown of the surface energies into polar and dispersive components.

Application of the Dupre' equation [2] for the thermodynamic work of adhesion to the material system in Figure E1 yields:

$$W_{th} = \gamma_1 + \gamma_2 + \gamma_{12} \qquad \textbf{(E2)}$$

where γ_1 and γ_2 are the surface energies of materials 1 and 2 against air, respectively, and γ_{12} is the interfacial energy between materials 1 and 2. Application of Equation E2 to Figure E1 is usually not trivial. Surface energies of solids are not as well-known as surface energies of liquids, and interfacial energies between solids are generally not experimentally accessible quantities, an approximate form of the interaction energy for non-polar materials (those containing only dispersive forces) was derived from treatments of interfacial forces in terms of Hamaker constants. The approximate form for non-polar systems is given as [3, 4]:

$$\gamma_{12} = \gamma_1 + \gamma_2 - 2\sqrt{\gamma_1 \gamma_2} \qquad \textbf{(E3)}$$

This approach was extended [5] to treat substances with both polar and dispersive interactions:

$$\gamma_{12} = \gamma_1 + \gamma_2 - 2\sqrt{\gamma_1^d \gamma_2^d} - 2\sqrt{\gamma_1^p \gamma_2^p} \qquad \textbf{(E4)}$$

where it was assumed that the interfacial energies could be broken into additive polar (superscript *p*) and dispersive (superscript *d*) components, $\gamma_1 = \gamma_1^d + \gamma_1^p$ and $\gamma_2 = \gamma_2^d + \gamma_2^p$, and the dispersive and polar interaction energies could be treated as geometric means. The combination of Equation E4 and E3 provides an estimate of

the thermodynamic work of adhesion in terms of the polar and dispersive components of materials 1 and 2:

$$W_{th} = 2\sqrt{\gamma_1^d \gamma_2^d} + 2\sqrt{\gamma_1^p \gamma_2^p} \qquad \textbf{(E5)}$$

While other treatments exist, such as the breakdown of surface energies into dispersive, acid and base contributions, along with other methods for treating the interaction energies such as arithmetic means, Equation E4 was assumed as a starting point for addressing the problem of gum adhesion to concrete. Two reasons for this are the ability to estimate solid surface energies from contact angle measurements and the ability to examine how a third layer (such as the weak boundary layer proposed as one mechanism for overcoming strong gum concrete adhesion) influences the work of adhesion. Figure 2 provides a depiction of a trilayer model where layer 3 would be the weak boundary layer with a surface energy against air of $\gamma_3 = \gamma_3^d + \gamma_3^p$. The resulting expression for the thermodynamic work of adhesion [6] is given as:

$$W_{th} = 2\left(\gamma_3 - \sqrt{\gamma_1^d \gamma_3^d} - \sqrt{\gamma_1^p \gamma_3^p} - \sqrt{\gamma_2^d \gamma_3^d} - \sqrt{\gamma_2^p \gamma_3^p} + \sqrt{\gamma_1^d \gamma_2^d} + \sqrt{\gamma_1^p \gamma_2^p}\right) \qquad \textbf{(E6)}$$

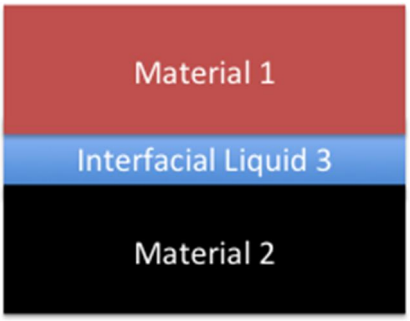

Figure E-2: Schematic depiction of a two-layer system with a weak boundary layer. The boundary layer is assumed to be "bulk" in dimension

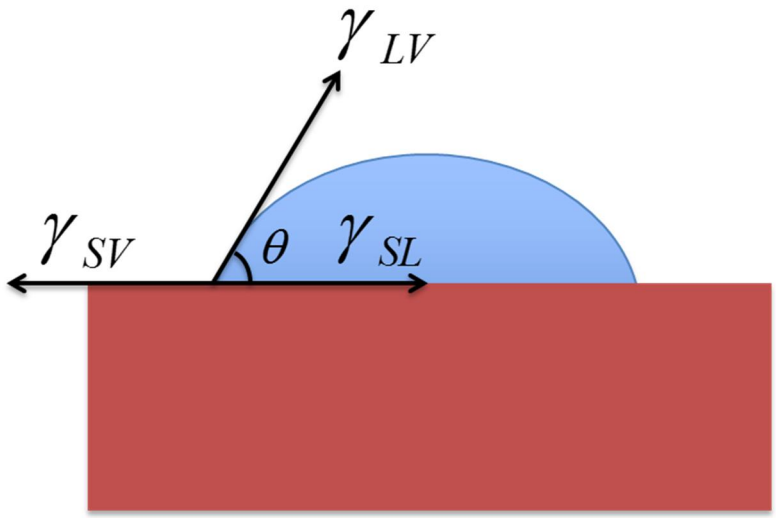

Figure E-3: Schematic depiction of the contact angle and relevant forces acting on the three phase contact line through the different interfacial energies.

The connection between liquid contact angles, solid surfaces, and Equations E1 and E9 begins with the balance of forces associated with the three phase contact line depicted in Figure D3. Balancing the forces at the three phase contact line gives rise to Young's equation [7]:

$$\gamma_{SV} = \gamma_{SL} + \gamma_{LV}\cos\theta \qquad \textbf{(E7)}$$

where γ_{SV}, γ_{SL} and γ_{LV} are the interfacial energies of the solid-vapor, solid-liquid and liquid-vapor interfaces, respectively, and θ is the contact angle. If one assumes these interfacial energies can be broken into the additive sum of polar and dispersive contributions, $\gamma_{SV} = \gamma_S^d + \gamma_S^p$, $\gamma_{SL} = \gamma_{SL}^d + \gamma_{SL}^p$, and $\gamma_{LV} = \gamma_L^d + \gamma_L^p$ (note that V was dropped from the subscripts of the solid-vapor and liquid-vapor interfaces tems to simplify later expressions), Equation E9 can be used to define the interfacial energy between the droplet and the solid surface:

$$\gamma_{SL} = \gamma_{SV} + \gamma_{LV} - 2\sqrt{\gamma_S^d \gamma_L^d} - 2\sqrt{\gamma_S^p \gamma_L^p} \qquad \textbf{(E8)}$$

The combination of Equations E7 and E8 yields [8]:

$$\frac{\gamma_{LV}(1+\cos\theta)}{2\left(\gamma_L^d\right)^{1/2}} = \left(\gamma_S^d\right)^{1/2} + \left(\gamma_S^p\right)^{1/2}\left(\frac{\gamma_L^p}{\gamma_L^d}\right)^{1/2} \qquad \textbf{(E9)}$$

Hence a graph of the left hand side of Equation E9 versus the square root of the ratio, γ_L^P / γ_L^d, is a straight line with an intercept equal to the square root of γ_s^d and a slope equal to the square root of γ_s^p Equation E9 is used in this study to evaluate the surface energies of various gums, surfaces and weak boundary layer materials. Thermodynamic work of adhesion can then be estimated using Equation E5.

Appendix F: Studying the interaction of a propagating crack with the locally weakened interface using finite element methods

Background

Numerical simulations were carried out using a commercial finite element analysis software ABAQUS® to obtain insights into the crack path selection in bonded joints containing weakened interfaces. The objective of this preliminary analysis was to study the effect of adhesive plasticity on the crack path selection in an adhesive joint containing a localized weakened interface. A previously developed finite element model was used for this preliminary analysis [1]. This model consisted of a cohesive zone based approach for the simulation of interfacial fracture, while the (extended finite element method) XFEM was used for the simulation of the crack propagation within the bulk adhesive layer. Details about this approach have been discussed in detail in a previously reported study [1].

Model parameters

The geometry and boundary conditions used for the finite element model are shown in Figure F-1. The model geometry was based on a double cantilever beam (DCB) specimen with adherends dimensions of 150×25.4×12.7 mm (length x with x thickness). The adhesive layer dimensions were 150×25.4×0.25 mm (length x width x thickness). The model contained a pre-crack (crack length from loading points to the crack tip equal to 58 mm) located at the middle of the adhesive layer. The distance between the pre-crack tip and the start of the weakened interface was two mm (eight bondline thicknesses). These distances were chosen so that the initial crack growth would be independent of the presence of weak interface and entire history of crack path selection can be studied as the crack propagates. Indeed, the following simulations show that this two mm gap (8 times the adhesive layer thickness) is sufficiently large to avoid effects of the weakened zone on the crack path during the initial stages of crack propagation

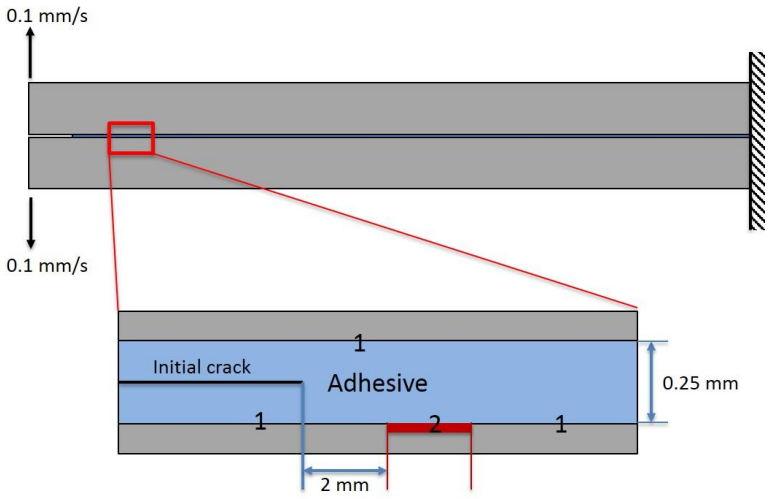

Figure F-1: Location of the weak interface in the DCB specimen model with initial crack.

The adherends were modeled using as an elastic material with Young's modulus $E = 70GPa$ and Poisson's ratio $\upsilon = 0.33$. These properties are of aluminum 6061-T6 alloy that was used as adherend material during the DCB tests reported in Chapter 3. The adhesive material was modeled as an elastic-plastic (strain-hardening) material. The Young's modulus and Poisson's ratio of the adhesive material was 3 GPa and 0.33 respectively. These properties are typical for an Epoxy material in the glassy state. The plasticity in the adhesive layer was modeled using stress vs. strain data shown in Figure F-2.

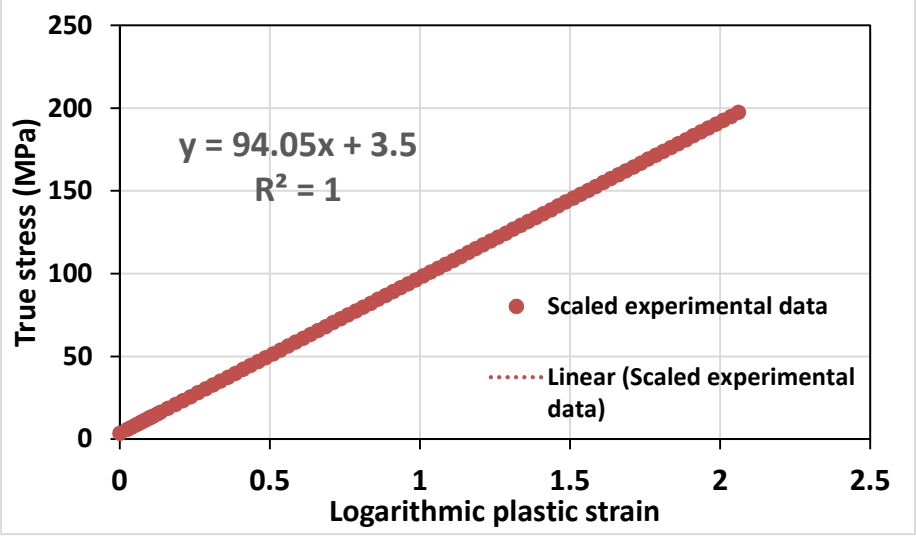

Figure F-2: Data used to model the plasticity of an adhesive layer

The data used to model the plasticity was based on compression tests data for the adhesives used during the DCB tests reported in Chaper 3 (Figure 3.4). This adhesive is a commercially available toughened structural adhesive. During finite element analysis, the experimental compressive stress vs. strain data was scaled down such that true yield stress of the adhesive material was 3.5 MPa while the slope of the trues stress vs. logarithmic plastic strain in Figure F-2 was similar to the experimental data shown in Figure 3.4. Residual stresses were assumed to be zero throughout this analysis.

As mentioned earlier, the cohesive elements were used for interfacial fracture, while the XFEM approach was used to simulate crack propagation within the bulk adhesive. Both the cohesive zone element method and XFEM are based on the CZM framework. Within a CZM framework, failure and crack propagation is simulated using a user-defined traction-separation law. The traction-separation law parameters used to simulate weak interface separation and for crack propagation within bulk adhesive are shown in Figure F-3. The parameters were chosen such that effect of plasticity on the crack path selection could be studied. The fracture energy of the strong interface is assumed to be similar to that of the adhesive 500 J/m^2, while the fracture energy of the weakened interfaces is assumed to be lower than that of the adhesive. The maximum tractions for the strong interface was 20 MPa. All materials in this study were simulated using 2D plane strain elements. Full integration analysis was used for adhesive layer while adherend materials were modeled using reduced integration analysis.

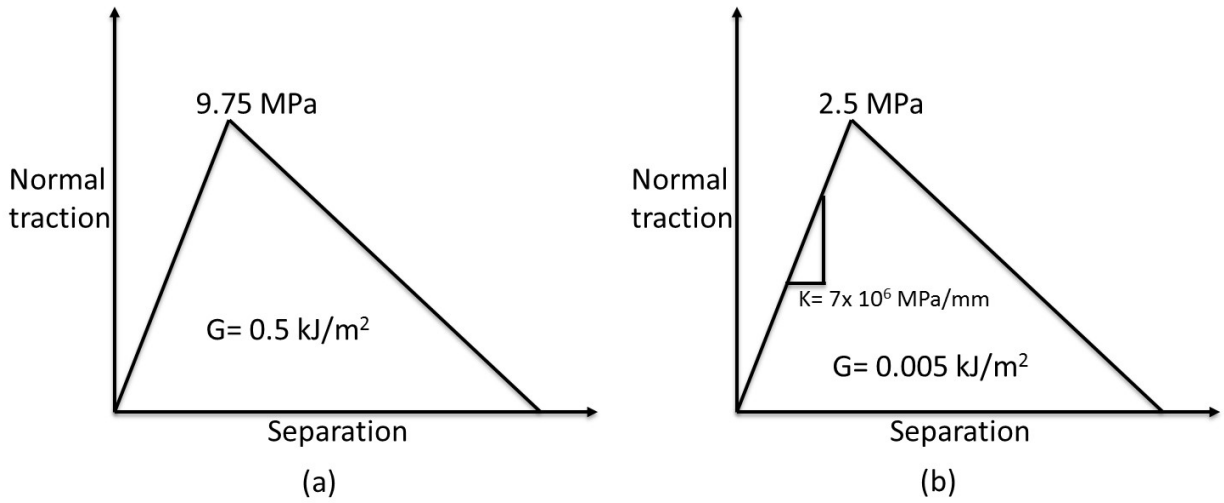

Figure F-3: (a) Traction-separation law parameters for crack propagation in bulk adhesive layer (XFEM based approach), (b) Traction-separation law parameters for weak interface separation (CZM based approach)

As mentioned earlier the aim of this preliminary analysis was to study the effect of plasticity on the crack path selection. Using material properties mentioned above the crack path selection can be studied for adhesive material which is elastic-plastic (strain hardening). In order to study the crack path selection in the absence of plasticity, same material parameters, boundary conditions and geometry as mentioned earlier were used except that the adhesive material was modeled as a purely elastic material with the Young's modulus and Poisson's ratio similar to the plastic case.

Preliminary results

For cohesive zone elements in weak interface regions, the damage variable is zero when the tractions have not reached the maximum traction value specified in the traction separation law, while damage variable becomes one when the materials separate. The Figure F-4 shows damage variable in the weak interface region for elastic-plastic and elastic model. For both the models, it can be observed that even if the crack tip is several bondline thicknesses away from the weak interface and has not deviated from the path, the weak interface has already started to separate (damage >0.99 for many elements).

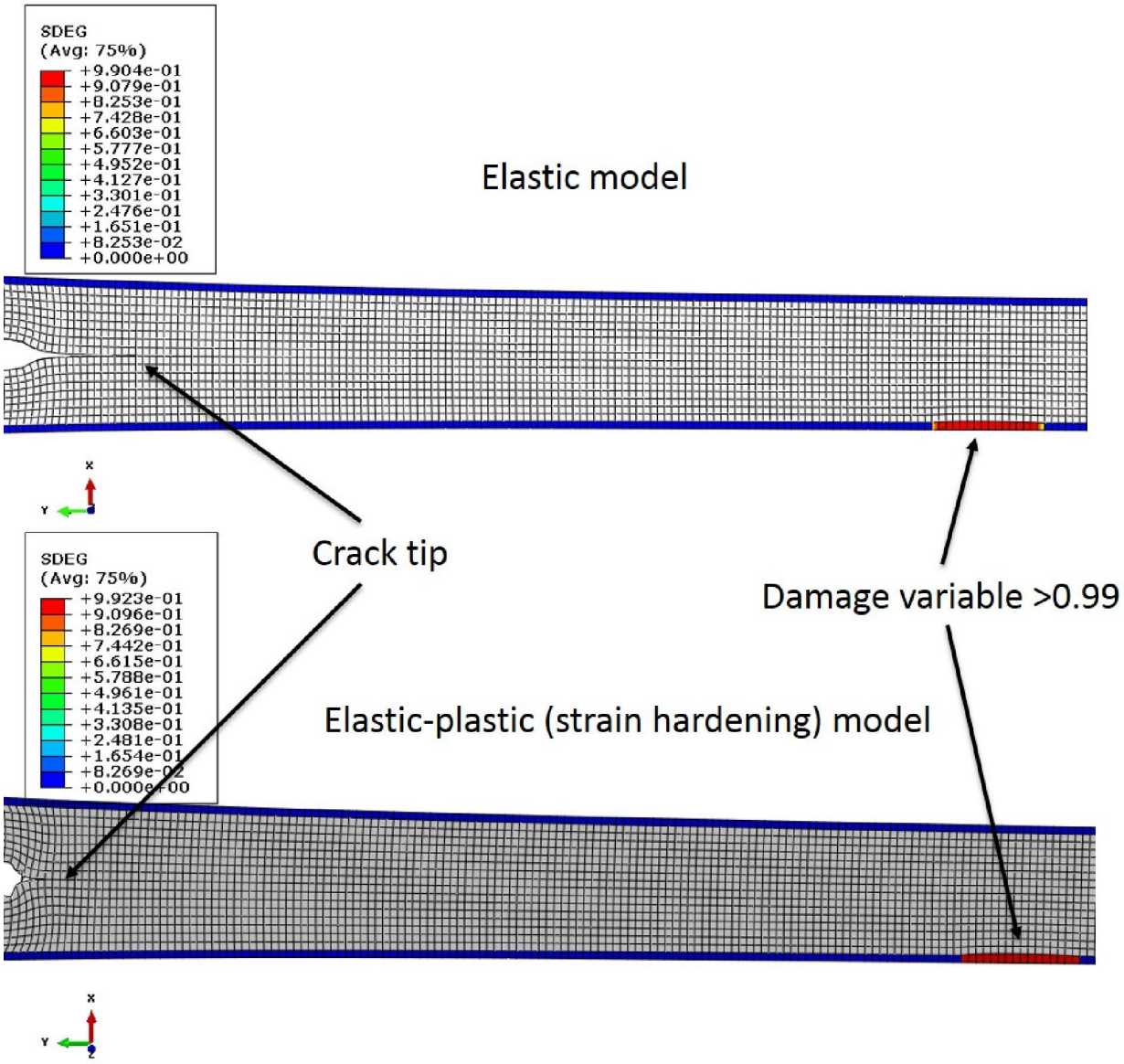

Figure F-4: Damage variable indicating onset of separation for elastic and elastic-plastic model

Figure F-5 shows peel stresses along the middle of the adhesive layer and ahead of the crack tip that is approaching a weakened interface for an adhesive layer that is elastic and for an elastic-plastic (strain hardening) adhesive layer. When the crack tip is sufficiently away from the weakened interface, the weak interface does not cause any changes in the stress distribution in the adhesive layer. In both of these cases, when the crack tip is sufficiently close to the localized weak interface the presence of weak interface causes changes in the stress distribution in and around the weak interface region. Upon observing damage variable (for weak interface) as the crack tip approached

the weak interface, the changes in stress distribution in and around the weak interface region were result of beginning of separation process at the weak interfaces (based on damage variable reaching 0.99 for several elements). Interestingly, in the case of the plastic model the changes in stress distribution occur when the crack tip is relatively farther to the weak interface region than that for an elastic model. This suggests that the weak interfaces affect the stress distributions over larger distances for an adhesive layer containing the plasticity than compared to a purely elastic or for a brittle adhesive layer. It must be noted however that the distances showed in Figure F-5 might change for finer mesh size as mesh independence was not confirmed for the model that contains the plasticity. The results from elastic model are mesh independent. In light of possible mesh dependence for the plastic model the results reported here are qualitative in nature.

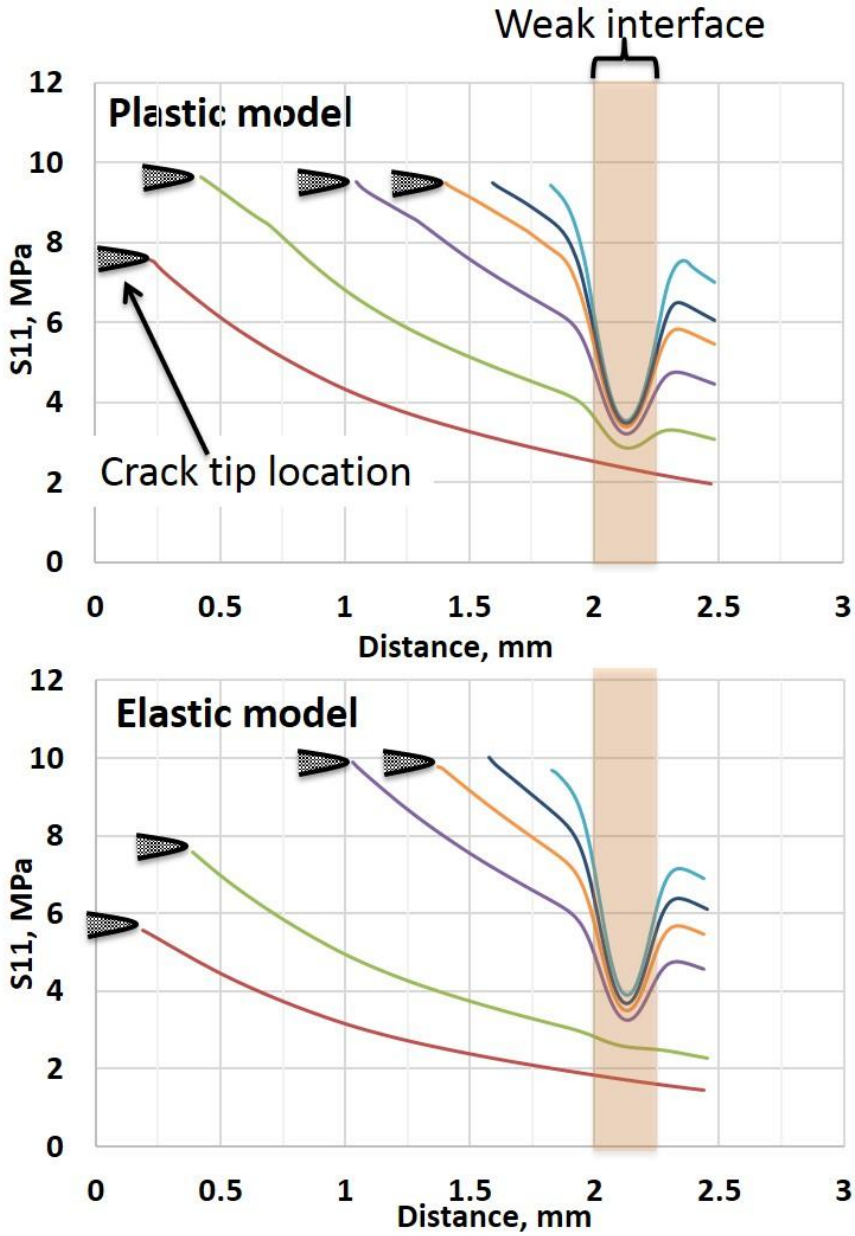

Figure F-5: Peel stresses ahead of the crack tip (along the middle of the adhesive layer) for elastic and elastic-plastic model

Future directions

As mentioned earlier, the results reported in this appendix are preliminary and qualitative. Mesh independent results would lead to quantitative insights into the effect of plasticity on the crack path selection. Similar study can be carried out for several values of peak traction and/or fracture energy in the weak interface cohesive zone elements.

References:

[1] Y. Guan, "Crack Path Selection and Shear Toughening Effects due to Mixed Mode Loading and Varied Surface Properties in Beam-Like Adhesively Bonded Joints," Doctor of Philosophy Dissertation, Virginia Polytechnic and State University, 2014.